Photonic Crystal Millimetre Wave and Terahertz Waveguides and Functional Components

Binbin Hong

Submitted in accordance with the requirements for the degree of
Doctor of Philosophy

The University of Leeds
School of Electronic and Electrical Engineering
Pollard Institute

June 2018

The candidate confirms that the work submitted is his/her own, except where work which has formed part of jointly authored publications has been included. The contribution of the candidate and the other authors to this work has been explicitly indicated below. The candidate confirms that appropriate credit has been given within the thesis where reference has been made to the work of others.

The work in Chapter 2 of the thesis has appeared in publication as follows:

Hong, B., Swithenbank, M., Somjit, N., Cunningham, J. and Robertson, I., 2016, Asymptotically single-mode small-core terahertz Bragg fibre with low loss and low dispersion. *Journal of Physics D: Applied Physics*, 50(4), p.045104.

I was responsible for literature review, preparation of results, and write up. The contribution of the other authors was advice of research methods and proof-reading.

The work in Chapter 3 of the thesis has appeared in publication as follows:

Hong, B., Swithenbank, M., Greenall, N., Clarke, R., Chudpooti, N., Akkaraekthalin, P., Somjit, N., Cunningham, J. and Robertson, I., 2017, Low-Loss Asymptotically Single-Mode Terahertz Bragg Fiber Fabricated by Digital Light Processing Rapid Prototyping. *IEEE Transactions on Terahertz Science and Technology*, 8(1), p.90-99.

I was responsible for literature review, design and fabrication of Bragg fibres, preparation of theoretical and measurement results, and write up. The contribution of the other authors was material characterization, measurement setup and calibration, advice on simulation, and proof-reading.

Partial works in Chapter 1 and Chapter 8 has also appeared in the above two publications, of which the author owns the first authorship.

Acknowledgements

I would like to express my sincere gratitude to those who have contributed to this thesis and helped me in one way or another during this unforgettable journey.

Firstly, I would like to thank my supervisors Dr. Nutapong Somjit, Prof. John Cunningham and Prof. Ian Robertson. It is your patience, encouragements and continuous support that helped me out of my hesitations and anxieties. It is you who allow me to think freely in the kingdom of knowledge, and also remind me to do right thing at the right time. Your wisdom always inspire me and will also continue to benefit my future life.

Acknowledgement should also go to the China Scholarship Council and University of Leeds for sponsoring my research.

In the process of my research, I have received enormous supports. I would like to thank Prof. Yunhua Zhang and Dr. Lukui Jin for their helpful discussions in our related research topics. I wish to thank Dr. Dragan Indjin and Dr. Paul Steenson who gave me constructive suggestions on my transfer report and annual progress reviews. Thanks to Mr. Roland Clarke and Dr. Viktor Doychinov for helping me in the measurement methodology of the vector network analyzer. Thanks also to Dr. Nicholas Hunter, Dr. Matthew Swithenbank, Dr. Nicholas Greenall, and Dr. Joshua Freeman for introducing the terahertz measurement facilities to me. I also wish to thank Dr. Yingjun Han and Dr. Lianhe Li for sharing your knowledge on the theory and fabrication of the quantum cascade laser with me. I wish also to thank Mr. Graham Brown and Mr. Andrew Pickering for their timely help on the fabrication of the THz waveguides. I also want to thank Isibor Obuh, Evans Silavwe, Dominic Platt, Nonchanutt Chadpooti, and Nattapong Duangrit for helpful discussions during the group meetings.

I would like to thank my colleagues at Pollad Institute and IRASS. It is the free coffee and relax conversation in the kitchen and foyer that makes my everyday work life joyful and colorful. I would also like to thank Mrs Susan Hobson, Mrs Clair Atkinson and Mrs Louise Coffey at Pollard Institute and IRASS for providing clerical help.

Acknowledgement should also go to Jiacheng Zhang, Rui Dong, Kun Meng, Lei Shi, Jingbo Wu, Jingxuan Zhu, Zhiqiang Zhang, Jing Tang, Nan Jian,

Xinliang Xu, Meng Xu, Xujun Luo, Ying Wang, and all friends from Leeds HiTECH Innovation Society, who make my life in the UK so unforgettable.

I want to express my gratitude to my parents and sister. Your selfless love and unconditional support all through my life make me who I am now.

My greatest thanks go to my dearest wife, Yanhong Huang, who shares happiness and sorrows with me. You are my sunshine, my only sunshine. You make me happy when skies are gray. I love you more than I can say.

List of Publications

Journal articles and conference papers based on the research for, and written within the duration of, this thesis:

Journal articles

- **Hong, B.**, Swithenbank, M., Somjit, N., Cunningham, J. and Robertson, I., 2016, Asymptotically single-mode small-core terahertz Bragg fibre with low loss and low dispersion. *Journal of Physics D: Applied Physics*, 50(4), p.045104.

- **Hong, B.**, Swithenbank, M., Greenall, N., Clarke, R., Chudpooti, N., Akkaraekthalin, P., Somjit, N., Cunningham, J. and Robertson, I., 2017, Low-Loss Asymptotically Single-Mode Terahertz Bragg Fiber Fabricated by Digital Light Processing Rapid Prototyping. *IEEE Transactions on Terahertz Science and Technology*, 8(1), p.90-99.

Conference papers

- **Hong, B.**, Somjit, N., Cunningham, J. and Robertson, I., 2015, August. Design study of low loss single-mode hollow core photonic crystal terahertz waveguide with support bridges. In *Infrared, Millimeter, and Terahertz waves (IRMMW-THz), 2015 40th International Conference on* (pp. 1-2). IEEE.

- **Hong, B.**, Somjit, N., Cunningham, J. and Robertson, I., 2017, June. High-Order Operating Mode Selection Using Second-Order Bandgap in THz Bragg Fiber. In *Millimetre Waves and Terahertz Technologies (UCMMT), 2017 IEEE 10th UK-Europe-China Workshop on*. IEEE.

Journal articles (in progress)

- **Hong, B.** , Chudpooti, N., Akkaraekthalin, P., Somjit, N., Cunningham, J., and Robertson, I., 2018. Investigation of Electromagnetic Mode Transition and Filtering of Asymptotically Single-mode Hollow THz Bragg Fibre. *Journal of Physics D: Applied Physic*. (Accepted)

- Chudpooti, N., Doychinov, V., **Hong, B.** , Akkaraekthalin, P., Robertson, I., and Somjit, N., 2018. Multi-Modal Millimeter-Wave Sensors for 3D Printing Polymer Characterization. *Journal of Physics D: Applied Physics*. (Accepted)

- **Hong, B.**, Doychinov, V., Platt, D., Clarke, R., Akkaraekthalin, P., Somjit, N., Cunningham, J., and Robertson, I., 2018. Design and Measurement of a Single-Mode Hollow Photonic Crystal Integrated Waveguide. (In preparation)

- **Hong, B.**, Somjit, N., Cunningham, J., and Robertson, I., 2018. Octave Bandwidth Single-mode Hollow Bragg Reflector Integrated Waveguide. (In preparation)

Conference Paper (in progress)

- **Hong, B.**, Somjit, N., Cunningham, J. and Robertson, I., 2018, September. Modelling and Design of a THz Hollow Photonic Crystal Integrated Waveguide. In Infrared, Millimeter, and Terahertz waves (IRMMW-THz), 2018 43th International *Conference on* (pp. 1-2). IEEE. (Accepted)

Abstract

This work discusses both the theoretical and experimental guidance of low-loss single-mode millimetre-wave (mmW) and terahertz (THz) waves within microstructured photonic crystal fibre or waveguides, as well as functional components which can be built upon them. The aim of this work is to provide good interconnects for mmW and THz system. The interconnects are desired to be low loss, single mode, low dispersion, as well as easy to fabricate and integrate. In this work, photonic crystal structures, which can easily manipulate the wave-behaving photons by artificially changing its geometrical and material properties, are used in the proposed mmW and THz waveguides. The proposed photonic crystal waveguides includes cylindrical Bragg fibres and flat hollow photonic crystal integrated waveguides. The geometrical differences between Bragg fibres and photonic crystal integrated waveguides make them work better for different challenges. The former are promising for long distance guidance of signals due to its ultra-low loss, while the latter are strong candidates for compact and multilayer packaging applications since its flatness and other exceptional properties.

The thesis has three primary themes. The first them is about the design principles, analysis, and fabrication and measurement of low-loss asymptotically single-mode THz Bragg fibres. A design principle for manipulating the photonic bandgap of Bragg fibres, which is called as the generalized half-wavelength condition, is proposed. Based on the design principle, an ultra-low loss THz Bragg fibre with single mode and low dispersion is proposed, verified by the simulation. Considering practical fabrication challenges, a sub-THz Bragg fibre is fabricated using 3D printing technology and characterized to be one of the lowest loss waveguide at around 300 GHz. The mode transition and filtering in the fabricated sub-THz Bragg fibre is investigated, disclosing the mechanisms of asymptotically single-mode operation pattern of Bragg fibres.

The second theme is about the design, fabrication and measurement of single-mode mmW flat and hollow photonic crystal integrated waveguides with low loss and zero group velocity dispersion. The hollow photonic crystal integrated waveguides comprise of air-core line-defect photonic crystal structures sandwiched by a pair of metallic parallel plates. Two different types of photonic crystals are used in the designs, namely hexagonal lattice

array of air holes in dielectric slab and Bragg reflectors that consist of periodic arrangement of dielectric layers and air layers. Therefore, two types of hollow photonic crystal integrated waveguides are designed. The designs are fabricated and verified at Ka-band by measurements. The hollow photonic crystal integrated waveguides possess the merits of both substrate integrated waveguide and photonic crystal waveguide, but eliminates their drawbacks, making them strong candidates for compact and multilayer mmW and THz system-in-package applications.

The third theme is about the design and simulation of mmW and THz functional components built upon the previously designed microstructured photonic crystal fibres and flat waveguides. The functional components that have been designed include waveguide bends, power splitters or combiners, cavity, h-plane horn antenna, and circular Bragg fibre horn antenna. This theme aims to demonstrate the expansibility and flexibility of the proposed microstructured photonic crystal fibres and flat waveguides as promising platforms for designing mmW and THz functional components.

Though each theme discusses the theoretical analysis and/or experimental measurements of distinct phenomena, they are deeply related within the overall theme of engineering low-loss single-mode fibres or waveguides and their integration into mmW or THz systems.

Table of Contents

List of Tables

List of Figures

Dedicated to my beloved family for their constant support and unconditional love…

Chapter 1
An Introduction to Terahertz Waveguides and Materials

The THz wavelength (0.1 mm ~ 1 mm), or frequency range (0.3 THz ~ 3 THz), is of great interest to the scientific community owing to its associated characteristic scales in time, length and energy level, and has recently attracted significant attention for public safety [1], submillimetre astronomy [2], plasma fusion diagnostics [3], medial and agriculture imaging [4, 5], communication [6], as well as identification of chemical or biological species [7]. Historically, this region of the spectrum was known as the “THz gap”, which refers to the fact that it is particularly difficult to generate THz waves with artificial sources because of its location in the spectrum within the interval between optical and electronic technologies [8]. The development of compact and robust THz systems has proved to be challenging due to the lack of high-power sources and high-sensitivity detectors, along with the high loss of typical transmission mediums [9]. Low-loss single-mode THz waveguides, which are fundamental and key components needed to interconnect the functional components in a THz system, are of significant interest, and especially when the power of sources and sensitivity of detectors are relatively weak.

Material properties and geometrical structures are the two main factors that affect the propagation loss of a waveguide. Metals introduce more ohmic loss as the wavelength of the guided wave becomes shorter. Most dielectric materials attenuate THz waves significantly [10]. Air, among those dielectric materials, is a very low loss media for the guiding of THz waves. It should be noted that humid air also damps THz wave significantly, so dry air is preferable for low attenuation. High-resistivity silicon also possesses very low material loss at the THz range, but it is not mechanically flexible [11]. Therefore, methods which guide THz waves in air are usually the best solution for low-loss waveguiding. However, finding structures which tightly confine THz waves in air without the use of metal is challenging.

Photonic crystals, which comprise structures having periodic regions with high and low dielectric constants, block modes of certain frequencies from propagating through the structure. The “photonic bandgap” refers to the groups of blocked modes so formed. This effect leads to distinct wave phenomena with useful applications, such as high-reflecting all-dielectric mirrors [10]. A line-defect in a photonic crystal allows the modes in photonic

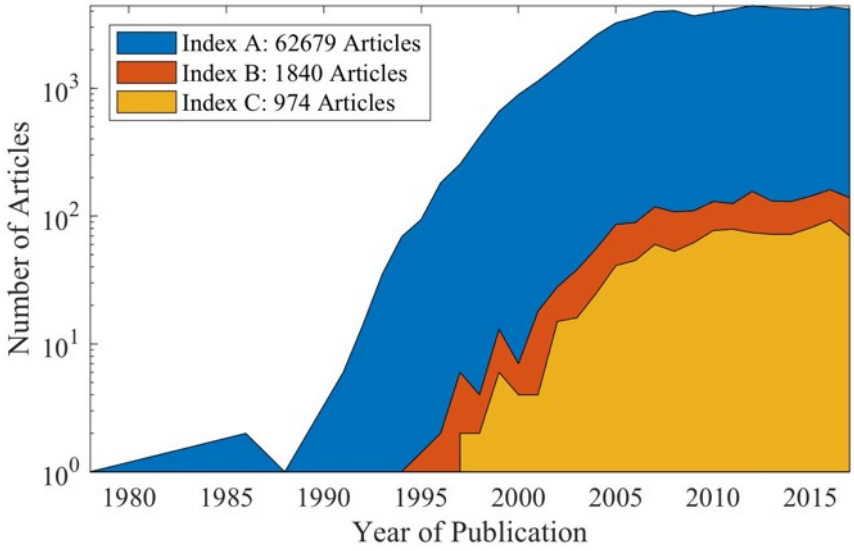

Fig. 1.1 The number of journal articles published per year that discussed the fields of photonic crystals (index A: blue), mmW and THz photonic crystals (index B: orange), and mmW and THz photonic crystal waveguides (index C: yellow). All data collected from Web of Science [12].

bandgaps to propagate within the defect region, thereby forming a waveguide. Replacing metals by photonic crystals in waveguides can reduce the severe ohmic loss at THz frequencies as the cost of introducing a small amount of dielectric loss and confinement loss. Therefore, photonic crystals can be seen as artificial structured materials that are capable of waveguiding THz waves with extremely low loss.

To understand the historical context and growth of the field of mmW and THz photonic crystal waveguides (PCWs), a search based on the Web of Science [12] was conducted, as shown in Fig. 1.1. The search was expanded to include mmW frequencies here since photonic crystal structures also exhibit very interesting properties at mmW frequencies, such as flatness, flexibility, integratability, as well as ease of fabrication. All indexed articles that discuss “photonic crystals” or “mmW and THz photonic crystals” or “mmW and THz photonic crystal waveguides” were noted[1].

[1] Owing to the different naming conventions, the search terms “millimetre,” “sub-millimetre,” “mmW,” “terahertz,” “THz,” “T-ray,” “far-infrared,” “photonic crystal,” “photonic bandgap,” “Bragg fibre,” “waveguide,” and “fibre,” as well as regional spelling variants were also searched.

As Fig. 1.1 shows, the interest in photonic crystals experienced a rapid growth in the 1990s after the term “photonic crystal” being firstly introduced by E. Yablonovitch *et al* [13]. However before that, the bandgap effect in one-dimensional photonic crystals, which is also known as “Bragg reflector” or “Bragg mirror” or “Bragg stacks”, has already been studied in 1976 [14]. The research of photonic crystals is firstly driven by optical applications, such as optical fibres, cavities, sensors, gratings, and photonic integrated circuits. The collision of photonic crystals with mmW and terahertz technology didn’t happen until the mid 1990s. Unlike the explosive development of photonic crystals, very few articles are published on mmW and THz photonic crystals, since most of them discuss optical applications. This may be due in part to the lack of low-loss high-refractive-index mmW and THz materials and suitable fabrication techniques. Among all studies on mmW and THz photonic crystals, about half of them investigates waveguides or fibres. Therefore, the study of waveguides still remains at the core of the field of mmW and THz photonic crystals, and studying it may pave the way for an increased interest in THz functional components and, in due course, THz system in package (TSiP) concepts.

1.1 Review of THz waveguides

The THz spectrum is located in the gap between the well-developed microwave and infrared spectral regions. Waveguides in the THz frequency range are well poised to benefit from techniques and technologies from both electronics and photonics, i.e., rectangular/circular metal waveguide [15, 16], parallel-plate [17, 18], metal wire [19, 20], planar and coaxial transmission lines [21 - 24], substrate-integrated waveguide [25, 26], sub-wavelength polymer fibre [27, 28], dielectric tube [29 - 31], dielectric-lined hollow metallic waveguide [32 - 35], and microstructured fibre [36 - 54].

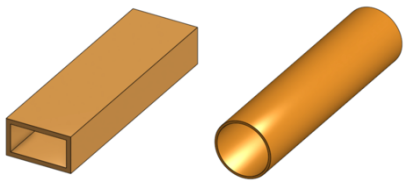

Hollow metallic rectangular and circular waveguides play an essential role in packaging sources, passive components, and detectors into conventional microwave systems. Hollow metallic waveguides function well at microwave frequencies, but as the frequency extends to high terahertz frequencies, the size of hollow metallic waveguides decreases to the sub-millimetre scale, which is a severe challenge for metal processing. Besides, the ohmic loss of hollow metallic waveguides is significant, which may greatly decrease the performance of THz systems since the power of

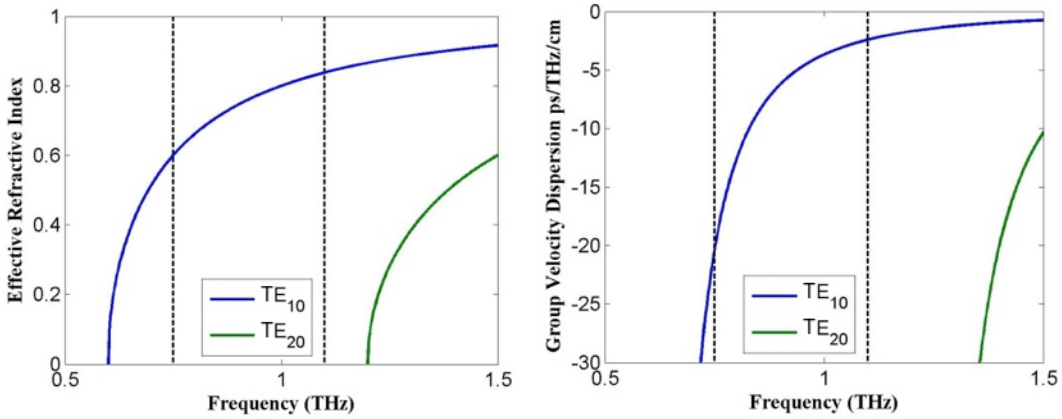

Fig. 1.2 Dispersion curves (left) and group velocity dispersion (right) for the lowest two modes in the WR1.0 rectangular waveguide.

THz sources are generally much lower than the power of microwave sources. In addition, hollow metallic waveguides experience strong group-velocity dispersion near the cut-off frequency of the guiding modes, since they do not support transverse electromagnetic modes which have no cut-off frequency. Generally, compared with standard metallic circular waveguides, standard metallic rectangular waveguides have a much larger bandwidth which allows only one mode to propagate. A rectangular waveguide, whose height to width ratio is 0.5, allows a single-mode operation bandwidth of 2:1 (the ratio of the upper band edge to lower band edge) or an octave, while the highest possible bandwidth of circular waveguides is only 1.36:1. In order to limit dispersion and avoid evanescent-wave coupling with higher order modes in standard hollow metallic rectangular waveguide, the lower edge of the band is usually approximately 30% higher than the waveguide's cut-off frequency, and the upper edge of the band is approximately 5% lower than the cut-off frequency of the next higher order mode. For instance, the rectangular waveguide WR-1.0 (WR-10) used by Virginia Diodes Inc. to cover the bandwidth 0.75-1.1 THz (75-110 GHz) has an estimated waveguide loss between 1.92 (0.061) and 1.35 (0.043) dB/cm at the low and high end of the band, respectively [55]. Fig. 1.2 shows the dispersion curves and the group velocity dispersion (GVD) of WR1.0 with gold-coated walls. It can be seen that the GVD for the lowest two modes in the WR1.0 in the suggested single-mode band is relatively large. The GVD is responsible for dispersive temporal broadening or compression of signals. For applications like spectroscopy or communication, the GVD is desired to be zero or close to zero to reduce the effect of the signal distortion.

Oversized rectangular and circular waveguides have also been investigated, both theoretically and experimentally [56 - 58]. Quasi-optical

techniques are used to efficiently couple freely propagating pulses of THz electromagnetic radiation into hollow metallic circular and rectangular waveguides [57]. A completely classical waveguide theory is typically utilized to calculate the coupling coefficient into the modes of the waveguide for the incoming linearly polarised and focused THz pulses, which can be treated as a plane-wave Gaussian beam. The propagation of the THz pulse through the waveguide is then described as a linear superposition of the coupled propagating modes with a unique complex propagation vector separately. The study [57, 58] shows that the linearly polarized incoming THz pulses significantly couple only into the TE_{11}, TE_{12}, and TM_{11} modes of the circular waveguide and the TE_{10} and TM_{12} modes of the rectangular waveguide. By suitably setting the beam waist of the Gaussian beam, and the size of the waveguides, coupling of the THz pulse to only one mode of the waveguide over many octaves in frequency can be performed. A 25 mm long 125 μm ×125 μm rectangular brass waveguide has been experimentally demonstrated to propagate a single TE_{10} mode over the frequency range from 0.7 to 4 THz with low loss [57], and a circular silver waveguide with an inner diameter of 1 mm has been reported to propagate a single TE_{11} mode at wavelengths from 190 to 250 μm with losses lower than 8 dB/m [58].

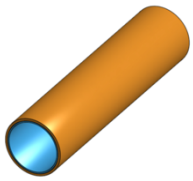

Dielectric-lined hollow metallic waveguides, which introduce a dielectric coating layer on the inner metallic walls of an oversized hollow metallic waveguide, have been intensively studied recently for reducing the propagation loss [32 - 35, 59 - 61]. These dielectric-lined hollow metallic waveguides aim to solve the issue of increasing ohmic losses of single-mode coaxial and rectangular waveguides at terahertz frequencies. In hollow metallic rectangular and circular waveguides, the ohmic losses are caused by the electric field not vanishing entirely on the metallic boundary, but instead penetrating into the wall, where absorption occurs. However, in the dielectric-lined hollow cylindrical metallic waveguide, the hybrid linear-polarized HE_{11} mode and the azimuthally polarized TE_{01} mode experience small absorption due to electric field then vanishing at the waveguide wall [62]. As free-space THz pulses at the focal spot can often be regarded as a linearly polarized plane-wave Gaussian beam, the linearly-polarized HE_{11} mode has a much higher coupling efficiency to the free-space THz pulse compared with the azimuthally polarized TE_{01} mode. By optimizing the thickness of the dielectric cladding and the bore diameter to wavelength ratio, the linearly polarized hybrid HE_{11} mode exhibits the lowest loss and becomes the dominant mode [62, 63]. The other modes, e.g. TE_{11}, TM_{11},

TE_{12}, suffer a significant increase in their attenuation coefficient, which is known as self-filtering. By means of efficient coupling, as with the coupling of freely propagating THz pulses to the fundamental mode in oversized circular waveguides, higher order modes can be further eliminated, thus enabling quasi-single-mode propagation. Therefore, the multimode nature of oversized waveguide is suppressed in dielectric-lined hollow metallic circular waveguide. The effective single-mode THz propagation in polystyrene-lined hollow silver circular waveguide with transmission loss below 1 dB/m and dispersion of 6 ps/THz/m with a bandwidth of at least 1 THz has been reported [35, 64].

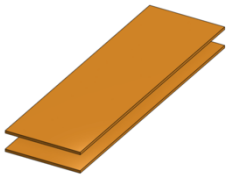

Parallel-plate waveguides consists of two parallel conducting plates positioned closely together [17, 65,66]. Generally, parallel-plate waveguides use the lowest-order transverse-magnetic (TM_0 or TEM) mode or transverse-electric (TE_1) mode as the operating mode. The TEM mode has a uniform electric field perpendicular to the plates under the approximation of perfect electric conductor (PEC), and has no cut-off frequency, so producing exceptional small GVD (zero for PEC plates, or minute real values for conductive metal ones). Since even-symmetry incoming THz field patterns do not couple to the odd symmetry modes in parallel-plate waveguide, and vice versa, the theoretical single-mode band for TEM is the band lower than the cut-off frequency of TM_2 mode. However, even if some coupling to the TM_2 mode did occur, it would experience rapid attenuation due to higher absorption than that of dominant TEM mode and thus be filtered out. The single-mode band for the TEM mode is therefore much wider than the theoretical value in practice. For instance, it is reported that undistorted, low-loss (0.61 dB/cm at 1 THz) single-TEM-mode propagation of the incoming 0.3-ps FWHM THz pulses can be observed over the frequency range from 0.1 to 4 THz through a 24.4 mm long copper parallel plates with a plate separation of 108 μm, which is much higher than the cut-off frequency of TM_2 mode (2.78 THz) [17]. In contrast, the electric field of TE_1 mode is orientated parallel to the plates, and has a cut-off frequency which causes spectral filtering and introduces high GVD, which results in a broadening and reshaping of the input broadband THz pulses. This was confirmed in Ref. [66], where a picosecond-scale input pulse propagating through aluminium plates with a plate separation of 0.5 mm was broadened to more than 150 ps, strongly reshaped, and exhibited a negative chirp. Nevertheless, it was also observed that the TE_1 mode exhibits extremely low loss (3.3×10^{-6} dB/cm at 1 THz) and negligible dispersion, and propagates in a single-TE_1

mode pattern over a wide band in oversized parallel plate waveguide by increasing the plate separation from 0.5mm to 10 mm [66]. The problem of the multimode nature in oversized waveguide is solved by selectively optimizing the coupling between the incoming THz Gaussian beam with the mode of interest via mode-matching. Both TEM and TE_1 modes are suited for the transmission of THz pulse in parallel plates with low loss and low dispersion. The electric field of TE_1 mode has a spatial dependent sine distribution, whereas that of TEM mode has a flat-top profile, and thus the TE_1 mode is matched to Gaussian beam profiles much better than the TEM mode, enabling better coupling and selectivity. The ohmic loss of TE_1 mode is much lower than that of TEM mode since the field vanishes at the wall. In addition, it has been reported that the intrinsic divergence loss in the unguided direction can be reduced by exploiting slightly concaved plates [65]. Overall, the TEM mode or TE_1 mode can be excited if the incoming THz Gaussian beam is polarized parallel or perpendicular to the plates, respectively.

Bare metal wire, also known as Sommerfeld wire, consists of a cylindrical metallic wire conductor. The dominant mode of bare metal wire is a cylindrically symmetric radial transverse magnetic mode (TM_{01}) which is also known as Sommerfeld wave [67]. It propagates as a weakly guided radial surface wave along the conductive surface of the bare metal wire, as thus is a form of surface plasmon wave. It has been measured that, for a metal wire with 0.9 mm in diameter, the time-domain waveforms have no evident change after a propagation distance of 24 cm, which indicates the propagation is essentially dispersionless and the attenuation can be as low as 0.01 cm^{-1} at 1 THz [19]. Since the interaction area between the electromagnetic field and the metal wire is a small surface, much smaller relatively than other metallic waveguides, the ohmic loss of the metal wire is relatively low concomitantly. However, due to the weak confinement of the TM_{01} mode, even mild geometric perturbations, such as bending, may lead to high radiation losses, indicating that the radiation loss is one of the main reasons which limit its practicable applications [68]. In addition, the coupling loss of the free-space THz beam to the guided mode is quite large, since the polarization of guided mode and the incoming THz Gaussian beam are poorly mismatched. Some efforts have been made to reduce the radiation loss and increase the coupling efficiency. A photoconductive antenna with radial symmetry can be used to emit a radially polarized THz beam, maximizing the spatial overlap between the polarization of the input THz beam and the radial symmetry of

the transverse magnetic mode (TM_{01}) [69], thus enhancing the coupling efficiency. Similar to the bare metal wire, a two-wire waveguide can also be used to carry the terahertz wave in air with low loss (0.01 cm^{-1} at 1 THz) and low dispersion [20]. However, the difference is that the dominant mode of two-wire waveguide is TEM mode confined in the small area between the wires, which allows more efficient coupling of the electromagnetic energy into the waveguide.

Subwavelength polymer fibre is a single polymer wire with subwavelength diameter. With a large wavelength-to-diameter ratio, the energy of the propagating modes expands to the air, minimizing the fractional power delivered inside the lossy polymer core [28]. Radiation loss due to nonuniform diameter variation and fractional material absorption due to absorptive polymer core are two dominant loss mechanisms for the subwavelength polymer fibre [70]. Owing to the efficient quasi-optical coupling of the free space THz sub-ps pulses to the propagating HE_{11} mode, subwavelength polymer fibre exhibits single-HE_{11} mode propagation over a wide band, regardless of the multimode nature of the subwavelength dimensions of the fibre [71]. However, the group velocity dispersion of the HE_{11} mode is significant. It is reported that a 0.6 ps incident THz pulse propagating through a subwavelength sapphire fibre with 325 μm diameter and 8 mm length is broadened to approximately a 10 ps pulse [71]. A propagation loss at 0.3 THz was reported to be of the order of or less than 0.01 cm^{-1}, but when the frequency extended to higher terahertz band the attenuation increases significantly [70]. Besides, in order to achieve a large wavelength-to-diameter ratio, the diameter of the fibre decreases to the tens of microns scale for the transmission of higher terahertz pulse, which makes the uniformity of the fibre more challengeable. In order to isolate humidity air from other environmental perturbations, a substantial porosity suspended core subwavelength fibre was reported to offer low-loss (0.02 cm^{-1}) single-mode guiding over the continuous bandwidth from 0.28-0.48 THz [72].

Polymer tube waveguides normally consist of a large air core and a thin dielectric hollow cladding. The guiding mechanism is the antiresonance effect of the thin dielectric hollow cladding, which acts as a radial Fabry-Perot etalon. Owing to the antiresonance effect, a series of low loss transmission bands is separated by frequencies with high loss which satisfy the resonance condition of the thin cladding [73]. The spacing of the resonance frequencies

is inversely proportional to the refractive index and the thickness of the cladding [29]. However, a uniformly thin cladding is fragile and difficult to fabricate in practice, and materials with appropriately low refractive index are rare. Moreover, tube waveguides with thin claddings are sensitive to external perturbations, since the propagating mode extends significantly outside the cladding. In addition, the low loss and low dispersion propagation of terahertz waves in polymer tube waveguides always require a large diameter of the air core, which leads to multimode transmission, and thus the single-mode transmission is sensitive to the coupling efficiency, leading to limited beam quality and beam stability. It has been reported that Teflon tube with a large core (9 mm) and a thin wall (0.5 mm) offers low loss (less than 0.005 cm^{-1}) transmission of THz waves (a passband of 200 GHz centred near 400 GHz) [29]. In order to overcome the band limits due to antiresonance reflection, a high-loss, thick PMMA cladding has been introduced to minimize the antiresonance reflection by absorbing the propagating field in the cladding and thus preventing it from being reflected into the core where the interfere occurs [30]. This PMMA tube waveguide is reported to offer low loss (0.05-0.5 cm^{-1}) and low dispersion (<10 ps/THz/cm) in the 0.3-1 THz range [30].

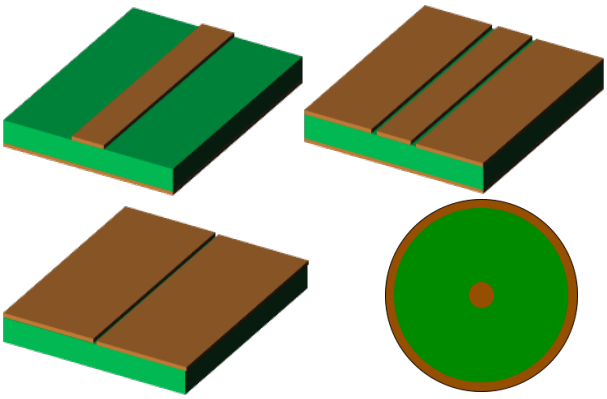

Transmission lines, including microstrip, stripline, coplanar, and coaxial transmission lines, are widely used in terahertz time-domain spectroscopy (THz-TDS) system for the generation of sub-ps-THz pulses. However, the transmission lines have not been considered for the transmission of THz pulses, mainly due to high attenuation and dispersion [22]. The electromagnetic wave carried by microstrip and coplanar exists partly in the dielectric substrate, and partly in the air above it, while coaxial transmission line delivers TEM modes in the dielectric area between the two coaxial conductors. Microstrip and coplanar transmission lines both suffer from high dispersion due to the dielectric substrate and strong frequency dependent loss due to Cherenkov-like radiation. The coaxial transmission line has low dispersion due to the TEM mode having no cut-off frequency, but it still has high loss owing to the finite conductivity of the metal. Reported propagation losses at 1 THz for microstrip, coplanar waveguide, stripline and coaxial cable are

approximately α_{ms}=10 cm^{-1}, α_{cpw}=15 cm^{-1}, α_{st}=6 cm^{-1}, and α_{coax}=0.48 cm^{-1}, respectively [21 - 24].

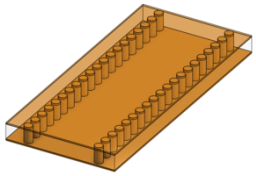

Substrate integrated waveguides (SIW) provide a promising platform for millimetre-wave integrated circuits due to their ease of integration and printability [25, 26]. However, at THz frequencies, the loss of dielectric-filled SIW is mainly limited by high material absorption loss [25], while the loss of hollow SIW converges to the high ohmic loss [26]. In addition, the metal vias are very difficult to make, especially in the THz range. It has been reported that a SIW works at 500 GHz with a propagation loss less than 3.5 dB/cm [25]. Compared with conventional SIW, hollow substrate integrated waveguide (HSIW), which is also known as air-filled SIW, can reduce the propagation loss substantially by mainly guiding the electromagnetic field in the air core [26, 74, 75]. HSIW has been reported to work over the Ka-band with a minimum loss of about 0.045 dB/cm around 34 GHz [74].

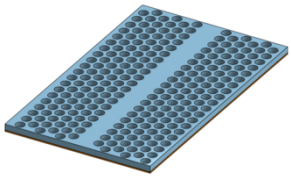

Photonic crystal slab waveguides [76-78] show very low loss and low GVD, but their performance is significantly affected by both the substrate and superstrate, which is why they are usually suspended in the air. Bends in the PC slab waveguide also greatly decrease the bandwidth owing to the discontinuities at the bends and the incomplete photonic crystal bandgap. Propagation loss of less than 0.1 dB/cm and bending loss as small as 0.2 dB/bend working over the frequency range from 0.326 to 0.331 THz are reported [76]. It is also recently reported that a PC slab waveguide works between 0.54 ~ 0.63 THz with a mean propagation loss of 4 dB/cm.

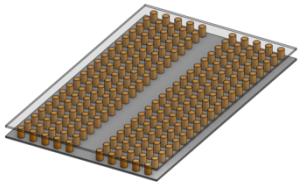

Hollow photonic crystal waveguide (HPCW) [79, 80] is made up of line-defect metallic photonic crystals sandwiched by two parallel metal plates. In the horizontal direction, the wave is confined in the air core by metallic photonic crystals due to the photonic bandgap effect, while in the vertical direction, the wave bounces between the two parallel metal plates. Gold-coated square lattice rods sandwiched by aluminum parallel-plate waveguide is reported to work over the frequency range between 0.65 ~ 1.0 THz with a propagation loss less than 1.74 dB/cm with a minimum of about 0.87 at 1 THz [80].

Ribbon waveguide [81, 82], confines the wave in a high-refractive-index dielectric core via the total internal reflection effect, and has been reported

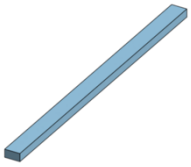

in the frequency ranges of 100 to 130 GHz [82] and 440 to 550 GHz [81] with a propagation loss of less than 0.087 dB/cm and 1.04 dB/cm, respectively. Ribbon waveguides are sensitive to the surrounding materials, and thus supporting structures are usually needed to keep them suspended in the air.

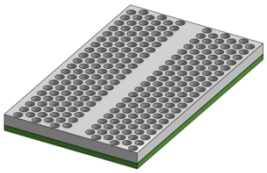

Substrate integrated image guide (SIIG) comprises of a dielectric core and two porous sidewalls. The effective refractive index of the porous sidewalls is smaller than that of the dielectric core. Thereby the wave is guided in the dielectric core via total internal reflection effect. It is reported that a SIIG is demonstrated to work between 85 GHz to 105 GHz with a mean propagation loss of 0.35 dB/cm [83].

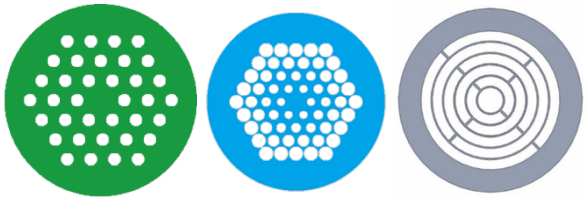

Microstructured fibres, including photonic crystal fibres, have been intensively studied in the optical frequency range since 1996 when the first all-silica endless single-mode photonic crystal optical fibre was fabricated [10, 84], but they are now an area of active field for the delivery of terahertz waved [36 - 53]. Amongst these microstructured fibres, some air-core microstructured fibres stand out as particularly promising [39, 42, 43, 46, 48 - 52]. A spider-web porous fibre fabricated by extrusion has been demonstrated with loss better than 35 dB/m between 0.2 and 0.35 THz with a minimum loss of 1.3 dB/m at 0.24 THz, but single-mode operation is not claimed in the work [48]. Using three-dimensional (3D) printing technology, a hollow core fibre with a triangular-lattice cladding around an air cylinder was demonstrated operating near 0.105 THz with 30 dB/m propagation loss [42]. A 3D-printed kagome-lattice THz waveguide with average propagation loss of 8.7 dB/m over three antiresonance windows in the frequency range from 0.2 to 1.0 THz has also been presented [49]. In addition, using 3D stereolithography, a hollow core Bragg fibre with propagation loss of 52.1 dB/m at 0.18 THz [50] was recently reported. In 2011, two rolled large air-core Bragg fibres were reported which exhibited propagation losses of 18 dB/m at 0.69 THz and 12 dB/m at 0.82 THz, respectively [43]. Recently, tube-lattice fibers fabricated with a fiber drawing technique have been demonstrated, in which the electromagnetic (EM) fields are guided in the low-loss air core, based on the antiresonance effect [51, 52]. The latest experimental work on a tube-lattice fiber showed a propagation loss of approximately 5 dB/m in the fundamental transmission

window around 0.27 THz can be achieved, and losses of 1 dB/m in higher order transmission windows were inferred, those latter were too low to measure reliably [52]. However, as a type of anti-resonant fiber, the tube-lattice fiber in [52] supports a high number of modes, especially in higher order transmission windows due to the relatively large core size, resulting in mode-competition problems [85, 86]. Triangular-lattice microstructured fibers fabricated by stacking were also shown to guide terahertz waves [39, 46], with a propagation loss less than 0.87 dB/m around 0.77 THz achieved [46]. These air-core microstructured fibers [39, 46] exhibit relatively low loss as they are able to tightly confine the EM field in the low-loss air core, based on either the photonic bandgap effect [87, 88] or the antiresonance effect [89, 90], but single-mode operation in these microstructured fibers was not claimed. A dielectric-lined hollow cylindrical metallic waveguide is a very promising structure, having achieved propagation loss of 1 dB/m at 2.54 THz [35]. It can enable quasi-single mode propagation by means of efficient coupling, but multimode interference was also reported which caused measurement difficulties.

The guiding mechanism of microstructured fibre can be divided into three classes: photonic bandgap effect, modified total internal reflection, and antiresonance reflection. The photonic bandgap effect requires a strictly periodic structure in the cladding, and the light is confined with the core as the transverse propagation in microstructured cladding region is made impossible by the periodic structure. The modified total internal reflection in microstructured fibre is similar to the total internal reflection in conventional step index guiding optical fibre. The effective index of the core is higher than the effective index of the cladding. The core can be either solid or microstructured, and the cladding can be either microstructured or air [41, 91, 92]. In antiresonance reflection microstructured fibre, each cladding layer can be considered as a Fabry-Perot like resonator. The wavelengths corresponding to low and high transmission of terahertz wave are referred as resonant wavelengths and antiresonance wavelengths, respectively.

Strictly periodic structures are not necessary for both modified total internal reflection and antiresonance reflection microstructured fibre [92, 93]. Moreover, the guiding mechanism may vary among aforementioned mechanisms in the same microstructured fibre depending on the frequency of interest [44, 94]. According to different structures, the family of microstructured fibre can be commonly divided into three classes: air-core,

Table 1.1 Review of THz microstructured fibres

Reference No.	Minimum Propagation Loss (L_{min})		Propagation Loss (L) or Average Propagation Loss(L_{avg})		Material	Fabrication Technique
	Loss (dB/cm)	Frequency (THz)	Loss (dB/cm)	Frequency Range (THz)		
[48] ‡	= 0.013	= 0.24	L_{avg} < 0.347	0.2 ~ 0.35	Cylic-olefin Copolymer	Extrusion
[42]	= 0.304	= 0.105	0.304 < L_{avg} < 2.82	0.08 ~ 0.24	n/a	3D printing
[49]*	= 0.043	≈ 0.27	0.043 < L_{avg} < 0.347	0.2 ~ 0.35	Stratasys® VeroWhitePlus	3D printing
[50]*	≈ 0.516	≈ 0.17	0.516 < L < 1.519	0.145 ~ 0.207	Asiga® PlasClear	3D printing
[43]†	= 0.122	= 0.69	0.122 < L < 1.303	0.1 ~ 2	PTFE & PMMA	Rolling
[51]*	= 0.3	= 0.375	0.3 < L < 2.5	0.29 ~ 0.47	PMMA	Drawing
[52]*	= 0.05	≈ 0.27	0.05 < L < 0.8	0.2 ~ 0.35	Zeonex	Drawing
[46] ‡	= 0.0087	= 0.77	n/a	n/a	PTFE	Stacking
[39]†	≈ 1.564	≈ 1	L_{avg} = 2.606	0.65 ~ 1	PMMA	Stacking
[53]	< 0.0695	= 0.88	L_{avg} < 0.1	0.78 ~1.02	TOPAS	Drilling & drawing
[41]	< 0.217	≈ 0.5	L_{avg} = 0.391±0.087	0.2 ~ 0.8	TOPAS	Drilling & drawing
[36]	≈ 0.434	≈ 0.3	0.434 < L < 1.737	0.2 ~ 1.2	Zeonex	Drilling & drawing
[40]†	< 0.052±0.0434	= 0.249	L_{avg} < 1.303	0.05 ~ 0.5	LDPE	Moulding & drawing
[45]	= 0.869	= 1.3	L_{avg} < 4.78	1 ~ 1.6	PMMA	Drilling
[47]	n/a	n/a	L < 2.172	> 0.6	HDPE	Stacking & fusing
[54] ‡	≈0.03	= 0.265	L_{avg} < 0.05	0.246 ~ 0.276	EnvisionTEC® HTM140	3D printing

* Each of these papers reported a microstructured fibre with multiple transmission windows. Only the results of the closest transmission window compared to the frequency range of interest of this work (from 0.246 to 0.276 THz) are presented in this table.
† Each of these papers reported multiple designs of microstructured fibres. Only the result with lower loss from each publication is presented in this table.
‡ A detailed comparison between these low loss microstructured fibres can be found in Chapter 3.

Table 1.2 Review of mmW and THz planar transmission lines and flat waveguides

Reference No.	Representative Propagation Loss (L_{rep})		Propagation Loss (L) or Average propagation loss (L_{ave})		Type	Material	Fabrication Technique
	Loss (dB/cm)	Frequency (GHz)	Loss (dB/cm)	Frequency range (GHz)			
21	43.4	1000	L<50	DC ~ 1000	Microstrip	Cyclotene / Aluminium	Electron beam evaporation / spin coating / Polymer curing / Lithography
22	65	1000	L<65	DC ~ 1000	CPW	GaAs / Ti / Au	Photolithogaphy
23	26	1000	L<26	DC ~ 1200	Stripline	Silicon-on-Sapphire substrate / Aluminium	Photolithography
25	3.5	500	$3<L<3.5$	150 ~ 500	CPW / SIW	Fused silica / copper	Photolithography / Waterjet drilling / Metal sputtering
26	-	-	L_{ave} =0.09	26.5 ~ 40	HSIW	Air / Dupont GreenTape 9K7	LTCC / Laser direct structuring / Screen printing
74	0.045	34	L_{ave} = 0.05	26 ~ 36	HSIW	Air / Rogers RT/duroid 6002	Laser direct structuring / Vias metallization
76	-	-	L<0.1	326 ~ 331	PC slab Waveguide	High-resistivity silicon	Photolithography / Plasma etching
77	-	-	L_{ave} =4	540 ~ 630	PC slab waveguide	High-resistivity silicon	Optical lithography
80	0.87	1000	L <1.74	650 ~ 1000	HPCW	Gold Aluminium SU-8 Silicon	Optical lithography / Metal sputtering
81	-	-	L_{ave} =0.087	100 ~ 140	Ribbon	High-resistivity silicon	Photolithography / Deep reactive-ion etching
82	=0.18	481.5	L_{ave} =0.54	440 ~ 500	Ribbon	High-resistivity silicon	Photolithography / Deep reactive-ion etching
83	-	-	L_{ave} =0.35	85 ~ 105	SIIG	High-resistivity silicon	Laser direct structuring

solid-core, and microstructured core waveguides. The air core microstructured fibre tends to guide the mode in the low loss air core through either photonic bandgap effects [95] or antiresonance reflection [46, 93], which are not to be confused, while the solid core and microstructured core fibre guides the mode in polymer or polymer/air core via modified total internal reflection [92] or antiresonance reflection [96].

In the past decade, much efforts has been dedicated to experimental work in microstructured fibre and flat waveguides. A summary of the properties of mmW and THz microstructured fibres and flat waveguides are listed in Table 1.1 and Table 1.2, respectively. This thesis aims to make contributions to these two types of THz waveguides for the low-loss single-mode guidance of mmW and THz wave.

1.2 mmW and THz materials

The materials typically used for mmW and THz microstructured fibres and flat waveguides are shown in Table 1.1 and Table 1.2, respectively. For THz microstructured fibres, all of the materials commonly used are polymers, including TOPAS, Zeonex, PTFE, HDPE, PMMA, and other 3D printing materials. Using THz-TDS system [97], most of these polymers are measured, and their THz dielectric properties are shown in Fig. 1.3. From Fig. 1.3(a) and Fig. 1.3(c), common polymers, such as TOPAS, PTFE, and HDPE, are less dispersive than 3D printing materials around 1 THz. From Fig. 1.3(b) and Fig. 1.3(d), the material absorption of 3D printing materials are generally higher than that of common polymers. Among them, TOPAS, which is a kind of cylic-olefin copolymer (COC), possesses the lowest material absorption coefficient with moderate refractive index, making it a common choice as the host material for THz microstructured fibres [41, 53].

For flat waveguides, as shown in Table 1.2, the most common material is high-resistivity silicon. High-resistivity silicon has high refractive index and extremely low loss for frequencies below 2.5 THz, and it is a favorited material for flat THz photonic crystal waveguides benefiting from mature silicon technologies, such as photolithography and plasma etching, though it is incompatible with fibre fabrication using extrusion or drawing techniques [10, 67]. Some other dielectric materials have been proposed as promising host materials for flat THz waveguides, such as fused silica [25], aluminium oxide (Al_2O_3) [98], and gallium arsenide (GaAs) [22]. Along with the above-mentioned polymers, the mmW and THz dielectric properties of typical materials are listed in Table 1.3.

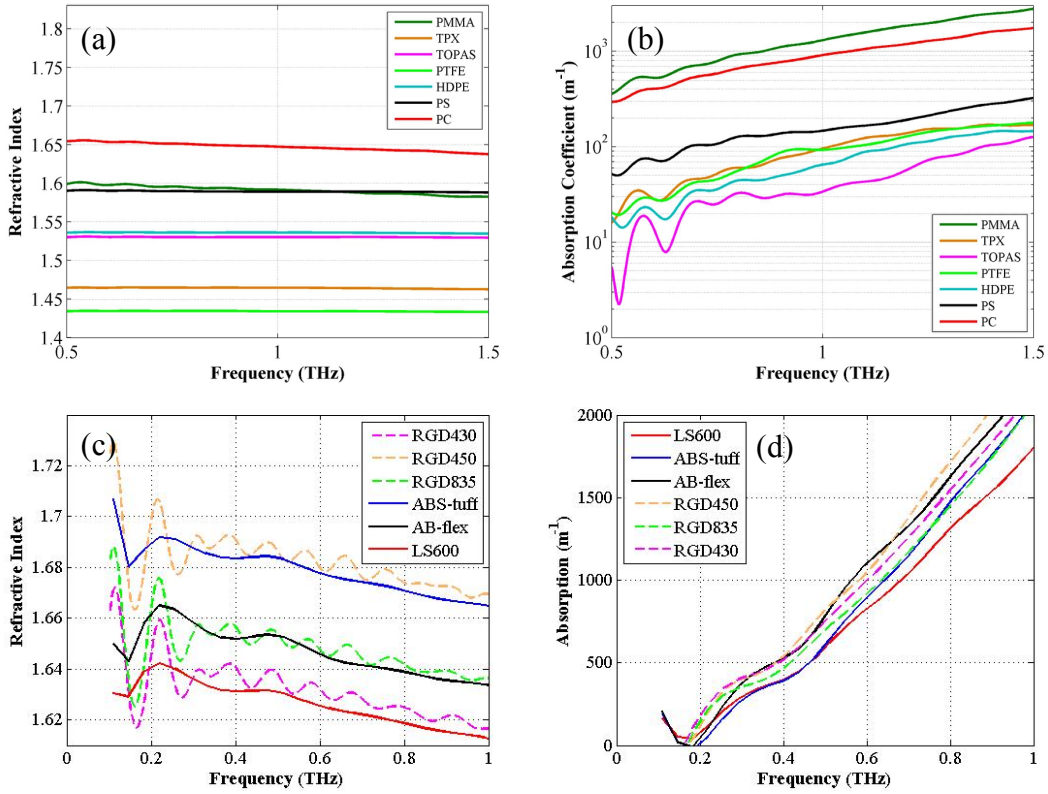

Fig. 1.3 Terahertz dielectric properties of polymers. (a) Refractive index and (b) absorption coefficient of some common polymers obtained from GoodFellow Inc.; (c) Refractive index and (d) absorption coefficient of some 3D printing materials. RGD430, RGD450 and RGD835 are obtained from Stratasys Inc., and ABS-tuff, AB-flex, and LS600 are obtained from EnvisionTEC Inc.

Overall, for the photonic crystal structures emphasized in this thesis, high-refractive index and low-loss materials are desirable to create a significant bandgap, although in reality trade-offs between the favorited properties of the materials and the feasible fabrication techniques have to be made. For

Table 1.3 mmW and THz dielectric properties at representative frequencies.

Material	Permittivity	Refractive Index	Absorption Coefficient (m^{-1})	Loss Tangent	Measured Frequency	Data Source
High-resistivity Silicon	11.676	3.417	1.5	2.095E-05	1 THz	[11]
InP	12.33	3.511	662.34	0.009	1 THz	[99]
Al_2O_3 (99.6%)	9.3	3.05	191.77	0.003	1 THz	
Fused Silica	3.818	1.954	200	0.0049	1 THz	[100]
High-resistivity GaAs	12.924	3.595	60	0.0008	1 THz	

Rogers RT/duroid 5880LZ	2	1.414	0.622	0.0021	10 GHz	[101]
Rogers RT/duroid 5880	2.2	1.483	0.28	0.0009	10 GHz	
Rogers RO3010	11.2	3.347	1.543	0.0022	10 GHz	
Rogers RT/duroid 6010LM	10.7	3.271	1.577	0.0023	10 GHz	
Zeonex	2.313	1.521	21	0.00066	1 THz	[36]
TOPAS	2.341	1.53	33.98	0.00106	1 THz	Measured at Leeds using THz-TDS system by the author
PTFE	2.056	1.434	93.01	0.00309	1 THz	
HDPE	2.359	1.536	65.09	0.00202	1 THz	
PMMA	2.534	1.592	1307	0.03919	1 THz	
TPX	2.146	1.465	96.14	0.00313	1 THz	
PC	2.712	1.647	910.9	0.02639	1 THz	
PS	2.525	1.589	147.1	0.00442	1 THz	
ABFlex	2.799	1.674	2390.3	0.06821	1 THz	
ABStuff	2.776	1.667	2094	0.05999	1 THz	
LS600	2.727	1.652	1902.8	0.05500	1 THz	
RGD430	2.628	1.622	2129.5	0.06270	1 THz	
RGD450	2.766	1.664	2449.2	0.07032	1 THz	
RGD835	2.674	1.636	2056.8	0.06004	1 THz	
HTM140	2.689	1.64-0.02288i	959.1	0.02791	300 GHz	Measured at Leeds using VNA free-space material characterization platform by the author

THz microstructured fibres, Zeonex or TOPAS are promising low-loss material which suit for the fibre fabrication techniques. As for mmW and THz flat waveguides, high-resistivity silicon is a popular choice.

1.3 Fabrication Techniques

1.3.1 Fabrication of microstructured THz fibres

For most of the reported microstructured THz fibres, fabrication usually involves moulding, drilling, stacking, rolling, 3D printing, solvent deposition, extrusion, and drawing, as can be seen from Table 1.1. Except for 3D printing, all above-mentioned fabrication techniques are widely used in the fabrication processes of optical and infrared polymer microstructured fibres and they usually have two stages [10, 102]. The first stage of the fabrication of an optical or infrared fibre is the construction of a preform which is a scaled-up (larger in diameter, shorter in length) version of the fibre which contains the necessary transverse microstructures and essential materials. In the second stage, the fibre preform is **drawn** to form a fibre using a

drawing tower which involves heating the preform to a temperature sufficiently larger than the glass transition temperature of the polymers to reduce its viscosity so that it can be drawn to fibre. The process may also involve intermediate stages, such as drawing the initial preform to an intermediate size called a “cane”, sleeving to increase diameter, or by stacking several canes to form a new preform [103]. However, on some occasions, due to the larger dimensions of THz waveguides compared to that in optics or infrared, no fibre drawing is required since the waveguide preform is suitable by itself for THz guidance. Much effort has focused on the primary preforms: stacking of capillary tubes, drilling holes in the bulk material, moulding/casting into a microstructured mould, extrusion, and so on.

Drilling is the first method used to fabricate microstructured optical fibre [104], and it has also been widely employed in THz range [36, 41, 45, 53]. The fabrication of a fibre made by drilling holes in the preform is very time consuming for a large number of holes, and this technique is not adequate for fabrication of fibres with high porosity due to the mechanical constraints of the hole size and the wall thickness between the holes [105]. In addition, the shape of the holes is limited to the circular shape and the length of preform.

The high porosity required for some microstructured fibre designs led to the investigation of **stacking**. To fabricate preforms through the stacking technique, the rod, tubes or capillaries are assembled in a hexagonal array [39, 46, 47] or other regular arrangement [106], and placed into a protective cladding to hold the arrangement securely in place. The advantage of this technique is that very large air fractions can be achieved by using very thin-walled tubes [106, 107].

Another technique employed for fabrication of microstructured THz fibres is **moulding**. Two different approaches are considered for this purpose: a sacrificial polymer technique, and microstructured moulding technique [40, 67]. For the former approach, a sacrificial polymer which has significantly higher glass transition temperature than the main material of the microstructured THz fibre is placed in the air region of the preform; the main material then consequently fills out the space between the sacrificial polymer by melting. After that the fabricated preform is then drawn into a fibre, and finally the air holes in a fibre are revealed by dissolving the sacrificial polymer without affecting the rest of the fibre. For the latter approach, the fibre preform is constructed by casting main material into a microstructured

glass mould. The glass moulds are pulled out from the preform, and any residual glass is etched away before drawing into fibre. Finally, the resultant preform is drawn down using active pressurization preventing hole closure and increasing the porosity. However, the transverse cross-section of the preform may be severely deformed by the active pressurization.

Hollow-core multilayer photonic bandgap waveguides can be fabricated by **rolling** up a thin film with a layer of powders on top of acting as a bridges to maintain the air gap between the layers, or by rolling up a bilayer of thin films with different materials [43]. Apart from the preparation of thin films of materials, these techniques are straightforward, but lack mechanical stability and reproducibility.

As a cost-effective, fast, convenient fabrication technique, **3D printing** is able to produce devices accurately with good repeatability, and hence it has attracted much attention for the fabrication of functional THz components, such as waveguides [42, 49, 50, 54, 108], fibres [109], lenses [110], antenna horns [111] and sensors [50]. 3D printing is also ideal for the fabrication of highly porous structures, which is a challenge for other techniques, such as moulding, drawing, rolling, and extrusion, owing to the deformation encountered during processing [67]. The confident thinnest dielectric wall thickness is larger than 0.4 mm for most commercial 3D printer currently [42, 54]. This feature limits its practical application on THz fibres working above 1 THz which usually contains sub-wavelength features thinner than 0.3 mm. Moreover, the printing materials are limited, and the usually have relatively higher losses than common polymers, such as HDPE, PTFE, etc., which are not adequate for fabrication of ultra-low loss THz fibre [42, 54]. However, due to the relative convenience of fabrication, this technique is usually employed for the demonstration of the fundamental mechanism.

Solvent deposition has been employed to fabricate hollow core polymer THz fibre containing a second polymer (rather than air layers) [44]. The first polymer is dissolved in a nonsolvent of the second and vice-versa. Each layer of the fibre can be deposited and dried non-destructively. In order to achieve an efficient bandgap, a large refractive index contrast is required. However, the refractive indexes of most common polymers are in the range of 1.3 to 2 which is not sufficient for maintaining a large bandgap. An approach to increase the refractive index of polymer is doping a host polymer with high refractive index inclusions (such as TiO_2 particles within a polyethylene host [43]), but this will increase the material loss of the polymer

composite significantly, making it inadequate for fabrication of low loss THz fibres.

Among all the fabrication techniques, the **extrusion** technique is one of the best candidates for the fabrication of the performs for the microstructured THz fibre which enables to continuous manufacture of non-circular preform with either symmetrical or asymmetrical features [105, 112]. Preforms are extruded by heating a bulk polymer billet to a temperature higher than the glass transition temperature, while the soft polymer is then forced through a structured die using a ram extruder at a fixed speed. The transverse cross-section of the preform is determined by the die exit geometry. By using the extrusion technique, the porosity of the preform, which is the scaled-up version of the final fibre structure, can be up to 65% [105]. As mentioned above, the preform by itself is suitable for THz guidance resulting in the elimination of the drawing process. It has been reported that the thickness of the wall in an all-PMMA air core Bragg fibre can be as thin as 0.2 mm [112].

1.3.2 Fabrication of mmW and THz flat waveguides

Table 1.2 shows the techniques involved in the fabrication of representative mmW and THz flat waveguides. Unlike the fabrication techniques of THz microstructured fibres discussed in section 1.3.1, which are diverse, the fabrication techniques of flat waveguides are more convergent. Along with other preparation techniques, like metal sputtering and spin coating, all designs listed in Table 1.2 use laser processing techniques, including laser direct structuring and photolithography. The use of laser processing techniques can mainly be attributed to their high fabrication resolution. Common metal processing techniques include metal sputtering [80], electron bean evaporation [21], and electroplating [74]. Plasma etching or deep reactive-ion etching are used to etch samples with high material thickness to achieve better quality of vertical side walls of etching structures [76, 81]. To be more specific, the fabrication techniques used in the papers listed in Table 1.2 are as follows:

- In Ref. [21], **spin coating** was used to deposit cyclotene resin on aluminum metallized low-resistivity silicon substrate. After the **polymerization** of the cyclotene resin, the signal conductor of the microstrip line was fabricated using **lithography**.
- In Ref. [22], **photolithography** was used to pattern a coplanar waveguide on a 500-μm-thick GaAs substrate.

- In Ref. [23], **photolithography** was used to fabricate a coplanar stripline comprised of aluminum metal lines on a silicon-on-sapphire substrate (SOS).
- In Ref. [25], **waterjet drilling** was used to drill ground vias out of a backside copper coated fused 50-μm-thick silica substrate which is optically transparent. Then the vias and the front surface of the silica substrate were metallized by copper using **metal sputtering**. Finally, **photolithography** was used to pattern the front face of the mode-selective transmission line.
- In Ref. [26], **low temperature co-fired ceramic (LTCC) and laser direct structuring** were used to fabricate a hollow substrate integrated waveguide. Four layers of Dupont® GreenTape 9K7 were firstly stacked and pre-laminated, and then laser direct structuring was used to create vias, cavities and slots in the pre-laminated structure. Then, silver paste was used to fill the vias and metalize the top and bottom layers. Finally, the aligned samples were laminated and co-fired forming the HSIW.
- In Ref. [74], **laser direct structuring** was used in hollow substrate integrated waveguide to create vias, holes and air channel out from Rogers® RT/duroid™ 6002 laminate. Two FR-4 boards with vias aligned with the 6002 laminate were used to sandwich the 6002 laminate creating the HSIW. The vias were metallized using standard PCB processing techniques.
- In Ref. [76], **photolithography and plasma etching techniques** were used to pattern 200-μm-thick 4-inch high-resistivity silicon wafer creating a photonic crystal slab waveguide with lattice constant equal to 240 μm.
- In Ref. [77]**, optical lithography** has been used to fabricate a photonic crystal slab waveguide which is made of high-resistivity silicon [77]. The thickness of the silicon layer is 100 μm. The fabrication accuracy is reported to be 1 μm which is much smaller than the wavelength of mmW and THz frequencies, so this technique can provide very good fabrication quality for mmW and THz waveguides.
- In Ref. [80], **optical lithography and metal sputtering** were used to fabricate a hollow photonic crystal waveguide. A SU-8 layer of 70 μm thickness, placed upon Al coated Si wafer, was exposed using optical lithography and developed into a square lattice rods with a period of 160 μm. The square lattice of SU-8 rods was then metalized by

sputtering approximately 400 nm of gold. After manually removing a row of metalized SU-8 rods, the line-defect square lattice metal rods were mounted into match parallel plate waveguide made by Aluminium and consequently forms the HPCW.

- In Ref. [81], **photolithography and deep reactive-ion etching** techniques were used to fabricate two dielectric ribbon waveguides. The dielectric ribbon waveguides are square. Two high-resistivity silicon wafers with the thicknesses of 585 μm and 385 μm are firstly patterned by photolithography and secondly etched by deep reactive-ion etching, resulting in two square ribbon waveguides with an edge length of 573.68 μm and 373.15 μm, respectively. The etched angle for the large and small ribbon waveguides are 2.5 ^{o} and 1.95^{o}, respectively. Similar techniques was used in Ref. [82] to fabricate a 100 μm thickness rectangular ribbon waveguide made of high-resistivity silicon.
- In Ref. [83], **laser direct structuring** was used to cut SIIG with lattice constant of 0.645 mm and air hole diameter of 0.5 mm out of a 380-μm-thick high-resistivity silicon wafer.

In summary, the thicknesses of waveguides fabricated using photolithography or plasma etching range from 70 μm to 573.68 μm, while waveguides fabricated by LTCC or standard PCB processing technique have more flexible thickness tuning range.

1.4 Concluding remarks

In this chapter, comprehensive reviews of mmW and THz waveguides, materials and fabrication techniques were presented performed, in order to provide a solid support of background material to underpin the research work that will be discussed in the following chapters.

Firstly, a comparison of different types of mmW and THz waveguides was made. When the frequency moves deep into the central THz spectrum from either microwave frequencies or optical frequencies, the traditional waveguides, such as microstrip lines and optical fibres, which are widely used in microwave or optical domains, now meet new challenges at THz frequencies in terms of the propagation loss. All-dielectric air-core microstructured fibres are recent active research topics recently which are promising to provide low-loss guidance of THz signals. Many other efforts have been devoted into the development of flat mmW and THz waveguides

which can benefit compact and multilayer system-in-package (SiP) applications.

Secondly, the properties of various dielectric materials used in mmW and THz waveguides are reviewed. The materials loss is no longer negligible in the THz frequency range, and plays a significant role in the link budget of a THz system, especially when the power of the sources and the sensitivity of the detectors are much lower compared to microwave and optical corresponding components. COC polymers (e.g. Zeonex and TOPAS) and high-resistivity silicon are promising low-loss host materials for microstructured fibres and flat waveguides, respectively.

Finally, techniques used to fabricate mmW and THz microstructured fibres and flat waveguides were reviewed. The fabrication techniques needed for the two types of waveguides are greatly different. For THz microstructured fibres, thermal processing of polymers are widely used, such as extrusion, moulding, and fibre drawing. Among all thermal processing techniques, fibre drawing technique provides the finest fabrication quality, but it also encounters challenges when fabricating highly porous fibres. For flat waveguides, photolithography is commonly adopted because of its highly precise fabrication quality. Commercial photolithography techniques are generally good enough to fabricate flat THz waveguides whose minimum feature scale is about tens of a micron. However, it is challenging for photolithography to fabricate thick layers as the wall of the etched structures will not be very perpendicular to the substrate. That is why that in some waveguides deep reactive-ion etching techniques are used.

1.5 Outline of thesis

This thesis is organized as follows. In chapter 2, a new design principle to manipulate the photonic bandgap of Bragg fibres is proposed. The design principle is called as the generalized half-wavelength condition. It helps to maximize the photonic bandgap at a specific value of effective refractive index so as to select a right operating mode for the Bragg fibre, and therefore it enables dynamically tuning of the photonic bandgap. With the aid of the novel design principle, an asymptotically single-mode Bragg fibre with the propagation loss less than 1.2 dB/m operating over the frequency range from 0.85 to 1.15 THz is designed and verified by simulation. In Chapter 3, a sub-THz Bragg fibre is fabricated using 3D printing technology. It has been characterized to be less than 3 dB/m operating from 0.245 to 0.265 THz, which is the one of the lowest loss microstructured fibre in the frequency

range from 0.1 to 0.3 THz. In Chapter 4, the mode transition and filtering in the fabricated sub-THz Bragg fibre which is presented in Chapter 3 is investigated using 3D full-wave simulations. The mechanism of asymptotically single-mode operating pattern of Bragg fibres based on modal-filtering effect is revealed, supporting the Bragg fibres to work in single-mode fashion.

Chapter 5 and Chapter 6 present two novel designs of flat hollow photonic crystal integrated waveguides. The design concept are similar between the two types of waveguides, and the operating frequency range of them can be easily scaled to high THz frequencies by changing the lattice constant of the photonic crystal structures. Two proof-of-concept waveguides for each type of hollow photonic crystal integrated waveguide are fabricated and characterized at Ka-band. Good agreements between the measurement results and numerical predictions are observed, validating the design principles.

Chapter 7 presents several designs of functional components based on the previously studied mmW and THz photonic crystal waveguides, including waveguide bends, power splitters or combiners, cavity, h-plane horn antenna, and circular Bragg fibre horn antenna. The expansibility and flexibility of proposed photonic crystal waveguides in terms of manipulating the electromagnetic wave are successfully demonstrated, which make the proposed waveguides strong platforms for building functional components and multilayer packaging.

Chapter 8 concludes the thesis and also points out the potential applications of the proposed mmW and THz photonic crystal waveguides in the fields of THz interconnecting, sensing, and multilayer packaging.

Chapter 2
Modelling and Design of low-loss asymptotically single-mode THz Bragg fibre

In this Chapter, we proposes a novel design of single-TE_{01}-mode small-air-core Bragg fibre working from 0.85 THz to 1.15 THz. It is composed of concentric dielectric layers in air, separated by support bridges. The support bridges act as defects in the photonic crystal structure which can cause mode coupling between the core mode and the surface states, resulting in the increasing of the propagation loss [113]. However, the proposed single-TE_{01}-mode Bragg fibre, which has a null point in the electric field close to the interface between the core and the cladding, can greatly suppress the negative impact of the support bridges on the propagation loss, exhibiting strong superiority over single-HE_{11}-mode Bragg fibre. In addition, unlike conventional single-TE_{01}-mode Bragg fibre which requires a large core, whose diameter is about 7.5 times of the operational wavelength, and 8 cladding layer periods [114], the single-TE_{01}-mode Bragg fibre in this chapter utilise a much smaller core, whose diameter is about 3 times the operational wavelength, and just 4 cladding layer periods. Thus, both the overall size of the Bragg fibre and the need for support bridges for mechanically maintaining the air gaps are greatly reduced. Moreover, the loss discrimination between the desired mode and other unwanted competing modes in the design is about 3 times larger than that of the conventional design [115], resulting in better mode selectivity. Furthermore, we also proposed a generalized half-wavelength condition describing the relationship between the material properties, the geometry, and the photonic bandgap, which provides an efficient technique to manipulate the shape of the photonic bandgap for Bragg fibre. The theoretical calculations indicate that the proposed Bragg fibre can achieve propagation loss less than 1.2 dB/m between frequencies from 0.85 THz to 1.15 THz with only 4 cladding layer periods, which makes it a strong candidate for low loss guidance of THz wave.

2.1 Manipulation of photonic bandgap for Bragg fibre

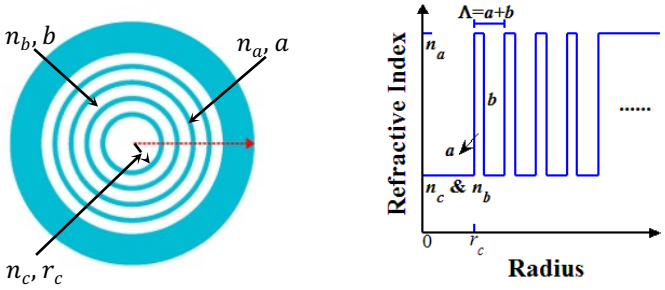

Fig. 2.1 Schematic of an ideal Bragg fibre. (a) The transverse section of the Bragg fibre which is uniform along the z-axis. (b) The radial refractive index profile of the Bragg fibre along the red dashed arrow in (a) starting from the centre and going into the edge.

Fig. 2.1 shows the geometry and the refractive index profile of the proposed Bragg fibre. It comprises an air core ($n_c = 1$) cladded surrounded by periodic concentric dielectric layers of alternatively high (n_a) and low (n_b) refractive index materials, the thickness of which are a and b respectively, while r_c is the core radius and $\Lambda = a + b$ is the period of the radial photonic crystal. The outermost layer is a thick protective layer that will absorb any residual EM waves and isolate the fibre from external perturbations. The dispersion relations and guided mode in Bragg fibre was first derived by Yeh *et al.* [87] A transfer-matrix method can be used to analytically analyse the Bragg fibre, as presented in the Appendix A. Under the cylindrical coordinates, Bragg fibres can be treated as an one-dimensional photonic crystal structure. The periodicity of the photonic crystal structure is about half of the wavelength of interest, so that the EM wave can be diffracted. Whether wave-behaving photons can be transmitted through the photonic crystal structure or not depends on their wavelength, which is known as the photonic bandgap effect. The photonic bandgap can be tailored by artificially changing the geometrical and material properties for manipulating the propagation of the wave-behaving photons. The Bragg fibre utilise the photonic bandgap effect to select the desired operating mode and filter out other unwanted modes, resulting in low-loss and single-mode operation pattern.

The Bragg fibre supports guided modes that are similar to the modes of a hollow metallic cylindrical waveguide. The field of these guided modes mainly distributed in the hollow core, and decays exponentially in the radial direction in the claddings. In Bragg fibre, for guided modes with zero azimuthal mode indices, the modes are exactly TE or TM polarized and are nondegenerate, such as TE_{01} and TM_{01}. For guided modes with nonzero

Table 2.1 Quarter-wavelength conditions

Quarter-wavelength condition	Angle of Incidence
$an_a = bn_b = \lambda_t/4$	$\theta = 0°$
$a\sqrt{n_a^2 - 1} = b\sqrt{n_b^2 - 1} = \lambda_t/4$	$\theta = 90°$
$a\sqrt{n_a^2 - n_t^2} = b\sqrt{n_b^2 - n_t^2} = \lambda_t/4$	$\theta = \text{asin}\,(n_t)$

azimuthal mode indices, TE modes become HE modes, like HE_{11}, and TM modes turns into EH modes, like EH_{11}, and they are doubly degenerate.

In this chapter, Bragg fibres that use air as the core and low refractive index material are investigated, so $n_b = n_c = 1$. There are at least four key advantages for this type of Bragg fibre compared to others with $n_b > 1$: (1) Owing to the high porosity, the vast majority of the THz wave is distributed in lossless dry air; (2) The width of the bandgap is maximized by cladding materials with a high refractive index contrast [116]; (3) The Bragg fibres with $n_b = 1$ show filtering of the unwanted TM modes owing to the Brewster phenomenon [117]; (4) The fabrication process is simplified since the concept is based on only one material, e.g. fabrication by extrusion or drawing. As a result of this, some support bridges or struts are required in order to maintain the air gaps between the dielectric claddings, however. As it is impractical to analyse analytically a practical Bragg fibre with support bridges, an analysis of the ideal Bragg fibre without support bridges is first studied, before the impact of the support bridges on the Bragg fibre is discussed (in section 2.2.5).

To understand the EM-field confinement mechanism, how to obtain the band diagram is first discussed. According to the Bloch's theorem in cylindrical coordinates [118], the constraint which stops the EM field from propagating through into the cladding crystal can be expressed as

$$|\text{Re}(X_s)| < 1 \tag{2.1}$$

where

$$X_s = \left[cos(k_b b) - \frac{i}{2}\left(\frac{\xi_b k_b}{\xi_a k_a} + \frac{\xi_a k_a}{\xi_b k_b}\right) sin\,(k_b b)\right] exp\,(-ik_a a) \tag{2.2}$$

and $k_i = \sqrt{(n_i k_0)^2 - \beta^2}$ $(i = a, b, c)$ is the lateral propagation constant; $k_0 = \omega/c$ is the vacuum wavenumber; ω is the vacuum angular frequency; c is the

speed of light in vacuum; β is the longitudinal constant, $\beta/k_0$is the effective refractive index of the mode (n_{eff}), and ξ_i is 1 or $1/n_i^2$ $(i = a, b)$ corresponding to $S = \mathrm{TE}$ or TM modes, respectively.

The bandgap Eqn. (2.1) can be solved analytically once the geometric (a, b, r_c) and materials (n_a, n_b, n_c) parameters are both known. The quarter-wavelength condition (QWC) has been widely used as a guiding principle to choose the layer thickness [114, 116, 119, 120], as shown in Table 2.1. Here, λ_t is a wavelength of interest which is equal or close to the central wavelength of the photonic bandgap, $n_t = \beta/k_0$ indicates the effective refractive index of interest, and θ is the angle of incidence between the normal line of the surface and the direction of the wavenumber in the plane of incidence. There are at least two disadvantages with the aforementioned QWC treatment: firstly, the QWC only applies for the first order bandgap and thus cannot be used to manipulate higher order bandgaps; secondly, the QWC only maximizes the first order bandgap by making the thicknesses of the cladding layers equal to one quarter of the wavelength of interest; thus, it cannot be used to tune the bandwidth. In practical terms, it is highly desirable that the bandwidth and the shape of any order bandgap can be manipulated for the sake of maximizing the confinement of the desired guiding mode as well as filtering out its competing modes. Therefore, a more flexible and multifunctional design principle than the use of the QWC is required.

2.1.1 The generalized half-wavelength condition

To manipulate the shape of the bandgap in the Bragg fibre, a generalized half-wavelength condition (GHWC) is introduced here, which can be expressed as follows:

$$n_{at}a + n_{bt}b = \zeta\frac{\lambda_t}{2} \tag{2.3}$$

where

$$n_{at} = \sqrt{n_a^2 - n_t^2} \tag{2.4}$$

$$n_{bt} = \sqrt{n_b^2 - n_t^2} \tag{2.5}$$

Here, ζ is an integer indicating the order number of the bandgap. By introducing a porosity factor τ, Eqn. (3) can be split into the following two equations:

$$n_{at}a = \tau\times\zeta\frac{\lambda_t}{2} \tag{2.6}$$

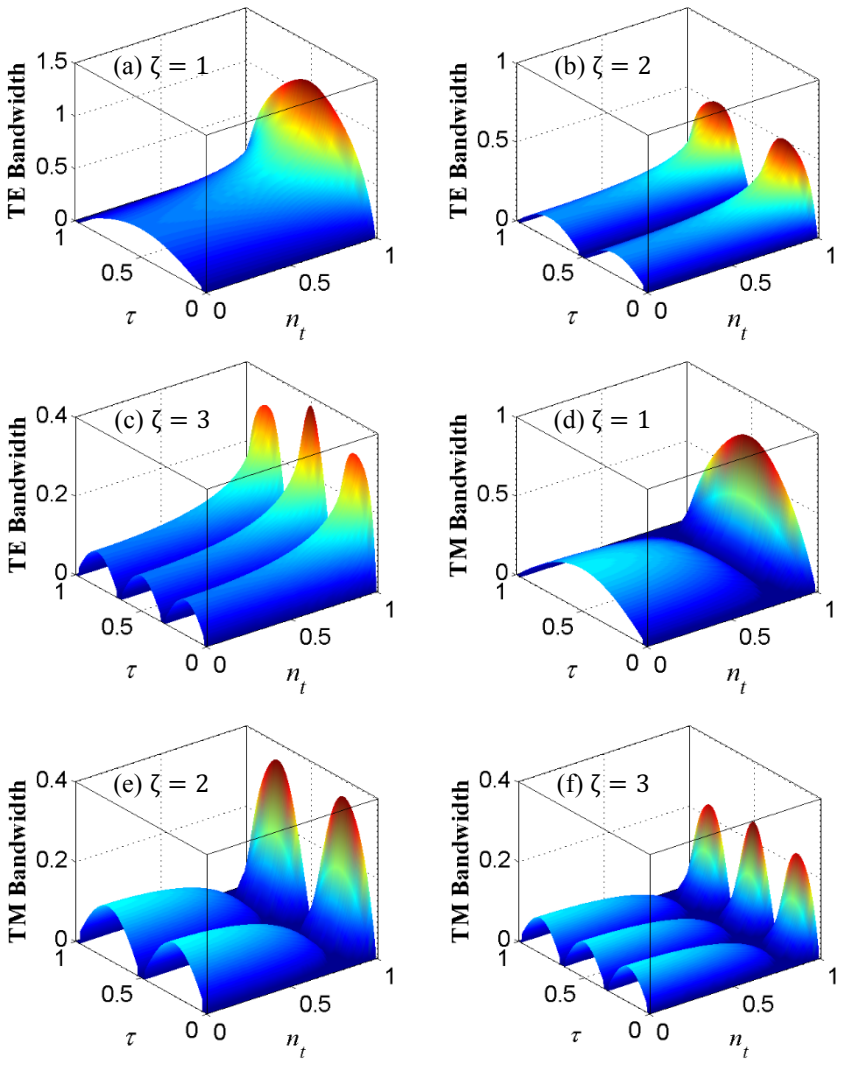

Fig. 2.2 The dependence of midrange ratio bandwidth Δ on porosity factor τ and effective refractive index of interest n_t for different polarisations and different bandgap orders ζ . (a)-(c) correspond to TE/HE polarisations. (d)-(e) correspond to TM/EH polarizations. $n_a = 1.5235$, n_b=1, and the thicknesses a and b are calculated by Eqns. (2.6) and (2.7). The colour map represents the normalized value of bandwidth, decreasing from red to blue.

$$n_{bt}b = (1-\tau)\times\zeta\frac{\lambda_t}{2} \tag{2.7}$$

Therefore, one can obtain the thicknesses of the cladding when the wavelength and effective refractive index of interest are determined. It is noted that if $\tau = 0.5$ and $\zeta = 1$ are elected, the GHWC reverts to the QWC. Thus, the proposed GHWC also covers all solutions provided by the QWC.

As discussed, only $n_b = n_c = 1$ is considered in this design. Generally, a large n_a increases the refractive index contrast of the cladding layers which enables a larger maximum bandgap resulting in greater EM-field confinement in the core [87]. However, the imaginary part of n_a which

accounts for material absorption also significantly influences the performance. At THz frequencies, the choices available for low loss dielectric materials are limited. Silica, which functions well for optical and far infrared applications, has a relatively high loss at THz frequencies [10]. High resistivity silicon shows low loss [11], but does not permit fabrication of fibres. TOPAS is known as a low loss and dispersionless polymer material over the frequency range from 0.2-1.5 THz [10, 41, 53], so this as a representative practical dielectric in the design is chosen. It is also noted that the measurement results of the refractive index of TOPAS in [53] are in good agreement with that in [41], but there are still some minor differences between them. In this chapter, the more recent measurement results in [53] is chosen. Namely, the real part of the refractive index of TOPAS is set to 1.5235, and its absorption coefficient is taken as $\mu\,(\mathrm{dB/cm}) = -0.13 + 0.63(f/1{\times}10^{12}) + (f/1{\times}10^{12})^{2}$ from 0.2 to 1.5 THz. Here, f is the frequency in Hz. However, it is also of interest to investigate the impact of the uncertainty of the refractive index of TOPAS on the performance of the design, so this issue is addressed in section 2.2.3.

Substituting Eqns. (2.6) and (2.7) into Eqn. (2.1) and solving it, the dependence of the bandwidth on n_t and τ for different ζ and different polarisations can be obtained (Fig. 2.2). The bandwidth is defined as the midrange ratio of the bandgap, $\Delta = (f_h - f_l)/[1/2(f_h + f_l)]$, when $n_{eff} = n_t$. Here, f_h and f_l are the upper and lower edge of the bandgap, respectively. From Fig. 2.2, the bandgap for TE modes always expands when n_t increases, while the bandgap for TM modes first shrinks but then expands after a critical point, where the TM bandgap closes up completely. This critical point, n_{B}, is related to the Brewster angle $\theta_{\mathrm{B}} = \mathrm{asin}(n_{\mathrm{B}}) = \mathrm{asin}\,(n_a n_b/\sqrt{n_a^2 + n_b^2})$, according to the Brewster phenomenon for TM/EH modes in Bragg fibre. In the case, since $n_a = 1.5235$ and $n_b = 1$, then $n_{\mathrm{B}} = 0.836$. The Brewster phenomenon reduces the width of the bandgap for TM/EH modes, but does not affect the TE/HE bandwidth. The bandwidth for TM/EH modes is always narrower than that of TE/HE modes for the same n_t, especially near the Brewster angle. This reduces the EM-field confinement of the TM modes and helps to filter them out, which has also been discussed in the previous work [121].

Owing to the Brewster phenomenon, the bandgaps of the TM/EH modes are always narrower than those of the TE/HE modes, resulting in a leaky propagation of TM/EH modes in a Bragg fibre. Thus, the bandgap for the TE/HE modes are more interesting. Comparing Fig. 2.2 (a), (b) and (c), it is

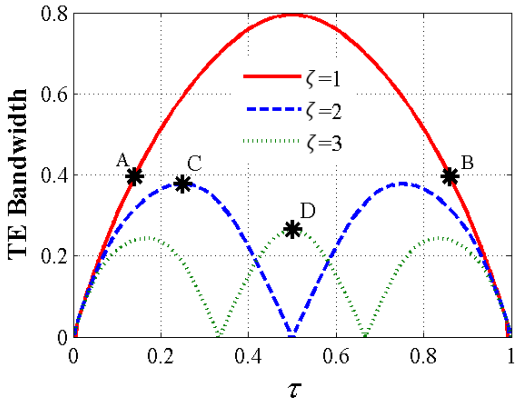

Fig. 2.3 The dependence of midrange ratio bandwidth Δ on the porosity factor τ for different bandgap orders number for TE polarization. $n_a = 1.5235$, n_b=1 and $n_t = 0.95$. The coordinates of A and B are (0.14, 0.3961) and (0.86, 0.3961) respectively.

found that for the same n_t the bandwidth of the lower order bandgap is generally wider than that of the higher order bandgap. This is validated by calculating and plotting the bandwidth for different order bandgaps in the same diagram by using Eqn. (2.1) in Fig. 2.3. Since the modes of interest in the design lie close to $n_{eff} = 0.95$, $n_t = 0.95$ is used in Fig. 2.3. The maximum bandwidth for the 1st-order bandgap occurs when $\tau = 0.5$, which satisfies the QWC. In addition, for any given centre frequency of interest, the maximum bandwidth of the 1st-order bandgap is almost twice that of the 2nd-order bandgap, three times that of the 3rd-order bandgap, *etc*. For a given bandwidth, a higher order bandgap offers a wider range of possible values of τ. If $\tau = 0$ and $\tau = 1$ are excluded, which indicate that the thickness of one material in the photonic crystal is zero, it can be seen that ζth order bandgap has $\zeta - 1$ closing point(s) when τ sweeps from 0 to 1. Moreover, for both TE and TM bandgaps, the bandwidth of the ζth ($\zeta = 1,2,3$) order bandgap has ζ peaks for any certain value of n_t.

2.1.2 Representative cases

The points A and B in Fig. 2.3 have the same bandwidth, but their bandgap structure is very different, as shown in Fig. 2.4. In Fig. 2.4, the black region represents the bandpass region for TE/HE modes in which the modes are allowed to propagate through the cladding periodic structure and are not confined in the fibre. The remaining white region shows the bandstop region, defining the bandgap for TE/HE modes. Fig. 2.4 (a) and (b) represent the points A and B in Fig. 2.3, respectively. The upper and lower edge of the 1st-order bandgaps at $n_{eff} = n_t = 0.95$ for both of them are $f_h = 1.1143$ and $f_l = 0.7459$. Thus the midrange ratio bandwidth is $\Delta = 0.3961$ which is the same

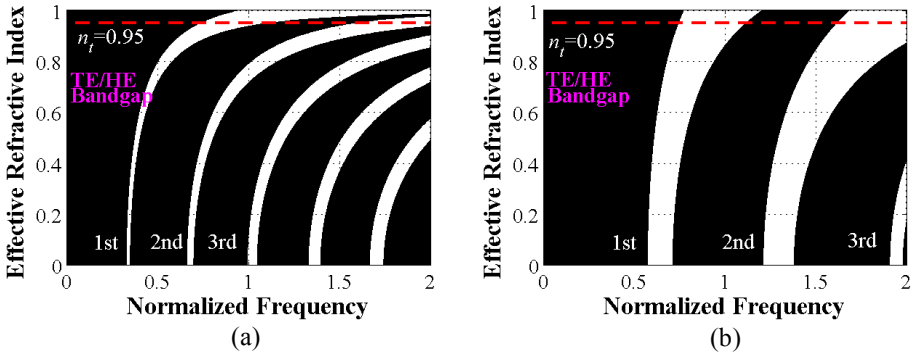

Fig. 2.4 TE/HE bandgap diagrams for the points A (a) and B (b) in Fig. 4. The x-axis is normalized to the frequency of interest $f_t(=c/\lambda_t)$. The red dashed line indicates the target effective refractive index of interest $n_t = 0.95$. The upper and lower edge of the 1st order bandgaps for both points A and B are $f_h = 1.1143$ and $f_l = 0.7459$ when $n_t = 0.95$. Thus, the midrange ratio bandwidth is $\Delta = 0.3961$. The black region represents the bandpass region for TE/HE modes.

as the value obtained in Fig. 2.3. Although the centre frequency of the 1st-order bandgaps at $n_t = 0.95$ shifts slightly from 1 to 0.93, it can then be tuned back by slightly changing the wavelength of interest λ_t in Eqns. (2.6) and (2.7) so that the target frequency can be achieved. When the effective refractive index n_{eff} is swept from 0 to 1 in Fig. 2.4, the 1st-order bandgap shape of Fig. 2.4 (point A) is narrower than that of Fig. 2.4 (b) (point B) when $n_{eff} < n_t$, but when $n_{eff} > n_t$, conversely, the bandgap width of the 1st-order bandgap in Fig. 2.4 (a) is wider than that in Fig. 2.4 (b). Furthermore, the 1st-order bandgap of Fig. 2.4 (a) spans several octaves in frequency, which is much wider than that of Fig. 2.4 (b). The different behaviours between the points A and B are important differences in the Bragg fibre in terms of manipulating the shape of the bandgap.

In practical terms, it is also needed to consider the thickness contrast between the cladding layers, as well as their absolute values. According to the GHWC, the thickness contrast between the claddings can be derived from the Eqns. (2.6) and (2.7):

$$\frac{b}{a} = \frac{n_{at}(1-\tau)}{n_{bt}\tau} \tag{2.8}$$

In accordance with Fig. 2.3 and Fig. 2.4, $n_t = 0.95$, $n_a = 1.5235$ and $n_b = 1$ are selected, thus $n_{at} = 1.1910$ and $n_{bt} = 0.3122$, and the thickness contrast becomes $b/a = 3.8143\times(1/\tau - 1)$ which has an inverse relationship with τ. As a is the thickness of the dielectric claddings and b is the thickness of the air claddings, τ is a factor which affects the porosity of the Bragg fibre. The value of τ for point A is smaller than that of point B, and hence the thickness

contrast of A is larger than that of B, and in return the porosity corresponding to A is higher than that of B. From Eqn. (2.8), the bandgap order number ζ does not affect the thickness contrast, but the absolute values of the cladding thicknesses have a direct relation with ζ. The absolute values of the cladding thicknesses are important parameters in fabrication since every fabrication technique has a limit of processing precision. Using the same parameters as in Fig. 2.4, the thicknesses of the dielectric and air cladding can be expressed respectively as $a = \zeta \frac{\tau}{2.382}\lambda_t$ and $\mathrm{b} = \zeta \frac{1-\tau}{0.6244}\lambda_t$, indicating that the thicknesses of the claddings are proportional to the bandgap order number ζ. Therefore, the thickness of the claddings can be manipulated by the bandgap order number to fit the processing precision of the available fabrication techniques, such as fibre drawing or extrusion.

2.1.3 The central gap points

The central gap points of bandgaps are interesting prominent points, and can be easily manipulated by the GHWC. In Fig. 2.3, the maximum point(s) of each order bandgap corresponds to their central gap point(s). In order to verify this argument, the stratified planar anti-resonant reflecting optical waveguide (SPARROW) model [122] is taken as a reference method to calculate the central gap points. For instance, the bandgap topologies of points C ($\tau = 0.25, \zeta = 2$) and D ($\tau = 0.5, \zeta = 3$) are shown in Fig. 2.5. For better illustration, $n_t = 0.8$ is chosen. In Fig. 2.5, the SPARROW model curves are overlaid upon the TE/HE bandgap diagram. The x-axis is normalized by the frequency of interest $f_t (= c/\lambda_t)$. From Fig. 2.5, the central gap point ($f/f_t, n_t$)=(1, 0.8) predicted by the GHWC is precisely consistent with the value given by the SPARROW model for both cases. This is true for every order of bandgap.

Summarily, one can manipulate the shape of the bandgap in Bragg fibre by using the GHWC, which can efficiently and flexibly manipulate any order of bandgap, while the QWC only predicts the central point of the 1st order bandgap. As discussed, the meaning of each variable in the GHWC is clear. After choosing the materials, for a given effective refractive index of interest n_t, any specific central frequency of ζ^{th} order bandgap can be archived by tuning λ_t, and its bandwidth is controlled by the porosity factor τ. This condition works with any combination of materials as long as $n_a > n_b \geq n_c \geq 1$, and it is not only functions well over the terahertz spectrum, but also in other frequency ranges.

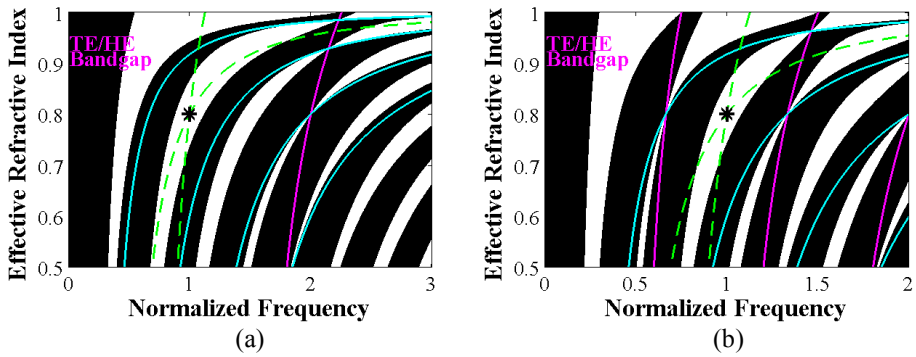

Fig. 2.5 SPARROW model curves overlaid upon the TE/HE bandgap. The cyan and magenta solid curves are the dispersion curves of the equivalent isolated cladding layers in the SPARROW model. For both (a) and (b), the intersections of the green dashed curves are the central gap points of the corresponding bandgaps given by the SPARROW, while the black circles are the central gap points predicted by the GHWC. All parameters are the same as that of Fig. 2.3 except $n_t = 0.8$. (a) $\tau = 0.25$, $\zeta = 2$. (b) $\tau = 0.5$, $\zeta = 3$.

2.2 Design of THz Bragg fibre

Both HE_{11} [92, 106, 123] and TE_{01} [114] have been chosen as the operating mode in Bragg fibres. The HE_{11} mode is the fundamental mode in Bragg fibres, which is desirable for single-mode operation, and its linear polarization makes it easier to couple with other devices. However, in practical designs, support bridges are required to maintain the air gap between the cladding layers. In Bragg fibres using the HE_{11} mode as their operating modes, the support bridges cause significant coupling between the core mode and the surface states, including cladding modes and other modes which are mainly distributed around the bridges. Subsequently, this effect narrows the effective transmission band and increases the propagation loss significantly [92, 106, 123].

The negative influence of the support bridges on the performance can be greatly reduced by employing the TE_{01} mode as the operating mode, as detailed in section 2.2.5. The TE_{01} mode is the first mode with zero azimuthal mode number, and it has a null point in the electric field near the core-cladding interface which prevents the field penetrating into the cladding; this minimizes the negative influence of the support bridges and surface roughness [114], resulting in extremely low propagation loss. In addition, typical single-TE_{01}-mode Bragg fibre requires a large core, with many cladding layer periods and a long transmission distance to filter out the unwanted modes [114]. In this chapter, by introducing a new approach using the modal-filtering effect, a low-loss single-TE_{01}-mode Bragg fibre can be

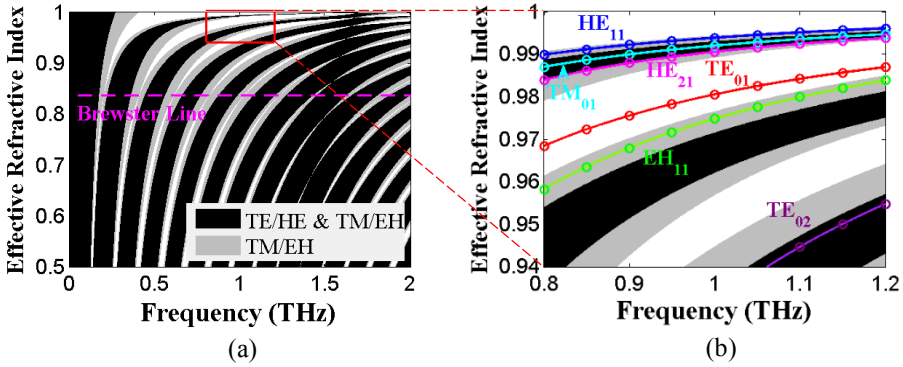

Fig. 2.6 Bandgap and dispersion curves of the target Bragg fibre. (a) Global view of the bandgap. The black (black and grey) region represents the bandpass region for TE/HE (TM/EH) modes. The dashed magenta line is the Brewster line. The red box indicates the region of interest and is detailed in (b). (b) The bandgap and dispersion curves. The blue, cyan, magenta, red, green, and purple solid lines are the theoretical dispersion curves of HE_{11}, TM_{01}, HE_{21}, TE_{01}, EH_{11}, and TE_{02} modes, respectively, calculated using the transfer matrix method, while the circles with same colours are their corresponding simulation results obtained from COMSOL.

achieved with a small air core and only 4 cladding layer periods. Besides, the TE_{01} mode has the additional benefit of an immunity to polarisation-mode dispersion from fibre birefringence thanks to it being cylindrically symmetrical and non-degenerate [114]. Moreover, efficient coupling of the TE_{01} mode in a small-core THz Bragg fibre has been reported [124], but the propagation loss of the designed single-TE_{01}-mode Bragg fibre in [124] is still as high as 43.4 dB/m.

2.2.1 Bandgap and dispersion curves

Based on the GHWC, the material and geometry properties of the target THz Bragg fibre are listed in Table 2.2. Here, N is the number of photonic crystal periods. In order to locate the minimum propagation loss point of the TE_{01} mode at the centre of the frequency of interest (1 THz), λ_t should be tuned carefully around 0.3 mm in practice. By using Eqn. (2.1) and parameters

Table 2.2 Material and geometric properties of the THz Bragg fibre

Dielectric properties			Geometry parameters				Tentative indexes			
n_a*	n_b	n_c	a [μm]	b [mm]	r_c [μm]	N	τ	ζ	n_t	λ_t [μm]
$1.5235+i\kappa_a$	1	1	77.5	1.154	917.1	4	0.5	1	0.997	357.29

* The frequency dependent complex refractive index of n_a (TOPAS) is obtained from the reference [53]. The extinction coefficient of TOPAS κ_a is calculated based on its absorption coefficient $\varkappa_a$ (dB/cm) $= -0.13 + 0.63(f/1\times10^{12}) + (f/1\times10^{12})^2$.

listed in Table 2.2, the bandgap diagram of the designed THz Bragg fibre is shown in Fig. 2.6 (a). Here, the bandgap diagram of TE/HE modes and TM/EH modes are combined in a single diagram. The black (black and grey) regions represent the bandpass region for TE/HE (TM/EH) modes, where the modes are allowed to propagate through the periodic cladding layers and are not confined in the Bragg fibre. On the contrary, the remaining region for each kind of bandgap diagram indicates the bandstop region or so-called bandgap in which the modes are forbidden to pass through the radial photonic crystal structure, and are subsequently confined in the fibre. The horizontal dashed black line 1is the Brewster line at which the TM/EH bandgaps are always closed completely, and the TE/EH modes have no reflection at the n_a/n_b interface [87]. The solid red box designates the parameter range of the designed THz Bragg fibre and is detailed in Fig. 2.6 (b).

In Fig. 2.6 (b), the transfer matrix method [125, Appendix A] and finite-element method (using COMSOL frequency domain solver) have both been used to independently calculate the dispersion curves. For simplicity, only the dispersion curves of the first six representative modes are plotted, i.e. HE_{11}, TM_{01}, HE_{21}, TE_{01}, EH_{11} and TE_{02}. TE_{01} is the desired fundamental mode, while HE_{11}, TM_{01}, HE_{21}, EH_{11}, and TE_{02} represent the modes competing with TE_{01}. Among these competing modes, HE_{11} and HE_{21} are the two lowest-order TE or TE-like (HE) modes, while TM_{01} and EH_{11} are the two lowest order TM or TM-like (EH) modes, and TE_{02} is the second mode with zero azimuthal mode number and a similar null point in the electric field near the core-cladding interface. The relative positions of all these modes to the bandgaps affect their propagation loss significantly. These positions are specially designed to enlarge the loss discrimination between the desired TE_{01} mode and its competing modes, which will be detailed in section 2.2.4.

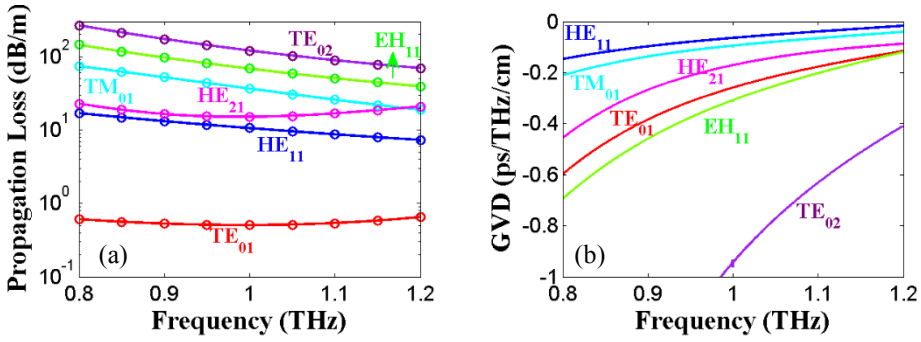

Fig. 2.7 (a) Propagation loss and (b) group velocity dispersion of the Bragg fibre. Solid lines are theoretical results and discrete circles are corresponding simulation results.

It is noted that the outermost cladding layer of the Bragg fibre is treated as an absorption layer and there is no signal reflection from the outside. This is achievable in practice by using a thick shielding layer. Hence, in the transfer matrix method, an absorption boundary condition has been used at the interface of the outermost period and the outermost shielding layer as suggested in [125], while in the finite-element method, a perfect-matched layer has been applied.

2.2.2 Propagation loss, GVD, and mode structure

The propagation loss and GVD of the various modes are shown in Fig. 2.7. In Fig. 2.7 (a), the propagation loss of the desired TE_{01} mode is less than 0.6 dB/m, which is the lowest loss mode across the frequency range of interest (from 0.8 THz to 1.2 THz), while the propagation loss of the main competing mode HE_{11} is more than 11 times greater than that of TE_{01} at the closest frequency points (1.2 THz). It should be noted that the proposed Bragg fibre is a small-core fibre using only 4 cladding layer periods, and that its loss discrimination is even larger than that of a large core fibre with 8 cladding layer periods [114]. The larger loss discrimination is attributed to the modal-filtering effect. Moreover, Fig. 2.7 (b) shows that the GVD of the desired TE_{01} mode is less than -0.6 ps/THz/cm. In Fig. 2.6 and Fig. 2.7, the numerical simulation results from COMSOL show an excellent consistency with the analytical predictions calculated by the transfer matrix method, supporting

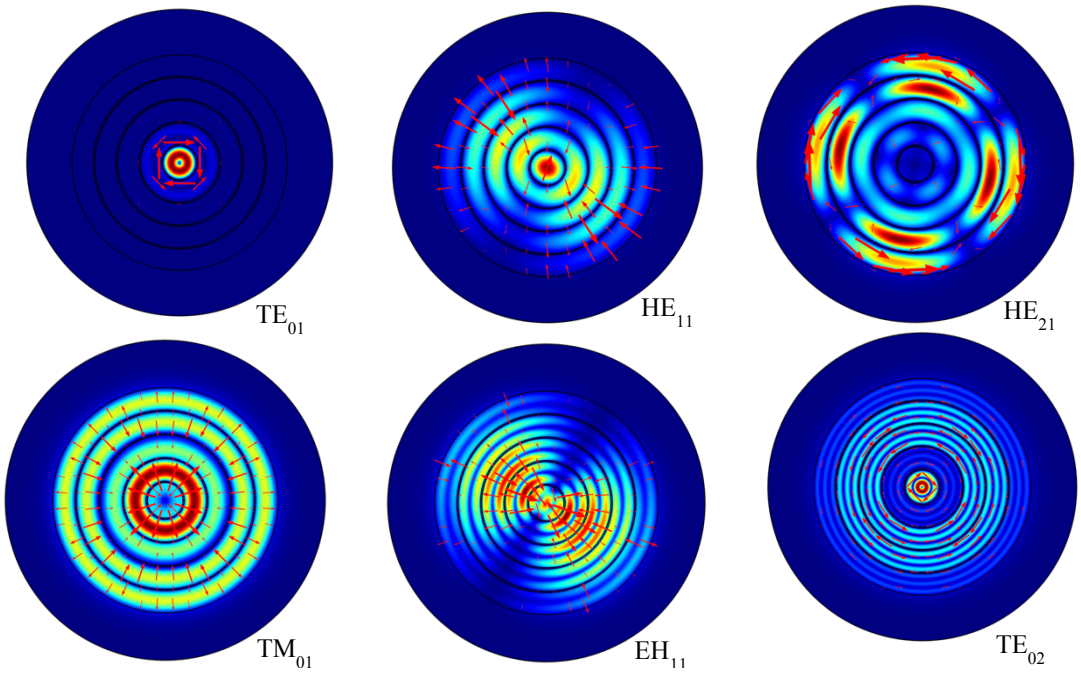

Fig. 2.8 Normalized electrical field of the six representative modes at 1 THz. Relevant material and geometry parameters are listed in table 2. The field decreases from red to blue.

the validity and the accuracy of both methods.

The mode patterns at 1 THz are presented in Fig. 2.8. It can be seen that the electric field of the desired TE_{01} mode is essentially confined within the lossless air core, while that of the competing modes are leaky, thus experiencing a high signal attenuation introduced by the bulk cladding materials. Subsequently, the TE_{01} mode has significantly less propagation loss from the surface roughness and the support bridges compared to the other competing modes.

2.2.3 Impact of the uncertainty of the refractive index of TOPAS

From 0.2-1.5 THz, the real part of the refractive index of TOPAS in [53] varies in the range of 1.5235±0.0005, while that in [41] varies in the range of 1.5258±0.0002. it is noted that both measurements were conducted by the same group of researchers across different years. The differences indicate that the real part of the refractive index of TOPAS may thus vary from 1.523 (lower limit in [53]) to 1.526 (upper limit in [41]). Therefore, it is of interest to investigate the impact of this uncertainty of the refractive index of TOPAS on the dispersion curves and propagation losses in the design. The results from this investigation are shown in Fig. 2.9. Here, the geometry parameters are the same as those listed in Table 2.2. As for the absorption coefficient of TOPAS, the measurement results in [53] which is slightly greater than that in [41] are used, standing for the case of the highest propagation loss in the design owing to the material absorption within the available parameter range of the absorption coefficient of TOPAS. For simplicity, only the dispersion curves and the propagation losses of the two lowest-loss modes are considered in Fig. 2.9. From Fig. 2.9 (a) and (b), it can be seen, respectively, that the impact of the uncertainty of the refractive index of TOPAS ranging from 1.523 to 1.526 on the dispersion curves and propagation losses of the TE_{01} and HE_{11} modes is negligible.

2.2.4 Modal-filtering effect

That the propagation loss of the desired mode should be smaller than that of the other unwanted competing modes is important for the transmission properties of Bragg fibres. Even if several modes are excited at the input, only the desired mode will remain in the Bragg fibre after a certain distance [126] while the other competing modes are heavily attenuated. This strong mode selectivity introduced by the loss discrimination creates a modal-filtering effect and results in an effectively single-mode operation in the Bragg fibre.

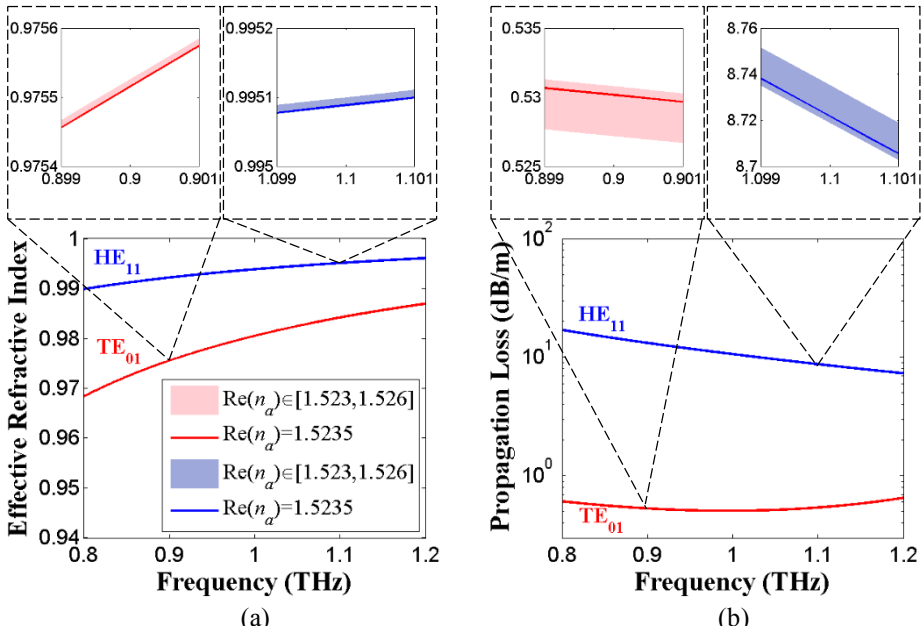

(a) (b)

Fig. 2.9 The impact of the uncertainty of the refractive index of TOPAS on the dispersion curves (a) and propagation losses (b) of TE_{01} and HE_{11} modes. The solid red and blue lines corresponds to $\mathrm{Re}(n_a) = 1.5235$. The light red and blue regions correspond to $\mathrm{Re}(n_a) \in [1.523, 1.526]$. (a) and (b) share the same legend.

There are many factors that contribute to the modal-filtering effect, including the Brewster phenomenon, the confinement loss of each mode, the number of cladding layer periods, and the support bridges. In Fig. 2.2, for any combination of cladding layer thicknesses (any value of τ), the TM/EH bandgap always closes up entirely at the Brewster angle, owing to the Brewster phenomenon and ensuring that the bandgap of TM/EH modes is always narrower than that of TE/HE modes, especially near the Brewster line, as exemplified in Fig. 2.6. This behaviour of the TM/EH bandgap increases the possibility that the TM/EH modes lie outside the bandgap and become lossy. In addition, the closer the dispersion curve of a guiding mode lies to the edge of the bandgap, the more field penetrates into the claddings, and the higher the confinement loss of it is. Thus, even if the dispersion curves of the TM/EH modes lie inside the bandgap, they are closer to the edge of the bandgap than that of the TE/HE modes, which leads to higher confinement loss. Therefore, the Brewster phenomenon increases the loss of TM/EH modes and increases their loss discrimination with the desired mode.

The confinement loss is defined as the loss due to the scattering of the multilayer claddings only, excluding the material absorption, and hence only the real parts of the refractive indexes of materials have been taken into account in calculating the confinement loss. This should be differentiated

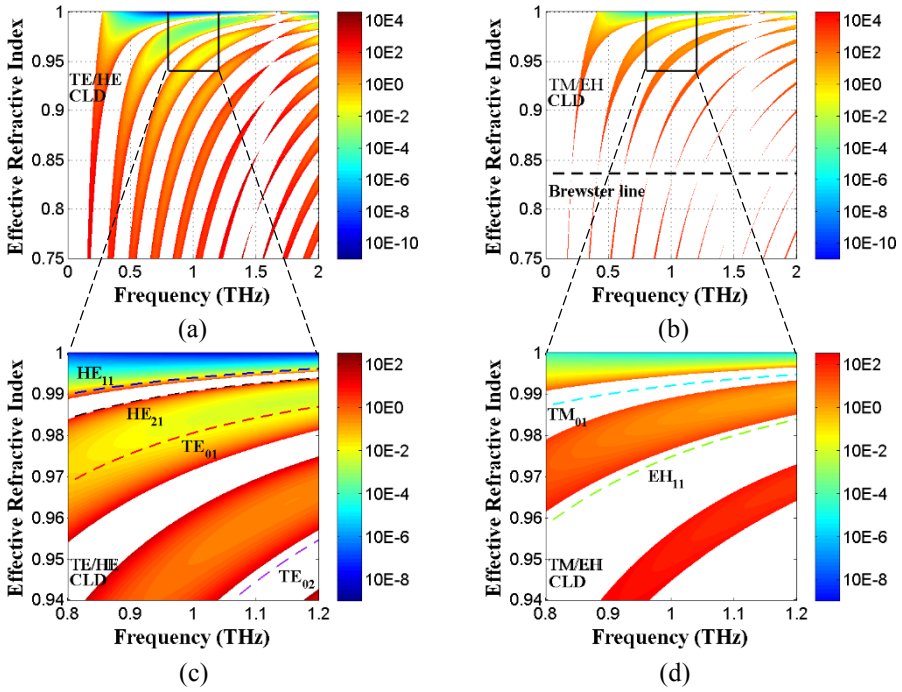

Fig. 2.10 Confinement loss diagram in photonic bandgap. The colour map represents the value of confinement losses. The unit is dB/m. The details in the black boxes in (a) and (b) is detailed in (c) and (d), respectively. The dashed blue, black, red, purple, green and cyan lines are the dispersion curves of HE_{11}, HE_{21}, TE_{01}, TE_{02}, TM_{01}, and EH_{11}, respectively.

from the propagation loss which considers the material absorption as well. Owing to the finite number of the cladding layer periods, the guiding modes in the bandstop (or bandgap) region are intrinsically leaky since the confinement is not perfect. This confinement loss, however, decreases exponentially with an increase in the number of the cladding layer periods. It is noted that this leaky mechanism should not be confused with the leakage of modes in the bandpass region which is determined by Bloch's theorem [118].

To characterise the confinement loss of the designed Bragg fibre, the confinement loss diagram (CLD) [127] and the photonic bandgap are shown together in Fig. 2.10. Here, all the parameters of the geometry and the materials are listed in Table 2.2, except that only the real part of the complex refractive indexes is used, since only consider the scattering loss is considered. The CLD, which presents the confinement loss of the Bragg fibre based on the properties of the geometry and the materials, is independent of any mode. Thus, it is useful to provide a global view of the confinement loss of any Bragg fibre. In addition, as only the region inside the bandgap where the modes can be confined in the Bragg fibre supports the guided modes, so the CLD is overlaid with the photonic bandgap diagram. In

other words, the confinement loss inside the bandgap region is plotted. This is a new feature compared with the original confinement loss diagram [127], which highlights the differences of the confinement loss between the modes of interest. The colour map in Fig. 2.10 represents the value of the confinement loss in dB/m. Fig. 2.10 (a) is the CLD corresponding to TE and HE modes, while Fig. 2.10 (b) corresponds to TM and EH modes. From Fig. 2.10 (a) and (b), due to the presence of the Brewster phenomenon for TM and EH modes, the bandgaps of the TM/EH modes are always narrower than that of the TE/HE modes for the same order bandgaps, resulting in higher confinement loss of TM and EH modes compared to that of the TE/HE modes. For all polarisations, the confinement loss in the central region of any order bandgap is always lower than that in the fringe region of the same order bandgap. In addition, for any given frequency, the confinement loss in the central region of the lower order bandgap is less than that of higher order bandgap, while the confinement loss in the fringe region for any order of bandgap is in a similar range. Therefore, it is possible that the confinement loss in the central region of a higher order bandgap is in fact less than that in the fringe region of a lower order bandgap.

The confinement loss diagrams, along with the analytical dispersion curves of TE/HE modes and TM/EH modes are plotted in Fig. 2.10 (c) and (d). As was discussed in section 2.2.1, the relative positions of the six selected modes to the bandgap are significant as they affects the confinement losses of the corresponding modes. It is possible that the confinement loss in the central region of the higher order bandgap is less than that in the fringe region of lower order bandgap. Therefore, based on the GHWC, the bandgap is tailored to place the TE_{01} mode close to the central region of the

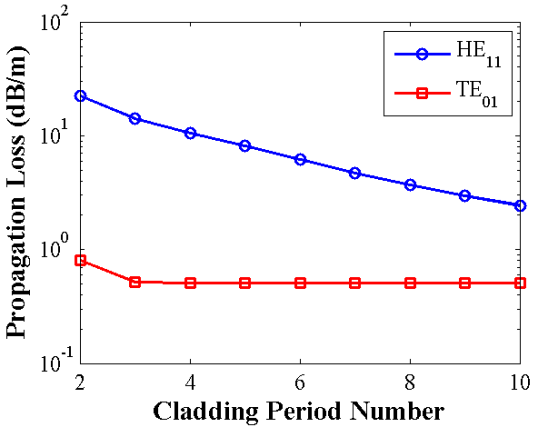

Fig. 2.11 The dependence of the propagation loss at 1 THz of the desired TE_{01} mode and the second lowest loss HE_{11} mode on the number of cladding periods.

2^{nd}-order bandgap and meanwhile let the HE_{11} mode be at the edge of 1^{st}-order bandgap. the TE_{02} mode, which has a similar ring field pattern to the TE_{01} mode and can potentially compete mode of TE_{01} mode, is restricted to be located outside the bandgap to reduce its impact. In Fig. 2.10 (d), both the TM_{01} and EH_{11} mode have been designed to be located outside the bandgap making them very lossy. Within the frequency range of interest, from 0.8 THz to 1.2 THz, compared to the aforementioned six representative modes, other higher order modes are located either in the higher order bandgaps or outside any bandgap resulting in higher confinement loss and weak mode competition. Therefore, the designed Bragg fibre has strong mode selectivity owing to the presence of the photonic bandgap.

According to [128], the propagation loss of the guiding modes in the bandgap region first decreases exponentially with increase in the number of cladding layer periods, following the same exponentially decreasing trend as the confinement loss, and then converges to a constant value due to the limit of the material absorption. Fig. 2.11 illustrates the dependence of the propagation losses at 1 THz of the desired TE_{01} mode and its main competing mode HE_{11} on the number of the cladding layer periods. From Fig. 2.11, when the number of the cladding layer periods, N>3, the loss of the TE_{01} mode shows almost no change, while the loss of the HE_{11} mode is still decreasing. As the introduction of support bridges breaks the periodicity of the photonic crystal structure and increases the propagation loss, the number of cladding layer periods is limited to 4 to ensure low loss of the TE_{01} mode. In other words, four periods are sufficient to achieve tight confinement of the desired TE_{01} mode and is a trade-off for the Bragg fibre, because when N>4, the loss discrimination between the desired modes and its competing modes reduces, and the increase of the number of periods does little to reduce the loss of the desired mode.

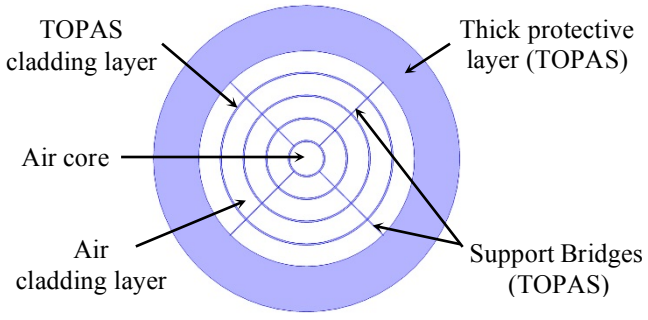

Fig. 2.12 Schematic of the practical Bragg fibre with support bridges of width 15 μm.

2.2.5 Impact of the support bridges

The impact of the support bridges on the spectral behaviour of the guided modes is significant. There are many choices in terms of the deployment of the support bridges in a Bragg fibre. Support bridges without symmetry in any two orthogonal directions cause polarization-mode dispersion. At the same time, it is preferable to have thin and fewer support bridges so as to minimize their negative impact. However, a trade-off has to be made between the thickness and the layout of the support bridges and the fabrication convenience. Accordingly, the layout of the proposed fibre with support bridges is shown in Fig. 2.12. Thanks to the small core, the need for support bridges is significantly reduced compared to designs with a larger core [106]. Here, the width of the support bridges is set to 15 μm, which has been optimized by sweeping the width from 5 μm to 50 μm to reduce the propagation losses of the desired TE_{01} mode over the frequency range from 0.85 THz to 1.15 THz.

Fig. 2.13 (a) shows the propagation loss of the desired TE_{01} mode support bridges. The propagation loss of the TE_{01} mode in the practical Bragg fibre (solid blue line) follows the trend of the ideal Bragg fibre (dotted black line). The deviations between them and some narrow peaks in the practical case are attributed to the presence of the support bridges which break the periodicity of the photonic crystal structure and introduces strong coupling between the TE_{01} mode and the surface states [92, 113, 129]. The mode structure at several representative frequencies is shown in Fig. 2.13 (c) – (i), while Fig. 2.13 (b) shows the mode structure of the desired mode without support bridges. It can be clearly seen that compared to the ideal case without bridges, slightly more of the desired field from the TE_{01} mode in the fibre penetrates into the cladding layers, resulting in an increased loss. The coupling between the core mode with the surface states increases the propagation loss significantly, which also decreases the effective bandwidth of the Bragg fibre and so is undesirable. Nonetheless, the propagation loss of the designed Bragg fibre with support bridges is still less than 1.2 dB/m from 0.85 THz to 1.15 THz with a minimum of 0.5953 dB/m at 0.98 THz.

Thanks to the special mode structure of the TE_{01} mode with a null point in electric field near the interface between the core and the cladding, the support bridges in the design only slightly increase the propagation loss of the desired TE_{01} mode, while causing coupling between the core mode and the surface states. In addition, compared to the larger core scheme in [114], the utilization of a second order bandgap to confine the desired TE_{01} mode

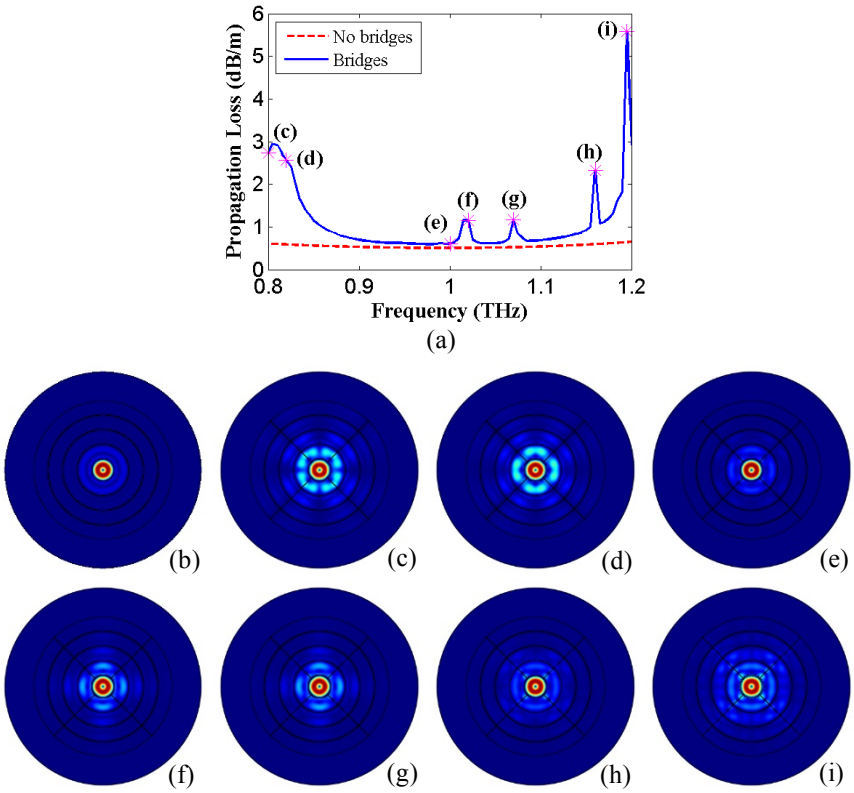

Fig. 2.13 (a) Propagation loss of TE_{01} mode. (b) is the normalized electrical field of TE_{01} mode at 1THz in ideal Bragg fibre without supportive bridges. (c) – (i) are the normalized electrical field of TE_{01} at 0.8 THz, 0.82 THz, 1 THz, 1.02 THz, 1.07 THz, 1.16 THz, and 1.195 THz, respectively.

in the design greatly reduces the diameter of the core. Subsequently, it reduces the size of the fibre, reducing the need for and negative impact from support bridges, and hence should be beneficial to fabrication.

2.3 Concluding remarks

This chapter presents a detailed analytical and numerical study of a tightly confined single-TE_{01}-mode small-air-core terahertz Bragg fibre which exhibits both low loss and low dispersion. Firstly, a generalized half-wavelength condition (GHWC) is proposed, which relates the photonic bandgap with the material and geometry properties, promoting the manipulation of the photonic bandgap in the Bragg fibre effectively. The properties of different order photonic bandgaps in the Bragg fibre have been investigated.

Secondly, the modal-filtering effect which contributes to increased discrimination by loss between the desired fundamental modes and other high order unwanted competing modes has been investigated, which allows

the fibre to operate in an effectively single-mode fashion. The factors contributing to the modal-filtering effect have also been discussed.

Thirdly, the use of the modal-filtering effect is proposed in a novel way. The bandgap is tailored by using the generalized half-wavelength condition to let the desired TE_{01} mode be located near the central region of the second order bandgap, while maintaining loss discrimination between the desired TE_{01} mode and other unwanted competing modes. This reduces the required diameter of the core and hence reduces the size of the fibre. It also reduces the need for support bridges, aiding fabrication.

Finally, based on the analysis, the design of a tightly confined single-TE_{01}-mode small-air-core Bragg fibre with propagation loss and GVD less than 1.2 dB/m and -0.6 ps/THz/cm respectively over a frequency range from 0.85 THz to 1.15 THz is proposed, presenting significant potential improvements compared to existing single-mode THz Bragg fibres. Having now determined an optimised structure for a THz Bragg fibre, the work is focusing on a number of fabrication methods.

Chapter 3
3D-printed Sub-THz Bragg Fibre

In this chapter, the design, fabrication, and measured performance of an all-dielectric asymptotically single-mode low-loss THz Bragg fibre, fabricated by digital light processing rapid prototyping, are proposed. The material structure of the proposed Bragg fibre, which uses a single dielectric, reduces the complexity of fabrication, while also making the fibre suitable for sensing applications in acidic or high magnetic field environment, which can be problematic for metallized waveguides [58, 15, 35]. It is also demonstrated that 3D printing using digital light processing techniques can be used to conveniently and cost-effectively fabricate high-porosity air-core Bragg fibres, which is challenging for other fabrication techniques. The Bragg fibre is designed to have large loss discrimination between the desired HE_{11} mode and other competing modes, so creating a modal-filtering effect while exhibiting strong mode selectivity. Based on the EM simulations, which use measured characteristics for our materials, and the actual geometric parameters of the fabricated Bragg fibre prototype, an asymptotically single-HE_{11}-mode operation was verified, ensuring the low-loss transmission of THz waves since only the desired HE_{11} mode can propagate in the low loss air core. Most importantly, although the loss tangent of the 3D printing material used in this work (EnvisionTEC HTM140) is much higher than other low-loss materials commonly used in the reported THz microstructured fibres, a very low loss asymptotically single-mode Bragg fibre was nonetheless successfully demonstrated.

3.1 3D fabrication of the THz waveguide

Fig. 3.1 (a) and (b) show the geometry and the refractive index profile of the proposed Bragg fibre. It comprises an air core ($n_c = 1$), surrounded by periodic concentric dielectric layers of alternating high (n_a) and low (n_b) refractive index materials, the thickness of which are a and b respectively, while r_c is the core radius and $\Lambda = a + b$ is the period of the radial photonic crystal. The outermost layer is a thick protective layer which will absorb any residual EM waves and isolate the fibre from external perturbations. Support bridges are introduced to mechanically maintain the air gaps between dielectric layers. The thicknesses of the outermost layer and the support bridges are represented by t and w, repectively.

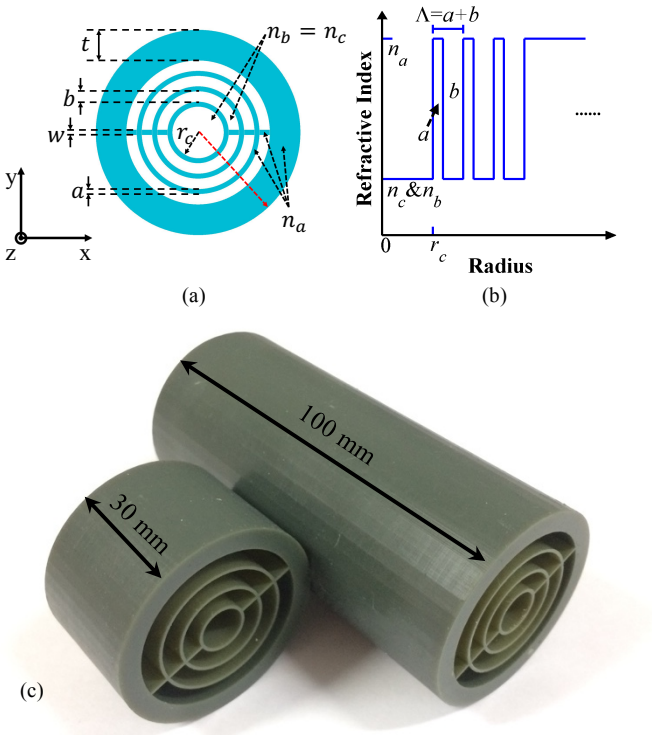

Fig. 3.1 The proposed Bragg fiber structure: (a) A cross-sectional diagram showing the key design parameters; (b) The radial refractive index profile, taken along the red dashed arrow in (a) starting from the center and going into the edge; (c) A photograph showing the samples with lengths 30 mm and 100 mm. The designed and actual dimensions are listed in Table 3.1.

In this chapter, EnvisionTEC HTM140 photopolymer was the material chosen owing to its high refractive index to provide cladding layers, the outermost protective layer, and the support bridges, while air gaps provided the low refractive index cladding layers ($n_b = n_c = 1$). Fig. 3.2 shows the complex refractive index of HTM140 over the frequency range from 0.24 to 0.3 THz, measured using the Keysight free-space material characterization

Table 3.1 The Designed and Measured Geometric Parameters

Parameters	Design (mm)	Measurement (mm)
a	0.652	0.667 ± 0.005
b	3.888	3.877 ± 0.004
r_c	4.742	4.681 ± 0.004
t	4.6	4.544 ± 0.011
w	0.64	0.652 ± 0.009

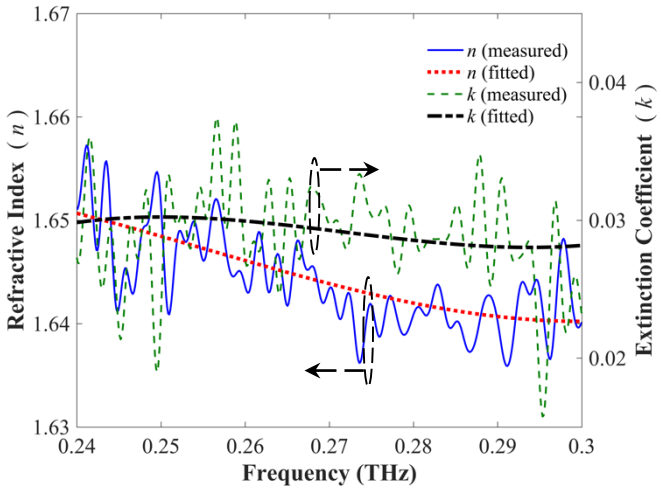

Fig. 3.2 The complex refractive index of HTM140. The solid blue curve and the dashed green curve represent the refractive index and extinction coefficient of HTM140, respectively, measured using the Keysight commercial free space material characterization platform. The dotted red curve and the dash-dotted black curve are the 3rd-order polynomial regression fitted curves based on the solid blue curve and the dashed green curve, respectively. The root mean squared errors between the 3rd-order fitted data and the measurement results for the refractive index and the extinction coefficient are 0.0026 and 0.002, respectively.

platform with a vector network analyser (VNA) and frequency extenders, described in detail in section 3.3. The fast ripples in the measurement curves of the complex refractive index of HTM140 are due to residual VNA calibration errors. Two third-order polynomial curves were fitted to the real and imaginary part of the complex refractive index of HTM140, respectively. Compared to other well-known low-loss THz polymers [10], such as TOPAS, Zeonex, HDPE, and PTFE, the material attenuation of HTM140 is much higher, which is a common limitation of most commercial available photopolymers in 3D printing applications at the time of writing. However, since the EM field in the Bragg fibre is tightly confined and mainly propagates inside the low-loss air core, only a small portion of the EM field is distributed in the periodic cladding material, and thereby the deleterious impact of the relatively high material attenuation of HTM140 is mitigated by the air-core Bragg fibre design.

The geometry of the THz air-core Bragg fibre is listed in Table 3.1. The design principle of the proposed Bragg fibre is based on the previous theoretical work [130], which is briefly summarized as follows:

1. As n_a, n_b and n_c are given, the photonic bandgap of the fiber is determined by a and b. Based on the generalized half-wavelength condition presented in the previous theoretical work [130], the values of

a and b are chosen to provide a wide photonic bandgap cantered around 0.27 THz, which covers the frequency range of interest.

2. Like the classic hollow cylindrical metallic waveguide, the dispersion curves of supported modes in the Bragg fibre are mainly determined by the core radius r_c. Based on the analytical analysis using the transfer-matrix method [130], the value of r_c is carefully chosen to ensure low loss propagation of the desired fundamental HE_{11} mode, as well as a large loss discrimination between the desired mode and its competing modes.
3. Both t and w play a relatively insignificant role in the performance of the proposed Bragg fiber. The outermost layer is designed to be an absorbing layer, so $t > a + b$ can provide good attenuation of signals considering the material as HTM140. The support bridges are perpendicular to the polarization of the HE_{11} mode, and have negligible impact on the loss of the fibre, which will be discussed here in section 3.2.3.

Samples with two different lengths (30 mm and 100 mm, as shown in Fig. 3.1 (c)) were fabricated with the EnvisionTEC Perfactory 3 mini multi-lens 3D printer that uses digital light processing (DLP) rapid prototyping technology. The DLP 3D printer has a fabrication tolerance of 21 μm in the horizontal plane. It is found that a minimum dielectric thickness of ~400 μm was needed to achieve good fabrication quality. In order to satisfy this condition, the second-order photonic bandgap is chosen as the operating band for the desired fundamental HE_{11} mode, which allows the thickness of the polymer layer to be increased, although it reduces the operating bandwidth [130]. As shown in Table 3.1, the fabricated fibre dimensions are in good agreement with the design, within the expected tolerance of the 3D printer's capability.

3.2 Theoretical analysis and simulation

3.2.1 Analytical analysis and eigenmode simulation of the ideal Bragg fibre without support bridges

To simplify the complexity of optimizing the design, a Bragg fibre without any support bridges was first investigated, while the impact of the support bridges on the Bragg fibre performance will be discussed in later sections. According to Bloch's theorem in cylindrical coordinates [118], the bandgap diagram of the measured Bragg fibre, with the geometric parameters listed in Table 3.1, is as shown in Fig. 3.3 (a). For convenience, the mean value of the complex refractive index of HTM140 over the frequency from 0.24 to 0.3 THz, $n_a = 1.644 + 0.0293i$, was used in the calculation of the bandgap since the slight change over the frequency range of interest has negligible effect on the bandgap shape, verified using the previous theoretical analysis [130].

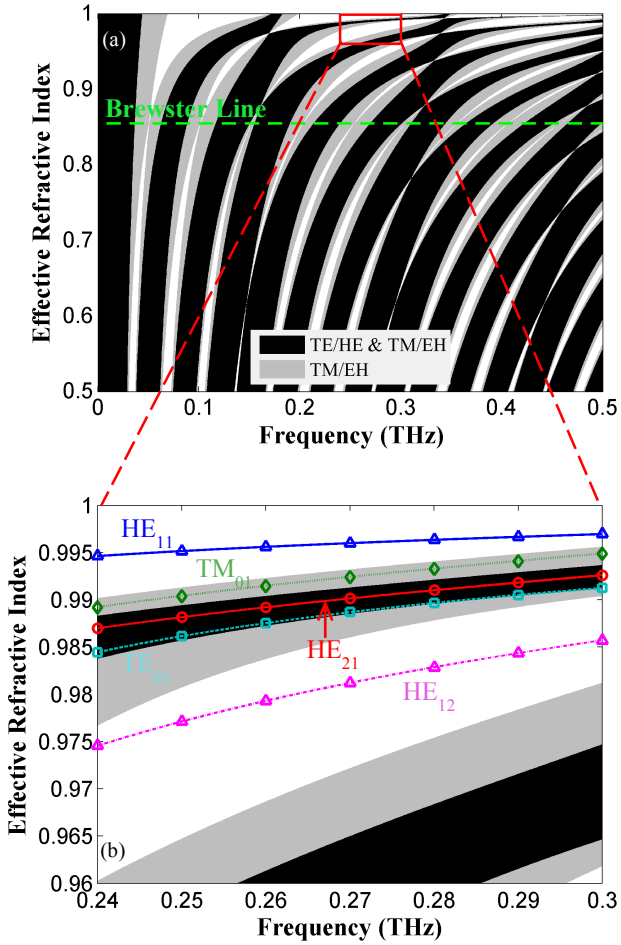

Fig. 3.3 Bandgap and dispersion curves of the ideal Bragg fibre. (a) Global view of the bandgap behaviour. The black regions represent the bandpass region for TE/HE modes while the black plus grey combined regions are for the TM/EH modes. The dashed green line is the Brewster line. The red box designates the operating parameter range of interest for the designed THz Bragg fibre and is expanded in (b). (b) The bandgap and dispersion curves. The blue solid line, green dotted line, red solid line, cyan dashed line, and magenta dash-dotted line are the analytical dispersion curves for the HE11, TM01, HE21, TE01, and HE12 modes, respectively, calculated using the transfer matrix method. The corresponding coloured markers are simulation results obtained from COMSOL.

However, all other analytical results and numerical simulations use the measured and fitted frequency-dependent complex refractive index of HTM140. The black regions represent the bandpass region for TE/HE modes, where the wave can propagate through the periodic cladding layers and is not confined in the fibre. The combined black plus grey regions show the bandpass region for the TM/EH modes. In contrast, the white and grey combined areas indicate the bandstop regions, or electromagnetic bandgaps, for the TE/HE modes: in this case, the wave cannot pass through

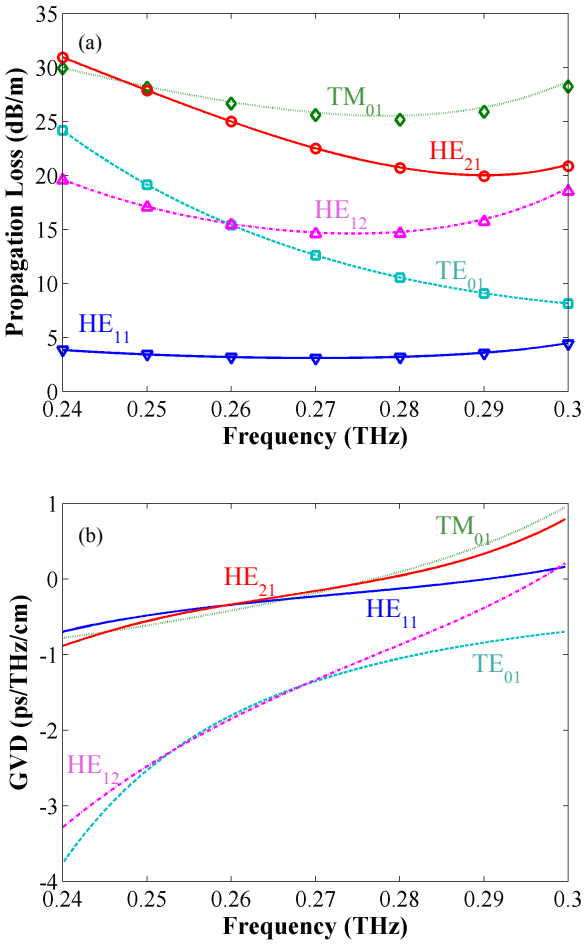

Fig. 3.4 (a) Propagation loss and (b) group velocity dispersion of the ideal Bragg fibre for the modes indicated in Fig. 3.3.

the radial photonic crystal structure, and is therefore confined within the fibre. The white areas show the regions where the TM/EH modes are confined within the fibre.

The highlighted region of Fig. 3.3 (a), expanded in Fig. 3.3 (b), designates the operating parameter range of interest for the designed THz Bragg fibre. In (b), the dispersion curves of the desired fundamental HE_{11} mode and other representative competing modes of the Bragg fibre, calculated by the transfer matrix method [125, Appendix A] and simulated by COMSOL frequency domain solver, are overlaid onto the bandgap diagram. Here, both in the theoretical analysis and simulation, the outermost cladding layer was set to be an absorbing layer with no reflected wave from the outside. Such an arrangement is achievable in practice by using a thick and lossy shielding layer. As mentioned at the end of section 3.1, the second-order bandgap was chosen as the operating band for the desired HE_{11} mode to overcome the fabrication challenges. According to the previous published work [130], the propagation losses of all modes in a Bragg fibre, including the five

selected representative modes, are sensitive to, and indeed determined by, their relative positions to the bandgaps. The proposed Bragg fibre is thereby designed to exhibit large propagation loss discrimination between the desired HE_{11} mode and other competing modes over the frequency range of interest, creating a modal-filtering effect, as shown in Fig. 3.4 (a), to obtain signal propagation with only the desired HE_{11} mode. Of course, at discontinuites and transitions the other modes may be excited, but the same is true of many well-developed waveguiding structures [131], and dealing with this issue will require further studies of specific cases.

Fig. 3.4 (a) shows that the desired HE_{11} mode is the lowest loss propagation mode across the frequency range from 0.24 to 0.3 THz, and that the propagation loss of the main competing mode HE_{12} is at least ~4.3 times greater in dB/m than that of the HE_{11} mode. The propagation loss discrimination between HE_{11} and HE_{12} modes at the centre of the band is greater than that at the edge of the band; at 0.27 THz, the propagation loss of the HE_{11} mode is 3.085 dB/m, while the propagation loss of HE_{12} is 14.7 dB/m. Note that, owing to the significant difference in polarization between HE_{11} and TE_{01}, there is barely any transfer from HE_{11} to TE_{01}. Therefore, TE_{01} is not the main competing mode of HE_{11}, although it is the second

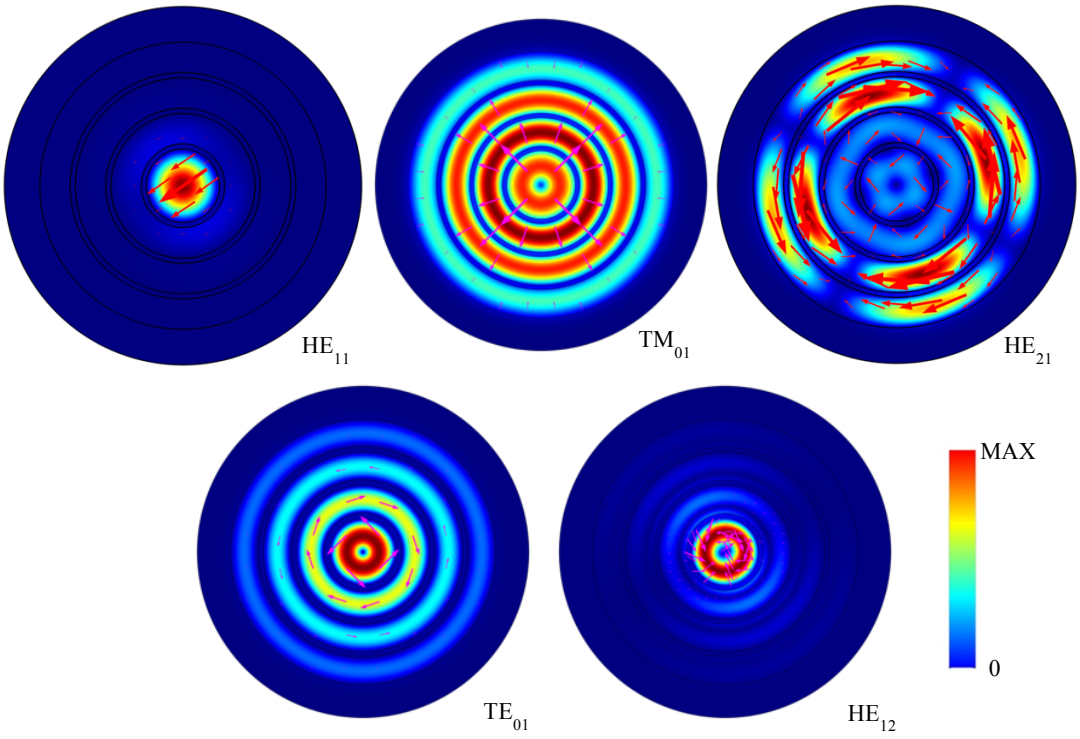

Fig. 3.5 Normalized electric field of the five selected representative modes at 0.27 THz. The field linearly decreases from red to blue. The magenta arrows in TM_{01}, TE_{01} and HE_{12} indicate the directions of the electric field.

lowest loss mode at some frequencies. In addition, Fig. 3.4 (b) shows that the desired HE_{11} mode exhibits low group velocity dispersion, with less than -0.56 ps/THz/cm between 0.246 to 0.276 THz. In Fig. 3.3 and Fig. 3.4, the consistency seen between the analytical theoretical analysis and the numerical COMSOL simulations validates the accuracy of both methods.

The normalized mode patterns of five selected representative modes are presented in Fig. 3.5. It can be seen that the electric field of the desired HE_{11} mode is well-confined within the low loss air core, while the mode patterns of the competing modes spread into the lossy cladding region, thus experiencing high signal attenuation. It is noted that the normalized mode patterns of the TE_{01} and TM_{01} mode appear similar to each other, but the direction of the electric field is radically different: the TE_{01} has circular E-field lines and the TM_{01} mode has radial ones. Also, the central peak in the normalized electric field of the HE_{12} mode is barely visible in Fig. 3.5, but closer inspection shows that the polarization and electric field components are similar to those of the ideal HE_{12} mode and very different to those of the TE_{01} and TM_{01} modes. Thus, it can still be categorized as the HE_{12} mode.

3.2.2 Eigenmode simulation of practical Bragg fibre with support bridges

The support bridges, which mechanically maintain the air gaps between dielectric layers, introduce additional EM-field leakage since they act as discontinuities in the photonic crystal, periodically perturbing its structure [130]. The support bridges also cause mode coupling between the guided mode in the core and the surface modes, resulting in a higher propagation loss [113]. However, the desired HE_{11} mode mainly propagates within the core region, and thereby the negative impact of the support bridges on the propagation loss of HE_{11} is relatively small compared to the other competing modes. Nevertheless, it is preferable to use thin support bridges and as few of them as possible to minimize their negative impact. Making use of the DLP rapid prototyping technology, only two bridges per air gap were necessary. Such a highly porous structure would be difficult to achieve with other thermal fabrication technologies owing to the deformation exhibited in the processing [67].

The impact of the support bridges on the desired HE_{11} mode was investigated using the COMSOL eigenmode solver. A practical Bragg fibre with support bridges using the measured data listed in Table 3.1 was simulated. As shown in Fig. 3.6, the presence of the support bridges has negligible impact on the propagation loss of the desired HE_{11} mode, leading

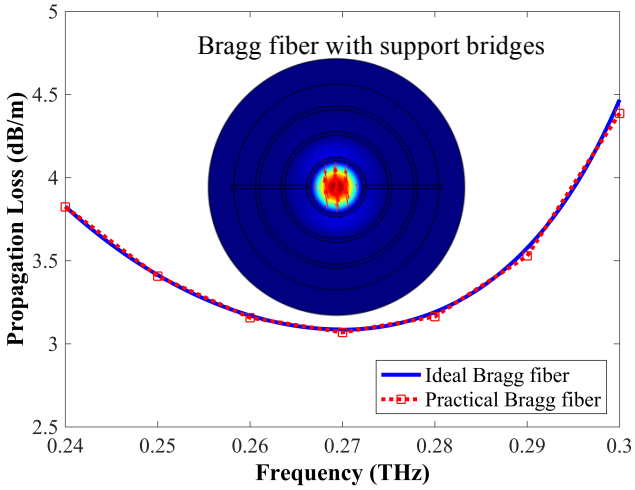

Fig. 3.6 Theoretical propagation losses of HE_{11} mode in ideal and practical Bragg fiber. The inset shows the normalized electric field of the HE_{11} mode in a practical Bragg fiber with support bridges.

us to the conclusion that the negative impact of the support bridges on the propagation loss of the desired HE_{11} mode can be well suppressed provided only a very few support bridges are used, placed perpendicular to the polarization of the HE_{11} mode. Additionally, a high-porosity structure like this fibre is barely achievable using thermal fabrication techniques. The inset shows the mode pattern of the desired HE_{11} mode in this practical Bragg fibre with support bridges; note that the HE_{11} mode is well-confined in the air core, despite the presence of the support bridges.

3.2.3 Propagation simulation of the real Bragg fibre using practical geometry and material parameters

To verify that the fabricated Bragg fibre operates with asymptotically single-mode behaviour, an electromagnetic simulation using the actual as-fabricated geometry and material parameters was carried out using CST Microwave Studio®. The set-up and the simulation results are shown in Fig. 3.7. The total length of the Bragg fibre was 30 mm. An open boundary was applied at the maximum and minimum plane of all directions. The fundamental HE_{11} mode of a hollow cylindrical metallic waveguide (HCMW) was used to feed the Bragg fibre from the left at x = -1.11 mm. x = 0 mm indicates the interface between the HCMW and the Bragg fibre. The mode profile in the Bragg fibre for a frequency of 0.27 THz at x = 1 mm and x = 30 mm are shown in Fig. 3.7 (c) and Fig. 3.7 (d), respectively, from which it can be seen that the mode profile at the front part of the Bragg fibre (x = 1 mm) is a superposition of multiple modes, but eventually the mode profile at the end of the Bragg fibre (x = 30 mm) becomes the desired HE_{11} mode.

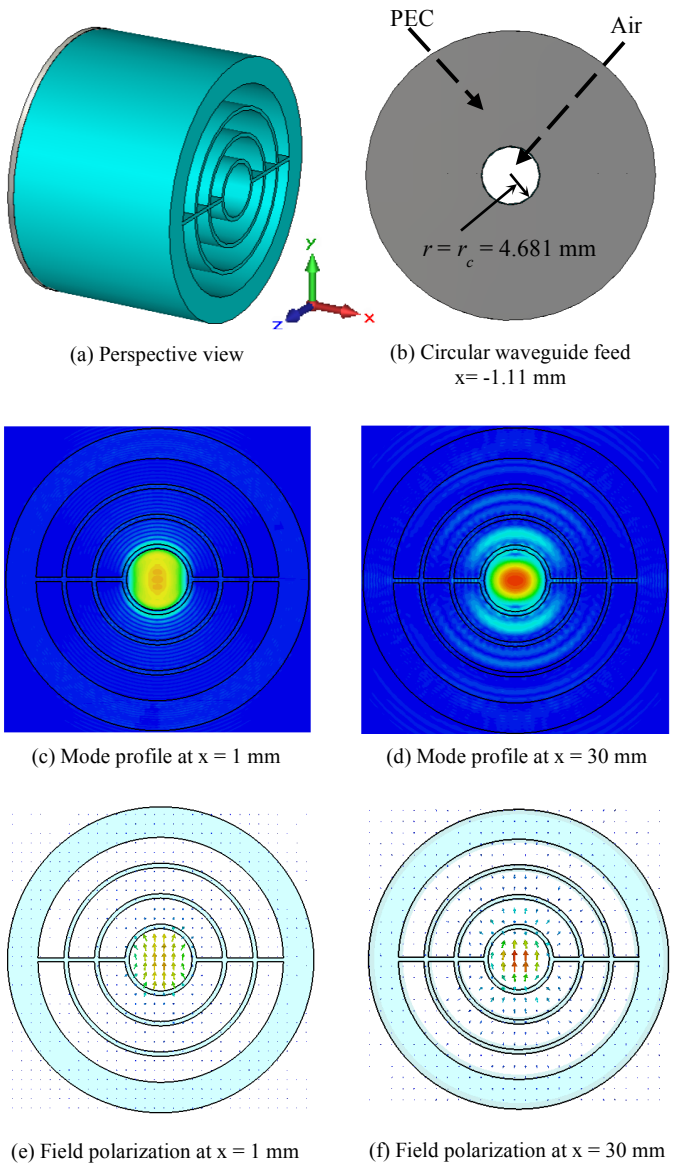

(a) Perspective view

(b) Circular waveguide feed x= -1.11 mm

(c) Mode profile at x = 1 mm

(d) Mode profile at x = 30 mm

(e) Field polarization at x = 1 mm

(f) Field polarization at x = 30 mm

Fig. 3.7 Transmission simulation of the Bragg fibre using practical geometry and material parameters listed in Table 3.1: (a) Perspective view of the setup of the transmission simulation; (b) HCMW feed at x = -1.11 mm; (c) Mode profile at x = 1 mm; (d) Mode profile at x = 30 mm; (e) Field polarization at x = 1 mm; (f) Field polarization at x = 30 mm.

Therefore, the proposed Bragg fibre shows strong mode selectivity while allowing the wave to be transmitted in an asymptotically single-mode pattern.

3.3 Measurement results and discussion

The measurement set-up used is shown in Fig. 3.8. The WR-3 rectangular waveguides (RWG) at both ends are on Oleson Microwave Labs (OML) 220 GHz to 325 GHz frequency extenders, which were connected to a Keysight PNA-X vector network analyser. The left WR-3 RWG was connected to port

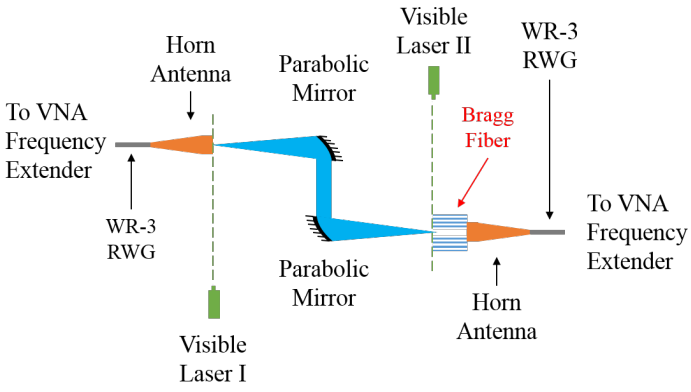

Fig. 3.8 Setup of the characterization experiment. The WR-3 rectangular waveguides at both ends were mounted on OML 220 GHz to 325 GHz frequency extenders which were connected to a Keysight PNA-X.

1 of the PNA-X, and the right WR-3 RWG to port 2. A circular corrugated horn antenna with rectangular waveguide input was mounted on each frequency extender. The EM wave emitted from the left horn antenna was collimated and focused onto the core of the Bragg fibre by a pair of parabolic mirrors. The Gaussian beam profile resulting coupled directly to the desired HE_{11} mode in the fibre. A 2D simulation of the 2-inch diameter 90° off-axis parabolic mirror using COMSOL gives the Gaussian beam waist w_0 at focal point of 3.19 mm, which is about 68.15% of the core radius r_c. Using mode-coupling theory for HCMW [58], the coupling coefficient between the free-space Gaussian beam and the desired HE_{11} mode in the proposed Bragg fibre is estimated to be 88%, thanks to the similar Bessel function patterns between the HE_{11} mode in Bragg fibre and the TE_{11} mode in HCMW. The coupling coefficient into the proposed Bragg fibre is thus fundamentally high. The corrugated horn antenna on the right was placed on a movable stage to permit both alignment with the core at the output end of the Bragg fibre, and the measurement of the Bragg fibres of different lengths. Two auxiliary visible lasers were initially used to determine the focal points of the parabolic mirrors, aiding alignment.

The measured transmission coefficients of the 30 mm and 100 mm Bragg fibres are shown in Fig. 3.9 (a). A standard LRL calibration was performed to shift the reference plane to the output ports of the WR-3 RWGs which were mounted on the frequency extenders, and then a cut-back calibration method [132] was used to calculate the propagation loss which removes the impact of coupling loss between the free-space Gaussian beam and the fibre. However, the cut-back method was not able to remove the systematic phase error caused by impedance mismatch in the transmission path, resulting in the fast ripple in the data. However, it should

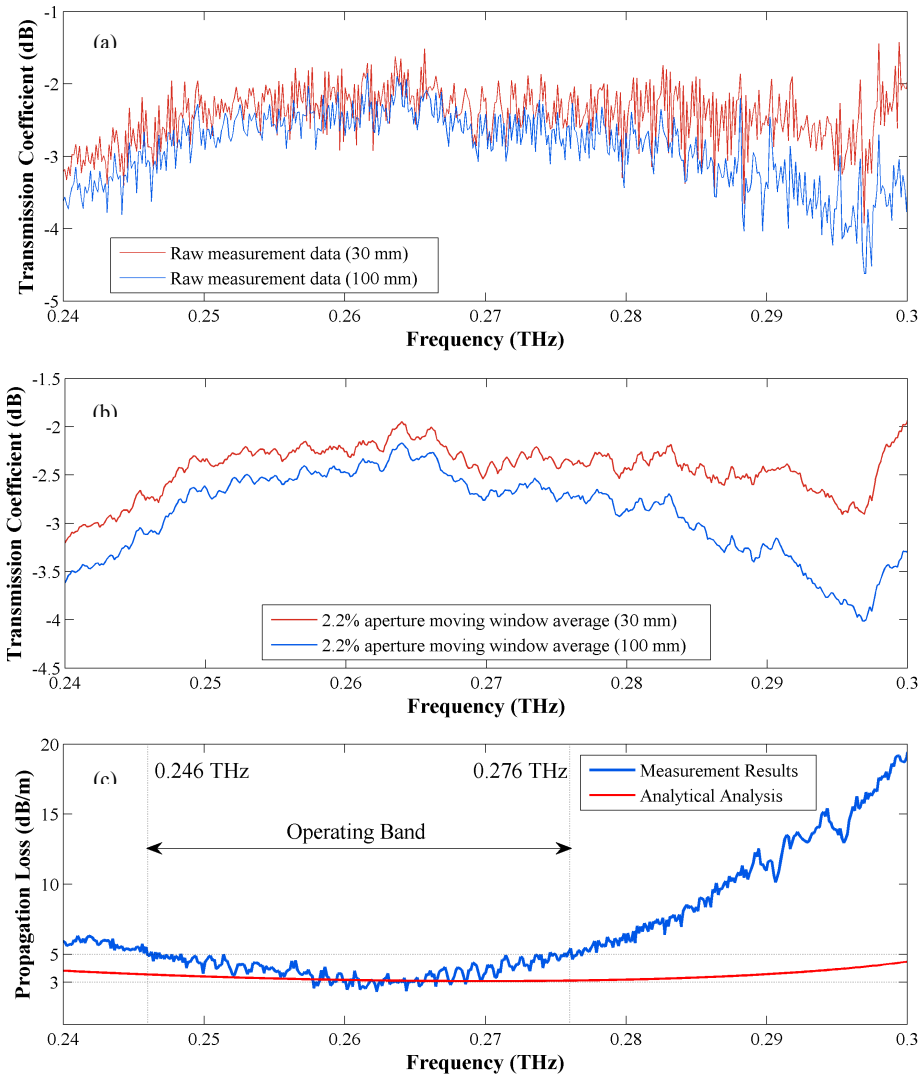

Fig. 3.9 Measurement results. (a) The raw measurement data of the transmission coefficients. (b) The moving window average of the transmission coefficients based on their raw values. (c) The measured propagation loss of the proposed Bragg fibers (blue line) and the analytical analysis result of the desired HE11 mode (red line).

be noted that this frequency domain measurement approach is fundamentally accurate and, while the time domain measurements used for many reported THz waveguides may yield very smooth data, this is only because of the lower level of frequency resolution achievable. The IF bandwidth was set to 100 Hz, the averaging factor was 384, and 456 frequency points were recorded over the truncated frequency range of interest from 0.24 to 0.3 THz. The raw measurement data of the transmission coefficients for the two sample fibres are shown in Fig. 3.9 (a).

To reduce the systematic phase error, a moving window average technique was applied to the raw measurement data of the transmission coefficients, shown in Fig. 3.9 (b). In other words, the transmission coefficient at each

frequency point is the mean value of its 11 nearest neighbour points (including itself), occupying about 2.2% aperture of the frequency range from 0.24 to 0.3 THz. Since the Bragg fibre is a passive component with no resonance peaks in the transmission spectrum, this technique is effective. Therefore, compared with the raw data in Fig. 3.9 (a), the smoothed curves in Fig. 3.9 (b) actually represent the average data of the transmission coefficients.

Using the cut-back calibration method [132] and the average data of the transmission coefficients shown in Fig. 3.9 (b), the measured propagation loss of the proposed Bragg fibre is shown in Fig. 3.9 (c). The blue line shows the averaged measurement value of the propagation loss. Again, the residual fast ripple is still caused by impedance mismatches between components in the transmission path, which is not corrected out with a cut-back calibration. The red line shows the COMSOL simulated propagation loss for the HE_{11} mode of the fabricated Bragg fibre. The averaged measured data is in good agreement with the simulated propagation loss of the HE_{11} mode over the central frequency region from 0.246 to 0.276 THz. From 0.22 to 0.246 THz, and from 0.276 to 0.3 THz, the measured loss of the waveguide is much greater than the simulated HE_{11} result. This is believed to be due to mode transition between the desired HE_{11} mode and other higher order competing modes at these frequencies introduced by the higher propagation loss of the HE_{11} mode and the smaller loss discrimination. Besides, the surface roughness can also contribute more to the loss at higher frequencies due to shorter operating wavelength. Nevertheless, a low average propagation loss, below 5 dB/m across the frequency range of interest from 0.246 to 0.276 THz, was achieved, with an average minimum of 3 dB/m at 0.265 THz.

A comparion of the reported experimental work on THz microstructured fibers is shown in Table 1.1. Among the THz microstructured fibers listed, the work in [48] shows a lower minimum loss at similar frequency range, but its average propagation loss is higher than that of this work. Also, the THz microstructured fiber in [48] does not work in a single-mode pattern, while the proposed Bragg fiber is able to operate in an asymptotically single-mode pattern over the frequency range from 0.246 to 0.276 THz. It is noted that the dielectric-lined hollow cylindrical metallic waveguide in [35] exhibits lower loss at 2.54 THz and can enable quasi-single mode propagation by means of efficient coupling. However, due to the simplicity of its structure, it offers very limited degrees of freedom to optimize the loss discrimination between

its desired mode and higher order competing modes, resulting in multimode interference which causes measurement difficulties, though much longer sample waveguide was used [35]. In contrast, the geometry of the proposed all-dielectric Bragg fiber offers a high degree of freedom to manipulate its photonic bandgap and dispersion curves, and it thereby allows the realization of low propagation loss of the desired mode and large loss discrimination between the desired mode and its competing modes simultaneously, resulting in strong mode selectivity.

3.4 Concluding remarks

In this chapter, the design and measured performance of a THz Bragg fibre, fabricated by digital light processing rapid prototyping, is described, which provides low-loss guiding of THz waves. The Bragg fibre was measured with a free space measurement platform using a Keysight PNA-X and OML frequency extenders, and its propagation loss was extracted using the cut-back calibration method. The results show the average propagation loss of the proposed asymptotically single-mode Bragg fibre is less than 5 dB/m over the frequency from 0.246 to 0.276 THz, which is, to the best of my knowledge, the lowest loss asymptotically single-mode all-dielectric microstructured fibre yet reported in this frequency range, with an average minimum loss of 3 dB/m at 0.265 THz.

Chapter 4
Mode Transitions and Filtering Effect in Asymptotically Single-mode Bragg Fibre

Modal-filtering effect [114, 127, 130], achievable by exploiting loss-discrimination between the nominal operating mode and other competing modes, allows Bragg fibre to operate in an asymptotically single-mode pattern. In such asymptotically single-mode THz Bragg fibre, a certain propagation distance is required to ensure the transition from multimode operating pattern to the effectively single-mode pattern. However, most previously published works on THz waveguides [30, 35, 42, 43, 49-52, 54, 60, 114, 127, 130, 133, 134, 133, 134] only focus on the steady state of the supported propagating modes in the fibre. A rigorous investigation of the EM-field mode transition and filtering processes prior to steady-state propagation is largely lacking. Specifically, it is essential to know the mode transition distance since this determines whether the THz waveguide is suitable for certain applications. For example, due to the small loss discrimination between the desired mode and the unwanted modes, the conventional design principles [114, 115,135] for optical Bragg fibre require several kilometres to eliminate the unwanted modes, and are therefore unsuitable for THz Bragg fibres, which are mainly considered in applications that require much shorter waveguiding distance, such as biological and security imaging [4, 136].

In this chapter, the mode transition and filtering phenomenon is investigated by using a 3D full-wave simulation of the EM wave propagation inside and along the length of a hollow all-polymer THz Bragg fibre, using directly measured material dielectric properties and with real geometric parameters [54]. The THz Bragg fibre discussed here can achieve asymptotical single-mode pattern propagation with large loss discrimination between the fundamental and other higher-order modes. Two different excitation methods (waveguide-port excitation and Gaussian-beam excitation) are considered in the full-wave simulations, representing multimode excitation and quasi-single mode excitation conditions, respectively. Using a multimode waveguide port excitation method, the filtering of different high-order modes, which correspond to different radiation angles, is clearly observed, indicating a good mode selectivity of the proposed Bragg fibre. With appropriate Gaussian-beam excitation, most high-order competing modes can be quickly

and effectively filtered out after a distance of approximately 13.7 free-space wavelengths, and beyond this point, the electric field amplitude of the desired HE_{11} mode is observed to be approximately 7 times larger than the main competing HE_{12} mode's. Additionally, the propagation loss of the HE_{12} mode is more than 10 dB/m higher than that of the fundamental HE_{11} mode. Therefore, the asymptotically single-mode propagation of the desired operational mode can be formed inside the fibre. The simulated propagation loss of the Bragg fibre is approximately 5 dB/m, which is in a good agreement with the experimental result of 3 dB/m, recently published by the authors [54].

4.1 The fibre

The geometry and refractive index profile of the fabricated all-polymer Bragg fibre prototype are shown in Fig. 3.1. The design principles of the fabricated Bragg fibre were reported in Chapter 2 and Chapter 3, and in the previous published papers [54, 121, 130, 137] . It is also briefly summarized as follows:

1) Among several available photopolyers for the EnvisionTEC Perfactory 3 Mini 3D printer, HTM140 is chosen as the material for the high refractive index regions for the proposed hollow-core single-polymer Bragg fibre due to its relatively high refractive index and low material loss.
2) The values of a and b are subsequently chosen based on a generalized half-wavelength condition [130] to provide a wide photonic bandgap centred around 0.27 THz which covers the frequency of interest.
3) The core radius r_c is carefully chosen to place the dispersion curve of

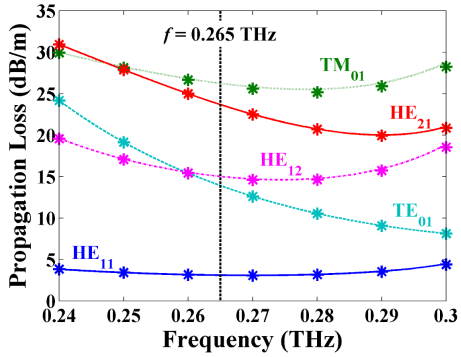

Fig. 4.1 Calculated (lines) and numerically simulated (asterisks) propagation losses of selected lowest-loss supported propagating modes in the fibre without support bridges.

the desired HE_{11} mode in the low confinement loss photonic bandgap region.

4) Both the width of the support bridges w and the thickness of the outermost protective layer t have little influence on the performance of the proposed high-porosity Bragg fibre, and they are chosen based on simulation optimization results.

the propogation losses of the several selected lowest-loss supported modes of the fabricated Bragg fibre can be calculated analytically using a transfer matrix method [87, 119]. The analytical results (lines) based on the transfer matrix method with the simulation results (asterisks) based on COMSOL are shown in Fig. 1 (c). The HE_{11} mode is selected as the fundamental mode as it has the lowest propagation loss over the frequency range from 0.24 to 0.3 THz. Since the HE_{11} mode is a linearly polarized mode which can barely couple with the circularly polarized TE_{01} mode, the main competing mode of HE_{11} is thus HE_{12} rather than TE_{01}. The minimum loss discrimination between the HE_{11} and HE_{12} modes over the frequencies of interest occurs at 0.265 THz, where they show a difference in their propagation loss of approximately 10 dB/m.

4.2 3D Full-wave EM simulation

Unlike standard hollow metallic rectangular or circular waveguides, the

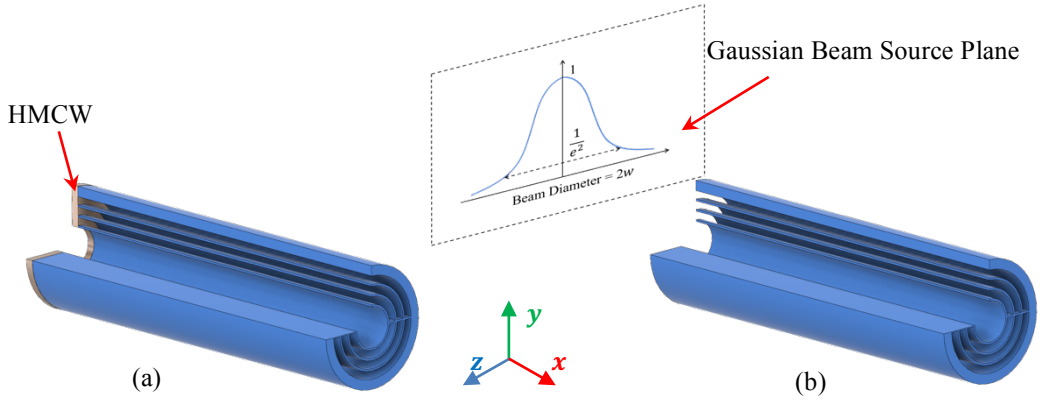

Fig. 4.2 Cutaway views of the proposed Bragg fibre for CST simulation using different excitation schemes. (a) Hollow cylindrical metallic waveguide excitation scheme. The core radius of HMCW is the same as the core radius of the Bragg fibre, namely 4.681 mm. The length of the HMCW is 1.131 mm. (b) Gaussian beam excitation scheme. The distance between the source plane and the input port of the Bragg fibre is 25.4 mm. The focal length and the beam waist of the Gaussian beam are 25.4 mm and 3.604 mm, respectively. The length of the Bragg fibre in both (a) and (b) is 125 mm. The origins of the coordinate in both schemes are placed at the centre of input port of the Bragg fibre.

Bragg fibre is a non-standard waveguide structure which, in practice, requires signal feeding from the other types of waveguide port or from free-space signal sources. In this work, two different excitation methods, conventional waveguide-port excitation and Gaussian-beam excitation, are considered, as shown in Fig. 4.2.

4.2.1 Multi-mode hollow cylindrical metallic waveguide excitation

From Fig. 4.1, at the operational frequency of 0.265 THz, the propagation loss of the HE_{11} mode is lowest. Moreover, the loss discrimination between the HE_{11} mode and the HE_{12} mode is highest as compared to the other frequencies in the operational bandwidth of 0.24 to 0.3 THz. Therefore, the frequency point of 0.265 THz is chosen to analyze the fibre, as indicated by the vertical dashed line in the figure. The 3D full-wave model of the proposed Bragg fibre using the measured geometrical parameters and material dielectric properties, shown in Fig. 4.2, is simulated using the CST Studio Suite®. All boundaries are set as radiation boundaries in order to absorb any incident EM waves. A hollow metallic circular waveguide (HMCW) is used to excite an EM field at $x = 0$ mm. The core radius the feeding waveguide $r_m = r_c = 4.681\ \mathrm{mm}$, and its length $l_m = 1.131\ \mathrm{mm}$ which is the same as the free-space wavelength λ_0 at 0.265 THz. Given the operating frequency f, the criteria allowing a HMCW to work in single-mode pattern is [138]

$$\frac{c}{3.41f} < r < \frac{c}{2.62f} \tag{4.1}$$

where c is the speed of light and r is the core radius. If $f = 0.265\ \mathrm{THz}$, then the criteria becomes $0.332\ \mathrm{mm} < r < 0.432\ \mathrm{mm}$. Since the core radius of the feeding waveguide $r_m = 4.681\ \mathrm{mm} \gg 0.432\ \mathrm{mm}$, the feeding waveguide is highly multimode. Therefore, at the end of the feeding waveguide, the output field pattern is a superposition mode composed from many supported modes. Using a multimode excitation scheme allows better understanding of the filtering of competing higher-order modes in the proposed Bragg fibre. The absolute electric field at 0.265 THz at the $z = 0$ plane, one of the longitudinal symmetry planes of the fibre, is shown in Fig. 4.3 (a). Overall, the EM field is substantially confined to the core of the fibre. However, the fibre does not work in a strictly single-mode pattern, requiring a certain distance before a relatively steady asymptotically single-mode state is obtained. The fibre is divided into two zones, as shown in Fig. 4.3 (a).

In zone I, which extends between $0\ \text{mm} \leq x \leq 16\ \text{mm}$ ($0 \leq x \leq 14.1\lambda_0$), the EM modes transition from HMCW multi-modes to Bragg fibre modes. In this region, several radiation angles can be clearly observed, indicating a relatively strong radiation of electromagnetic field from the air core to the cladding layers. The radiation angles correspond to different supported propagating modes in the Bragg fibre; they are mainly lossy high-order competing modes. Fig. 4.3 (b)–(g) show the transverse mode patterns of several representative points. In zone I, Fig. 4.3 (b)–(e), the gradual changes of the guided mode from a highly superposition mode to a relatively

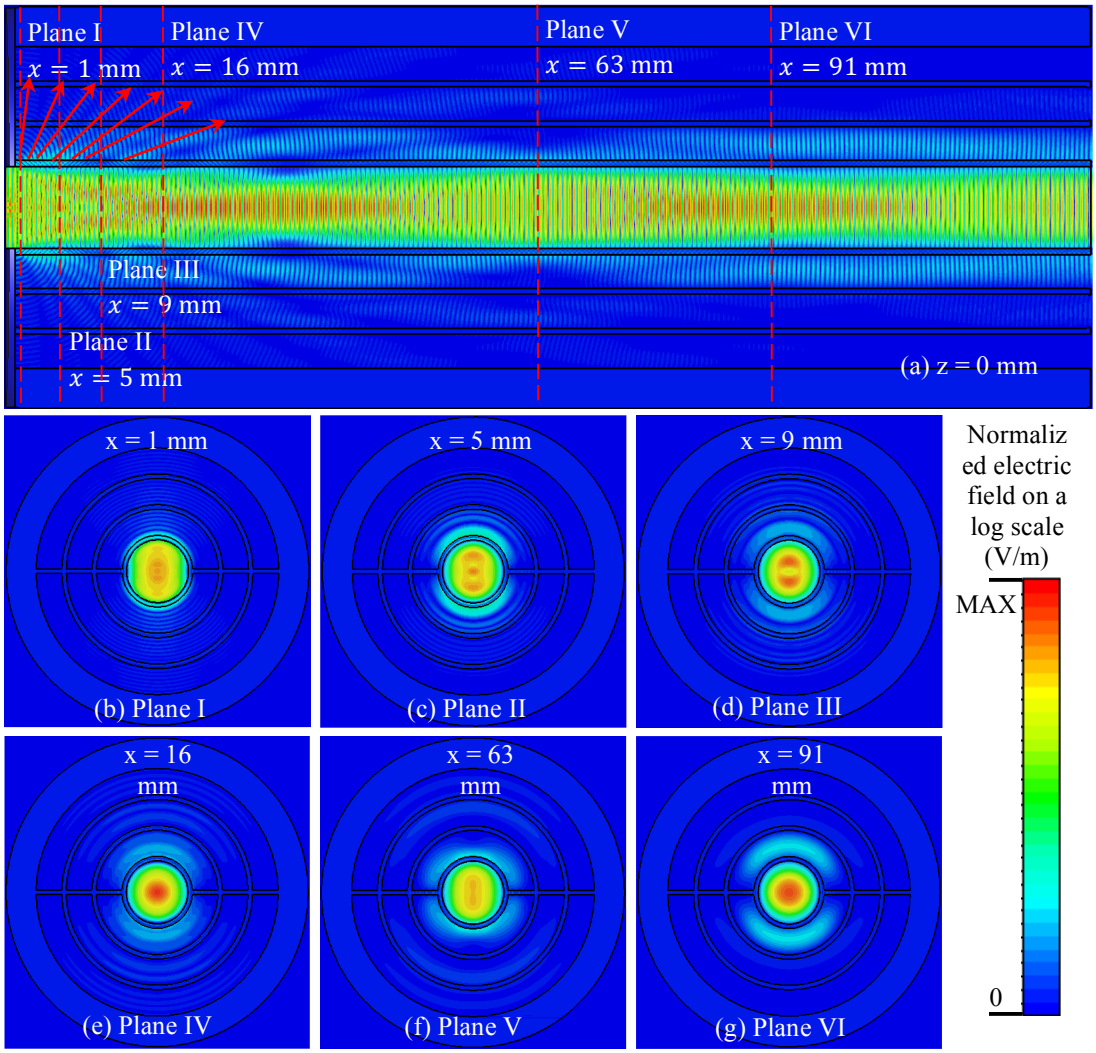

Fig. 4.3 Absolute electric field with HMCW excitation at 0.265 THz using a log scale colour map. The coordinate scheme is the same as that in Fig. 2. (a) $z = 0$ mm plane. Vertical dashed lines represent the positions of different transverse cut planes. Solid red arrows represent the different radiation angles of the electromagnetic field which correspond to different modes. (b) Plane I ($x = 1$ mm). (c) Plane II ($x = 5$ mm). (d) Plane III ($x = 9$ mm). (e) Plane IV ($x = 16$ mm). (f) Plane V ($x = 63$ mm). (g) Plane VI ($x = 91$ mm).

pure HE_{11} mode is achieved. Most higher-order competing modes are filtered out in this zone, allowing the Bragg fibre to operate in a relatively pure EM mode pattern thereafter. However, due to the relatively low loss among the competing modes, a small portion of the main competing mode HE_{12} may still exist in the fibre; it will also be gradually filtered out in the next zone by a modal-filtering effect.

In zone II, for $x \geq 16\ \mathrm{mm}$ ($x \geq 14.1\lambda_0$), a periodic pattern with a period of approximately 61 mm or $53.9\lambda_0$ is observed. This periodic pattern is caused by mode-beating [139,140], from the interference between two modes of slightly different propagation constant. In this case, the two modes are the desired HE_{11} mode and its main competing mode HE_{12}. Fig. 4.3 (f) and Fig. 4.3 (g) show the mode pattern at one representative peak and valley, corresponding to the situation when the two modes are approximately in phase and 180 degrees out of phase, respectively. Fig. 4.3 (f) shows that at the valley, the overall mode pattern behaves similarly to the desired HE_{11} mode, though the slight distortion of the mode pattern also indicates the existence of a small portion of the competing mode. Fig. 4.3 (g) shows clearly the mode pattern of HE_{11} at the beat peak. The residual competing mode in zone II can be gradually filtered out from the fibre by propagation loss, allowing the Bragg fibre to be operated in asymptotically single-mode pattern in this zone and beyond.

4.2.2 Single-mode free-space Gaussian excitation

Like conventional optical fibre and other hollow core THz microstructure fibres [95, 141, 142], Bragg fibres can be excited using a focused Gaussian beam. The EM mode transitions from the free-space Gaussian mode into a

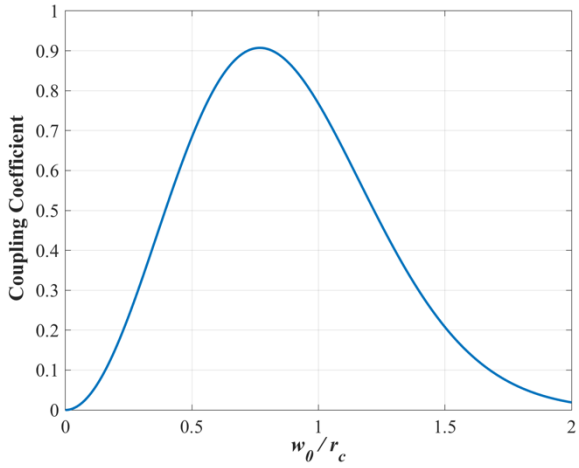

Fig. 4.4 Estimated coupling coefficient between the free-space Gaussian beam and the HE_{11} mode in the proposed Bragg fibre.

guided Bessel-function mode within the Bragg fibre. The mode transition process is closely related to the mode coupling at the input port. An efficient input coupling leads to a smooth mode transition process, consequently reducing the overall losses of the fibre [84, 95].

As the mode pattern of the desired HE_{11} mode in the Bragg fibre is similar to that of the TE_{11} mode in HMCW. The mode-coupling theory [58, 143], which describes the coupling coefficient of TE_{11} mode in HMCW when excited by a Gaussian beam can be used to estimate the efficiency of coupling from free-space Gaussian beam into the Bragg fibre, as shown in Fig. 4.4. When the ratio of the Gaussian beam waist to the core radius w_0/r_c is equal to 0.77, the coupling coefficient is as high as 90%. This ratio can be also used to maximize the coupling coefficient of the HE_{11} mode in Bragg fibre, as well as

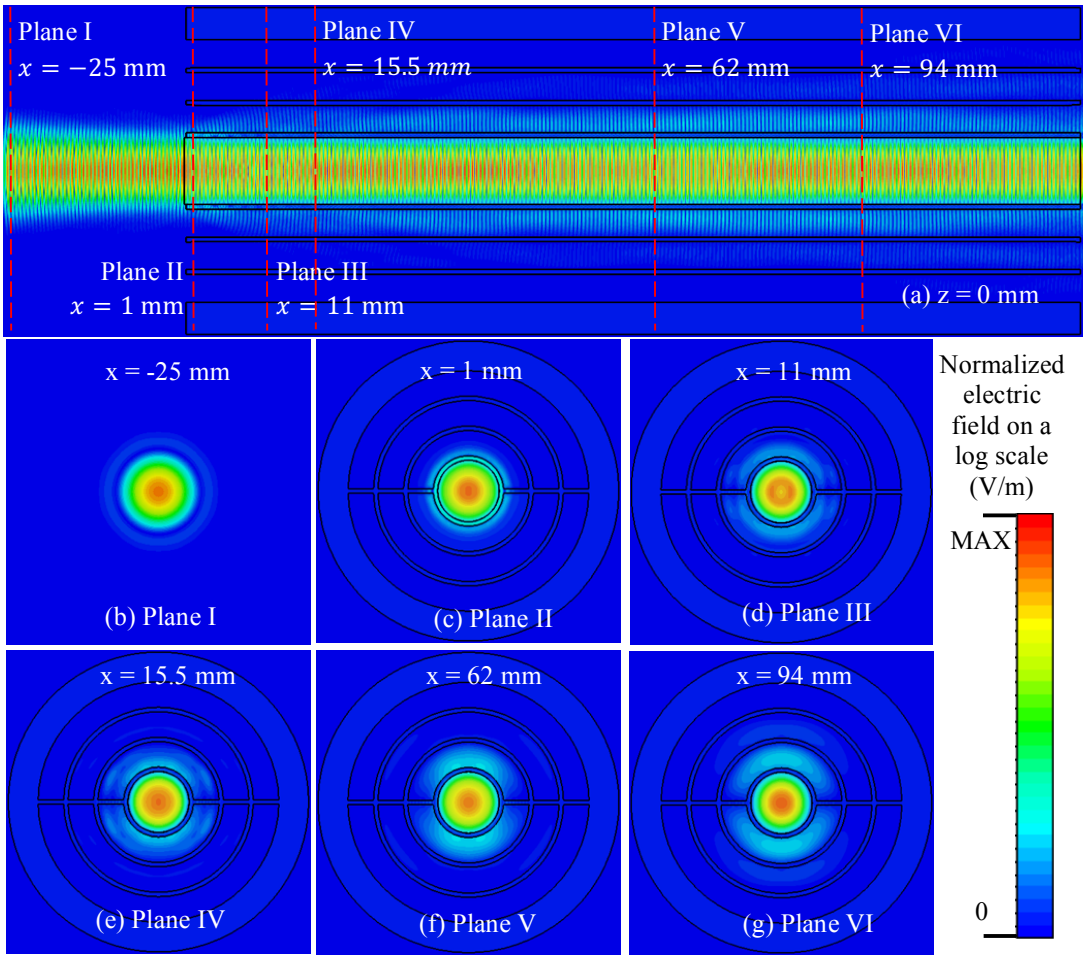

Fig. 4.5 Absolute electric field with focused Gaussian beam excitation at 0.265 THz using log scale colour map. The Gaussian beam is excited at the $x = -25.4$ mm plane and focused at the input port of the fibre with a beam width at beam waist $w_0 = r_c$. The coordinate scheme is the same in Fig. 2. (a) $z = 0$ mm plane. (b) Plane I ($x = -25$ mm). (c) Plane II ($x = 1$ mm). (d) Plane III ($x = 11$ mm). (e) Plane IV ($x = 15.5$). (f) Plane V ($x = 62$ mm). (g) Plane VI ($x = 94$ mm).

to suppress the coupling of Gaussian beam to other competing modes.

Since the core radius of the Bragg fibre $r_c = 4.681$ mm, a Gaussian beam waist $w_0 = 0.77r_c = 3.604\,\mathrm{mm}$ is set in the full-wave simulation to maximise the coupling coefficient. The absolute electric field at the operating frequency of 0.265 THz at the $z = 0\,\mathrm{mm}$ plane is shown in Fig. 4.5 (a), while Fig. 4.5 (b)–(g) show the transverse mode patterns at several representative points. From Fig. 4.5, when using free-space Gaussian beam as the feeding source (Plane I), the mode pattern at the input port of the fibre (Plane II) is relatively pure and close to the mode pattern of the desired HE_{11} mode. Additionally, compared with the strong radiation of electromagnetic field at the input of the fibre in the previous excitation scheme using HMCW, the radiation of the wave at the same part of the fibre in this excitation scheme is much weaker, and only very few radiation angles are observed. However, due to the impedance mismatch at the input interface of the fibre, a small amount of EM energy of the main competing mode HE_{12} is excited and causes a slight distortion on the overall mode pattern at Plane III, but the mode pattern quickly converges to the HE_{11} mode at $x = 15.5\,mm$ (Plane IV), which is approximately $13.7\lambda_0$. After this point, although the phenomenon of mode beating also exists, the amplitude of the mode beat is relatively weak, compared with the previous multi-mode excitation scheme using HMCW. Besides, the mode pattern at the beat valley (Plane V) is still well maintained as the desired HE_{11} mode and the distortion caused by the HE_{12} mode can barely be observed, suggesting that the amplitude of the competing HE_{12} mode is much weaker than that of the desired HE_{11} mode.

Therefore, compared with the previous excitation scheme using HMCW, the excitation scheme using a proper Gaussian beam in this design can lead to a better mode transition process and a shorter transition distance, and the fibre can operate in effectively asymptotically single-mode pattern after the transition point at around 13.7 operating wavelengths. When comparing the

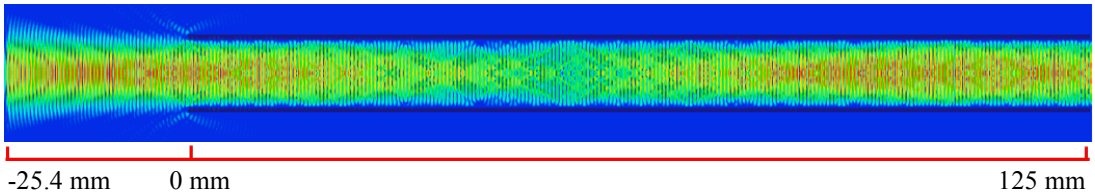

Fig. 4.6 Absolute electric field of the electromagnetic field propagating in HMCW at $z = 0\,\mathrm{mm}$ plane at 0.265 Hz. The core radius of the HMCW is 4.681 mm. The Gaussian beam excitation source is placed at $x = -25.4\,\mathrm{mm}$. The parameters for the Gaussian beam are the same as those in Fig. 4.5 (a).

Bragg fibre with a conventional HMCW which uses the same radius as the air core, the single mode selection in Bragg fibre is much more obvious. Fig. 4.6 shows the EM-wave propagation in HMCW with Gaussian beam source excited from the left. The mode pattern in the HMCW is highly multimode, while, under the same excitation condition, the Bragg fibre works in effectively asymptotically single-mode pattern.

4.3 Mode Competing and filtering

4.3.1 Mode beat

When two competing modes with slightly different propagation constants simultaneously exist in the Bragg fibre, a periodic variation in the amplitude of the electric field can be observed, which is also known as mode beating [144]. Considering two EM waves of significantly different amplitudes added together linearly:

$$A\cos(2\pi\upsilon_1 x) + B\cos(2\pi\upsilon_2 x) =$$
$$(A-B)\cos(2\pi\upsilon_1 x) + 2B\cos(2\pi\frac{\upsilon_1+\upsilon_2}{2}x)\cos(2\pi\frac{\upsilon_1-\upsilon_2}{2}x) \qquad (4.2)$$

Here, A and B are the amplitudes of the two waves, where $A \gg B$. $\upsilon_n = 1/\lambda_{gn} = \beta_n/2\pi$ $(n \in \mathbf{N})$ is the spatial frequency of a wave, where n is an identifier associated with different waves, λ_g is the guide wavelength and β is the longitudinal wave propagation number. υ_1 and υ_2 are quite close to each other. In the second term of the right side of Eqn. (4.2) the frequency $(\upsilon_1 - \upsilon_2)/2$ is perceived as a periodic variation in the amplitude of the tone $(\upsilon_1 + \upsilon_2)/2$. In addition, since $A \gg B$, the overall amplitude of the superposition mode is mainly dominated by the first term of the right side of the Eqn. (4.2), while beat amplitude is mainly dominated by the second term.

To quantitatively understand the mode competition in the Bragg fibre, based on Fig. 4.5 (a), E_y along the x-axis of the fibre is plotted in Fig. 4.7. x ranges from -25 mm to 125 mm, with a step size of 0.25 mm, which is about 22% of the guide wavelength of the HE_{11} mode, making it an appropriate step size to observe the high-frequency changes within one wavelength. In zone I, the wave propagates in the free-space region. In zone II, the free-space Gaussian beam transitions into Bessel function modes supported by the Bragg fibre. A sharp reduction of the amplitude of E_y at around $x = 11$mm or $x = 9.7\lambda_0$ is mainly attributed to the rapid increase of the higher-order competing modes due to the structure discontinuity at the input port of the fibre. In zone III, the amplitude of E_y varies periodically and decays as a

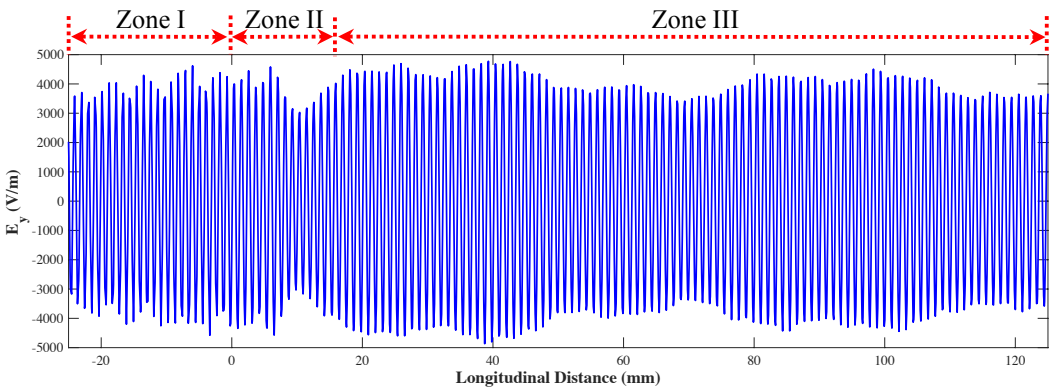

Fig. 4.7 Plot of E_y along the x-axis of the fibre. In zone I ($-25.4\ \mathrm{mm} \leq x \leq 0\ \mathrm{mm}$), the wave travels in free space. Zone II ($0\ \mathrm{mm} \leq x \leq 15.5\ mm$) is a mode transition region where the free-space Gaussian beam transitions into a Bessel function. In zone III ($15.5\ \mathrm{mm} \leq x \leq 125\ mm$), the proposed Bragg fibre operates in an asymptotically single-mode pattern.

result of both mode beating and propagation loss. The amplitude of the envelope for the beat is relatively small, however, compared with the amplitude of the signal.

To compare the EM-field strength of the main HE_{11} mode and its competing mode in zone III, a discrete Fourier transform is used to transform the E_y signal in zone III from the spatial domain to the spatial-frequency domain (Fig. 4.8). The spatial spectrum is relatively clean compared to that of the multimode excitation method, indicating a good mode selectivity of the Bragg fibre. The main peak at 894.5 m^{-1} corresponds to the desired HE_{11} mode. The secondary peak at 848.9 m^{-1} corresponds to the main competing HE_{12} mode. The amplitude of the main peak is about 7 times of the amplitude of the secondary peak. This agrees well with the previous analyses as in Eqn. (4.2) and Fig. 4.7. The superposition of HE_{11} and HE_{12} creates the mode beating in zone III, and the overall amplitude of the signal in zone III is dominated by the desired HE_{11} mode, while the HE_{12} mode dominates the amplitude of the envelope of the beat. The large differences between the amplitudes and the propagation losses of the desired mode HE_{11} and the main competing mode HE_{12} allow the fibre to operate in effectively asymptotically single-mode pattern in zone III.

Based on the cut-back method by comparing the amplitude of E_y at the start ($x = 15.5\ \mathrm{mm}$) and the end ($x = 125\ \mathrm{mm}$) of the zone III, the propagation loss of the fibre is estimated to be 4.78 dB/m, which is comparable to the experimental result of 3 dB/m in the previous experimental work presented in Chapter 2 and [54].

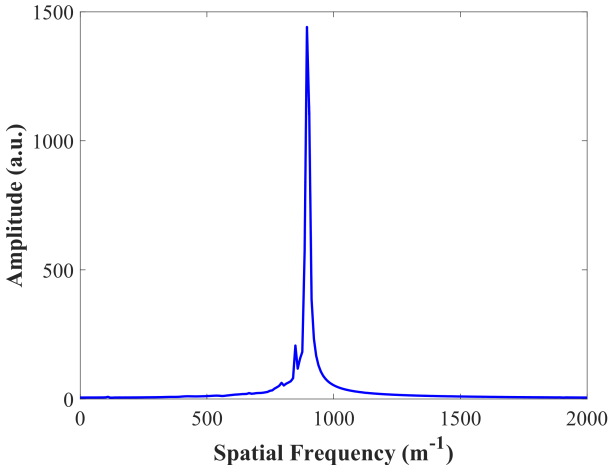

Fig. 4.8 Discrete Fourier transform of the E_y signal in zone III of Fig. 4.7.

4.3.2 Mode filtering

In addition to the significant differences of the amplitude of the electromagnetic fields between the desired HE_{11} mode and its competing modes when the fibre has an efficient Gaussian-beam excitation source, substantial differences in the attenuation rate between fundamental HE_{11} and higher-order modes also contribute to the mode selection, creating a modal-filtering effect. Based on the theoretical results shown in Fig. 4.1, Fig. 4.9 shows the attenuation of the HE_{11} mode and its competing modes as a function of the propagation distance. At the distance of 200 mm, the power of the main competing mode HE_{12} drops by one half (-3 dB), while the attenuation of the HE_{11} mode is only 0.62 dB, and the difference of the propagation loss of these two modes is as large as 10 dB/m. Therefore, significant differences in the amplitude and the attenuation rate between the HE_{11} mode and its competing modes allow the fibre to operate in effectively

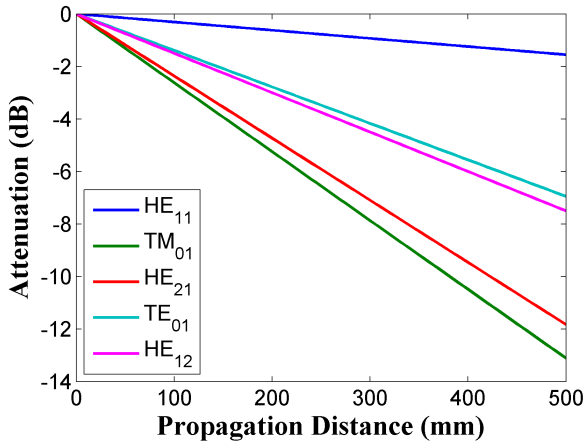

Fig. 4.9 The attenuation of the desired HE_{11} mode and its main competing modes as a function of the propagation distance at 0.265 THz.

asymptotically single-mode pattern with low propagation loss.

4.4 Concluding remarks

In this chapter, 3D full-wave simulations have been used to study the mode transition and filtering in an asymptotically single-mode hollow THz Bragg fibre. The Bragg fibre was designed to support asymptotically single-mode operation centred at 0.265 THz. With multimode excitation using HMCW, good suppression of the higher-order competing modes was observed in the mode transition zone of the fibre. Using a Gaussian beam excitation source, a smoother and shorter transition zone was achieved, which is highly desirable in practical applications. The phenomenon of mode beating, caused by the superposition of the desired HE_{11} mode and its main competing mode HE_{12}, was also observed. However, due to the large discrimination between the amplitudes and the propagation losses of the modes, the proposed Bragg fibre can still operate in an effectively asymptotically single-mode pattern, making it a strong candidate as a low-loss interconnects for THz systems.

Chapter 5
Design and Measurement of a Hollow Photonic Crystal Integrated Waveguide

In this chapter, a novel hollow photonic crystal integrated waveguide (HPCIW) is proposed, which is comprised of an air-core line-defect hexagonal dielectric photonic crystal waveguide sandwiched between two parallel metal plates, as shown in Fig. 5.1. In the horizontal direction, the EM wave is strongly confined in the air core owing to the photonic bandgap effect, while in the vertical direction, the EM wave bounces between the two parallel metal plates. Hence, the proposed waveguide possesses the merits of both SIW and photonic crystal waveguide, but eliminates their drawbacks. Namely, it completely eliminates the need for SIW via metallization, thus simplifying the fabrication process; this is important because the size of vias decreases significantly with increasing operating frequency. Besides, both SIW and photonic crystal waveguide are well-known platforms for functional components and circuit design [76, 77], and HPCIW adopts some of their best features. In addition, in contrast to the photonic crystal waveguide, the HPCIW tightly confines the EM wave in the air core, so it is insensitive to its surroundings, making it a strong candidate for compact and multilayer mmW and THz system-in-package applications.

Theoretical design of the proposed HPCIW was performed using the MIT Photonic-bands (MPB) package [145], which indicated that the HE_{10} mode is supported over a fractional bandwidth of 26% centred at $0.453\,c/a$, and a zero group-velocity dispersion point is found at $0.457\,c/a$, where c is the speed of light and a is the lattice constant for the hexagonal photonic crystal.

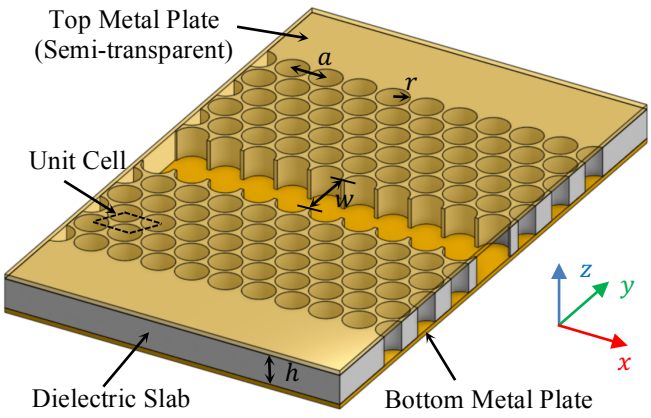

Fig. 5.1 Trimetric view of the HPCIW.

Selecting 4.106 mm as the value of a, a HPCIW operating in the Ka-band was fabricated and characterised. By changing the lattice constant of the photonic crystal and properly choosing the dielectric material, the design here presented can be easily scaled to higher frequencies for THz and optical applications.

5.1 Dispersion relation and guided modes

Fig. 5.1 shows the schematic of the proposed HPCIW with the key design parameters indicated. The top and bottom layers are a pair of parallel metal plates, while the middle layer is an air-core line-defect hexagonal dielectric photonic crystal [146]. The photonic crystal consists of hexagonal arrays of air holes in the dielectric slab. Compared with conventional hollow metallic rectangular waveguide or SIW, the proposed HPCIW removes the metallic parts at the side regions in y direction. It helps to eliminate conduction current flow between the two metallic parallel plates, which is the main source of Ohmic loss for the fundamental HE_{10} mode, replaced by displacement current flow.

The material for the dielectric slab is desired to be high permittivity and low loss, to create a significant photonic bandgap and to reduce the material

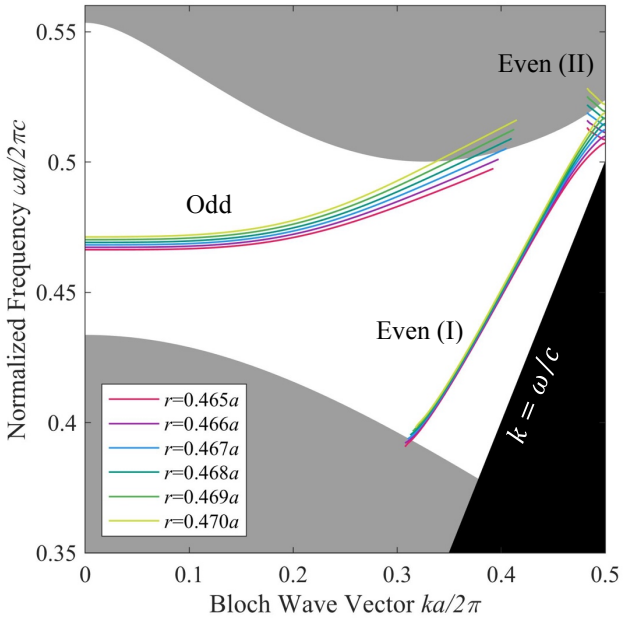

Fig. 5.2 Band diagram and dispersion curves for the vertically polarized modes in the line-defect photonic crystal waveguide. The even and odd modes here correspond to the symmetric and antisymmetric modes with respect to the x- z plane. The black region below the light line ($k = \omega/c$) shades the slow modes that are not guided by the HPCIW.

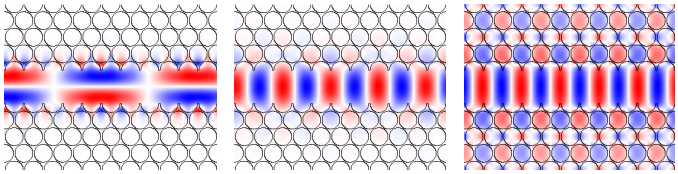

(a) Odd mode (b) Even mode (I) (c) Even mode (II)

Fig. 5.3 Mode patterns when $r = 0.467a$. (a) $(k_n, \omega_n) = (0.1, 0.4687)$; (b) $(k_n, \omega_n) = (0.4025, 0.4512)$; (c) $(k_n, \omega_n) = (0.4925, 0.5159)$. Here, $k_n = ka/2\pi$ and $\omega_n = \omega a/2\pi c$. Periodical boundaries are applied.

absorption loss. Taking into account the available fabrication techniques, Rogers RO3010™ material was chosen for the dielectric slab. Its design Dk (dielectric constant) is 11.2 between 8 and 40 GHz and loss tangent is 0.0022 measured at 10 GHz, according to the datasheet obtained from the manufacturer. Two rows of unit cells are missing in the photonic crystal, so creating an air-core line defect, with width $w = \sqrt{3}a$, where a is the lattice constant of the photonic crystal. A line defect with an integer number of missing unit cells helps to maintain the periodicity of the photonic crystal structure if there are waveguide bends in the structure, and thereby reduces other unwanted defects. The radius of the air holes, r, is chosen to be $0.467a$. The reason for choosing this value will be explained later.

The fundamental mode of the proposed HPCIW is a vertically polarized HE_{10} mode. Like SIW, the height of the HPCIW, h, is adjustable, but it will slightly affect the performance, and will introduce high order modes if the value of h is too large [147]. In this chapter, a HPCIW with a thin dielectric slab, namely, $h < w/2$, is considered. Since the electric field of the HE_{10} mode is evenly distributed along the z-axis, the height of the HPCIW does not contribute to the dispersion relation. Therefore, the problem about dispersion relation is simplified to a two-dimensional (2D) problem in the x-y plane, and it represents the eigenvalues for the vertically (z-axis) linearly polarized modes confined in the air core of the line-defect photonic crystal waveguide.

The dispersion curves for the guided modes in the 2D line-defect photonic crystal waveguide were numerically studied by using MPB, as shown in Fig. 5.2. The dispersion curves related to different values of r are presented, but the band diagram (the gray regions) only corresponds to $r = 0.467a$, which is why the dispersion curves of $r = 0.467a$ are properly aligned with the edge of the band diagram while others are not. For $r = 4.67a$, the mode pattern of the even and odd modes in Fig. 5.2 are shown in Fig. 5.3. As it can be seen, both the odd mode and the even mode (I) can be tightly confined by the line defect, but the even mode (II) is much more lossy with

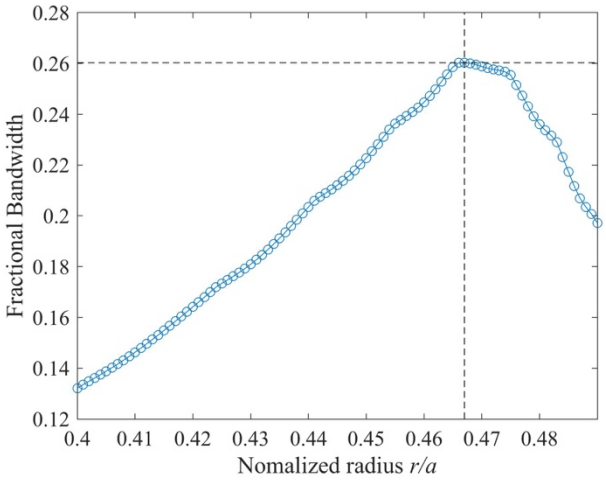

Fig. 5.4 The dependence of the fractional bandwidth on the normalized radius.

significant field penetrating into the bulk of the photonic crystal. This is because the dispersion curve of the even mode (II) is close to the edge of the band diagram where the degree of confinement is reduced [130]. The even mode (I) is the desired fundamental mode, and by appropriate coupling in to this field pattern of the HPCIW, avoiding excitation of the odd mode, the waveguide can operate in single mode fashion [17].

Fig. 5.2 shows the dispersion curve of the even mode (I), which is folded at the Brillouin zone edge ($k = \pi/a$) and turns into the even mode (II) [148]. There is a gap at the Brillouin zone edge between the even mode (I) and the even mode (II) where neither of them can propagate in the HPCIW. The impact of the radius of the air holes, r, on the dispersion curves is also shown in Fig. 5.2. The radius changes the dispersion curves continuously and predictably. The operating fractional bandwidth of the desired even mode (I) is related to the radius, r, as shown in Fig. 5.4. Here, the fractional bandwidth is defined as $\Delta = (\omega_n^h - \omega_n^l)/[(\omega_n^h + \omega_n^l)/2]$, where ω_n^h and ω_n^l are the upper and lower bounds of the dispersion curve for the even mode (I) in the bandgap, respectively. The bandwidth is maximum, $\Delta = 0.26$, when $r/a = 0.467$. This explains the reason for the choice of $0.467a$ for the radius of the air holes. It is noted that a photonic crystal with wider bandgap more strongly confines the field in the line defect, thus reducing the leakage of the wave from the waveguide [130].

The group velocity and GVD of the even mode (I) when $r/a = 0.467$ are plotted vs. normalized frequency in Fig. 5.5. The GVD is defined as $\partial^2 k/\partial\omega^2$. Fig. 5.5(a) shows that as the frequency increases, the group velocity first

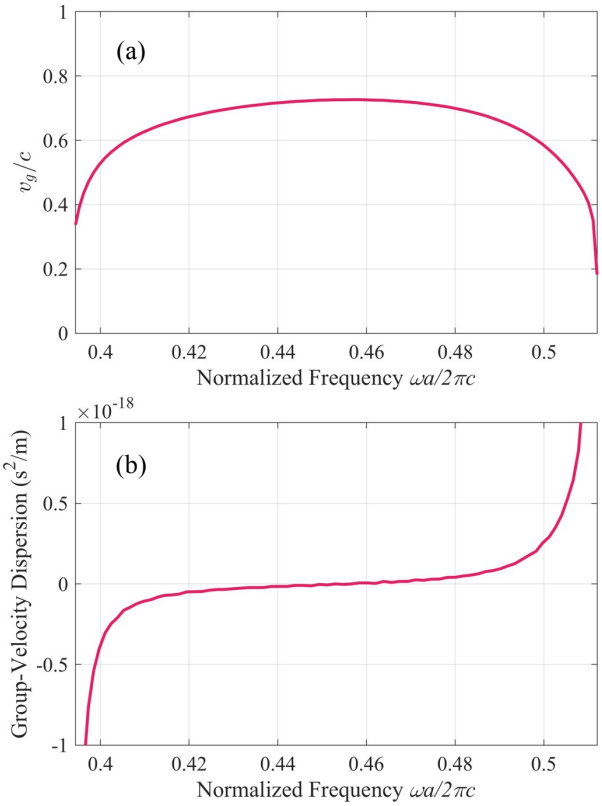

Fig. 5.5 (a) Normalized group velocity and (b) group-velocity dispersion.

increases and then decreases, with the turning point occurring at $0.457a$ where the zero GVD occurs, as seen in Fig. 5.5(b).

The design presented here is scalable. One can achieve this by changing the lattice constant of the photonic crystal, and by properly choosing a low-loss and high-permittivity material which suits the target frequency band. In the next section, a design at Ka-band by choosing Rogers RO3010™ as the host material and setting $a = 4.106$ mm will be demonstrated.

5.2 Fabrication

Considering the full 3D geometry of the proposed HPCIW shown in Fig. 5.1, the even mode (I) shown in Fig. 5.3(b) becomes the HE_{10} mode. Fig. 5.6 shows the CAD design of the HPCIW. The colours do not reflect the original colours of materials for the purpose of distinguishing different sections. A short section of microstrip line is used to couple the signal into the HPCIW, since the quasi-TEM field pattern of the microstrip line is also an even mode with respect to the $x-z$ plane, and the field of the microstrip line beneath the signal track is also basically vertically polarized, thus matching the polarization of the HE_{10} mode. Fig. 5.7 show the fabricated thru-reflect-line (TRL) calibration set and the device under test (DUT) before final assembly.

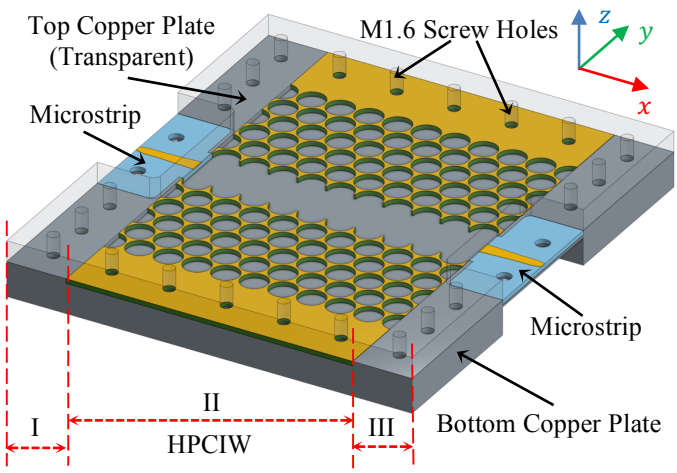

Fig. 5.6 CAD design of the HPCIW. The HPCIW in region II is fed by microstrips in regions I and III.

As shown in Fig. 5.7, 2.4 mm female end launch connectors (obtained from Southwest Microwave Inc.) are used to connect to the microstrip lines and then 2.4 mm coaxial cables go to the VNA. The input end of the microstrip line is designed to fit the dimensions of the end launch connector, and the other end of the microstrip line is designed to match the impedance of the HPCIW. The microstrip line therefore tapers gradually between the two ends. The material chosen for the microstrip fed lines is Rogers RT/duroid® 5880LZ™, whose dielectric constant is 2.00 between 8 GHz and 40 GHz and loss tangent is 0.0021 at 10 GHz. It is one of the lowest dielectric constant materials with acceptable loss tangent available from Rogers. Choosing a low dielectric constant material as the substrate of the microstrip feeds aims to reduce the signal reflection between the microstrip and the HPCIW. The dielectric thickness and copper cladding thicknesses (both sides) of the RT/duroid® 5880LZ™ boards are 0.635 mm and 17.5 μm, respectively. Double-sided copper-clad Rogers RO3010™ was used as the host material for the photonic crystal structure. A significant dielectric constant contrast was thus achieved between the dielectric material and the air holes to form a large photonic bandgap. The thicknesses of the dielectric and copper claddings of the RO3010™ boards were 0.635 mm and 17.5 μm, respectively.

Both the microstrip feeds and the photonic crystal structures were machined using an LPKF ProtoLaser U3. The fabrication was sufficiently precise, but the walls of the hexagonal holes were slightly burnt by the laser with a very small amount of burnt dielectric material left surrounding the bottom edge of the air holes, as shown in the inserted picture in Fig. 5.7(d). Since cleaning the residual burnt dielectric materials manually could have damaged the

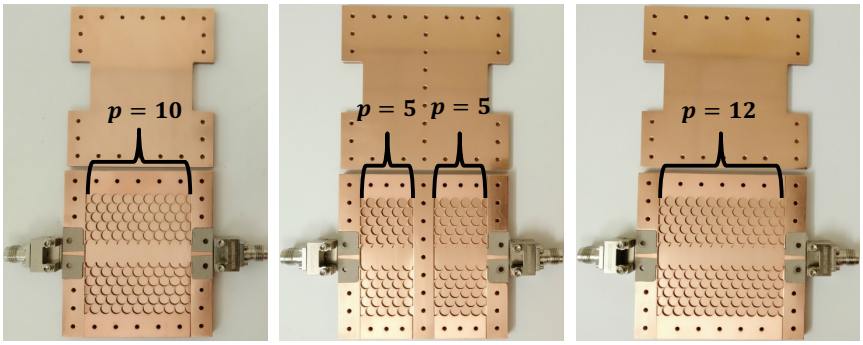

（a）Thru　　（b）Reflect　　（c）Line

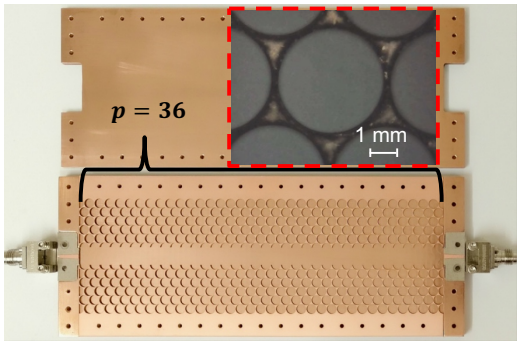

（d）DUT

Fig. 5.7 Photograph of the TRL calibration set and the DUT before final assembly. p is the period number of the photonic crystal in $\boldsymbol{x}$ direction. Same pairs of 2.4 mm female end launch connectors and microstrip lines are used in each device for minimize the repeatability issues.

structure, this material was left in place. The copper cladding of the RO3010™ was not removed from the dielectric in order to provide extra mechanical support for the delicate photonic crystal structure. The copper cladding was not originally incorporated in the design of the HPCIW, but as the thickness was only about 0.2% of the free-space wavelength at the central frequency at 33 GHz and about 2.7% of the dielectric thickness, the residual copper claddings should have negligible impact on the dispersion relation, and only very slightly increase the overall propagation loss, as confirmed by additional simulations.

The top and bottom copper plates are made of C101 copper. The copper plates were first machined with a DMU 40 CNC milling machine and then manually polished by using 500 grade wet and dry silicon carbide. The bottom plates had CNC milling tool marks on the surface. The surface finish of the top plates, which does not require CNC processing, was smooth, but the surface finish of the bottom plates was relatively poor due to the tool marks since CNC processing is required to create a concave space to mount the photonic crystals and microstrip lines.

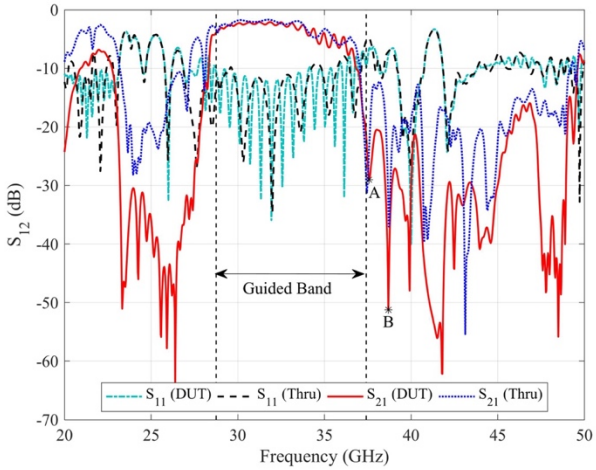

Fig. 5.8 Simulated s-parameters for the thru and DUT shown in Fig. 5.7. The frequencies of the points A and B are 37.58 GHz and 38.69 GHz. The guided band, ranging from 28.75 to 37.41 GHz, indicates the lower and upper bands for the even mode (I) shown in Fig. 5.2.

5.3 Simulation

The thru and DUT shown in Fig. 5.7 were simulated using the CST time-domain solver. A simplified 50Ω coaxial connector, mimicking the actual end launch connector, was used to feed the signal to the microstrip line in the simulation. The simulated S-parameters for the thru and DUT are presented in Fig. 5.8. From Fig. 5.8, an obvious transmission window from 28.75 GHz to 37.41 GHz was observed, agreeing well with the theoretical predictions based on the dispersion curve of the even mode (I), as shown in Fig. 5.2. The upper bound of the transmission window is coincident with point A, which confirms the existence of the frequency gap between the even mode (I) and even mode (II) at the Brillouin zone edge shown in Fig. 5.2. The

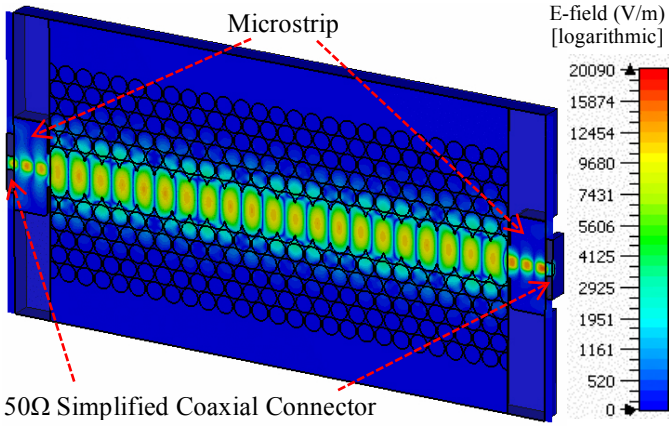

Fig. 5.9 Electric field pattern of the DUT in log scale at 33 GHz. Two 50Ω simplified coaxial connector models are used to feed the microstrip lines.

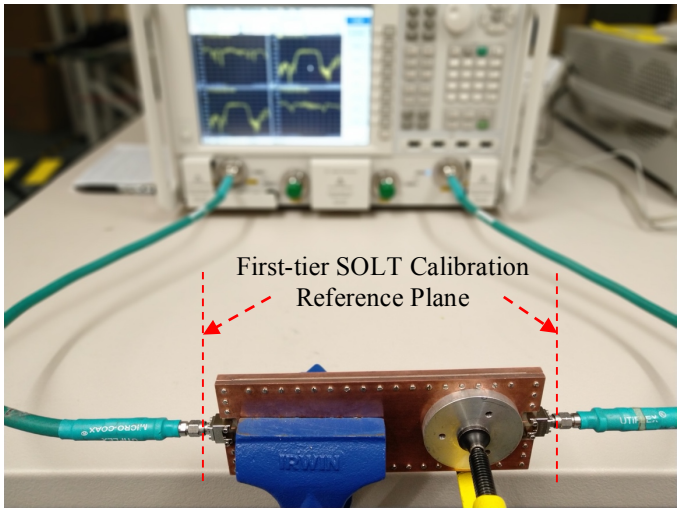

Fig. 5.10 Measurement Setup. SOLT calibration was applied to set the reference plane to the ends of the 2.4 mm coaxial cables. Clamps were used to squeeze out the air gaps between the metal plates and the photonic crystal layer as much as possible.

return loss within the transmission window is about 10 dB, indicating most power is coupled into the HPCIW. Above point A, the HPCIW works in the even mode (II) fashion. The reduction of transmission at the point B results from the cross-coupling between the even mode (II) and the cladding modes [146].

Fig. 5.9 shows the electric field pattern of the DUT at 33 GHz. The waveguide operates in single-HE_{10}-mode, and the electric field is strongly confined in the line defect. The reflection between the microstrip line and the HPCIW is small, indicating that the signal is properly coupled into the HPCIW from the microstrip.

5.4 Measurement

A photograph of the measurement setup is presented in Fig. 5.10. The samples and connectors were cleaned carefully with isopropanol (IPA) before testing. A two-tier calibration technique was used to characterise the HPCIW. The first-tier Short-Open-Load-Thru (SOLT) calibration was performed using a 2.4mm mechanical calibration kit to place the reference planes to the ends of the coaxial cables. The second-tier calibration used TRL calibration [149] to shift the reference plane from the input port of the end launch connectors to the middle of thru line as shown in Fig. 5.7.

The raw measurement data after first-tier SOLT calibration are shown in Fig. 5.11. From Fig. 5.11(a), a transmission window that matches the simulation results can be clearly observed, with a frequency range which also agrees

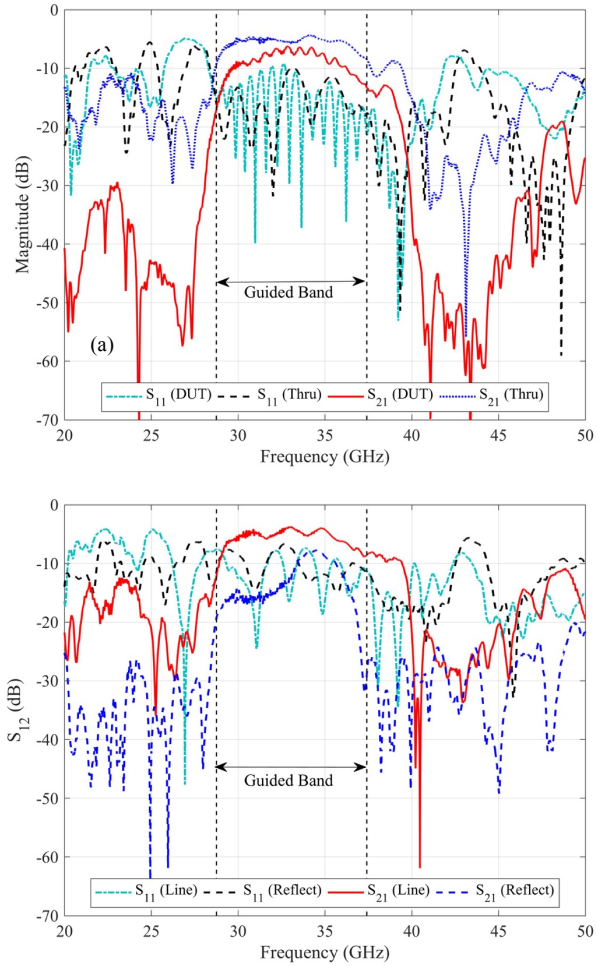

Fig. 5.11 Measured S-parameters. (a) Thru and DUT; (b) Line and reflect.

with the theoretical analysis based on the dispersion relation. The measured return losses are also about 10 dB for the thru and DUT, agreeing with the simulation results shown in Fig. 5.8. A reduction of transmission slightly above the upper bound of the guided band is observed which corresponds to the transmission gap between even mode (I) and even mode (II) as revealed by previous numerical studies. The q-factor of this transmission gap is slightly lower than the simulation results, which is probably caused by the relatively high practical transmission line loss. Compared Fig. 5.8 with Fig. 5.11, the measured S_{21} difference between the thru and DUT is much more obvious than that of the simulation results, which indicates the insertion losses of the measurement results are higher than that of the simulation results. Factors that increase the loss, such as residual air gaps between different layers, surface roughness, oxidation of copper, residual burnt dielectric powders, and fabrication errors, are not considered in the simulation, which contribute to the difference between the simulated and measured results.

The measured propagation loss of the fabricated HPCIWs, shown in Fig. 5.12, is obtained by using TRL calibration method [149]. A guided band ranging from 28.75 GHz to 37.41 GHz is observed, which corresponds to the even mode (I) shown in Fig. 5.2 and Fig. 5.3. A narrow frequency range of negative propagation loss around 32.79 GHz is observed. It is likely that this ripple is caused by the transition waveguides and photonic crystal structures were not placed at precisely the same position from one measurement to another.

An additional method comparing the maximum available gain (G_{max}) [138] of the thru and DUT was used as a reference to the TRL calibration method. It is called as the GMAX method in this chapter. The maximum available gain is defined as:

$$G_{max} = 10\log_{10}\left(\frac{1}{K+\sqrt{K^2-1}}\frac{|S_{21}|}{|S_{12}|}\right),$$

where

$$K = \frac{1-|S_{11}|^2-|S_{22}|^2+|\Delta|^2}{2|S_{21}S_{12}|},$$

and $\Delta = S_{11}S_{22} - S_{12}S_{21}$. Then, the propagation loss using GMAX method is given by

$$\alpha\ (\mathrm{dB/cm}) = \frac{G_{max}^{t}(\mathrm{dB}) - G_{max}^{d}(\mathrm{dB})}{-\Delta l\ (\mathrm{cm})},$$

where, G_{max}^{t} and G_{max}^{d} are the maximum available gains of thru and DUT, respectively, and Δl is the difference of length between them. The thru and

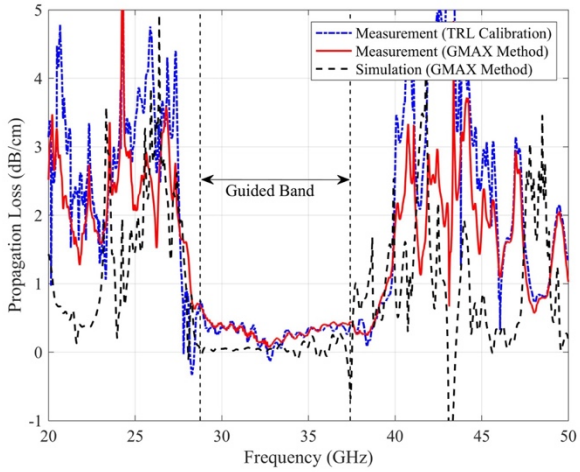

Fig. 5.12 Propagation loss of the proposed HPCIW. The simulation result outside the guided band is less accurate since it doesn't fulfill the required of multiline calibration method.

the DUT is compared intentionally because the s-parameters between them are more consistent than the line, which indicates the misplacements of components in the waveguide are smaller. It should be noted that the GMAX method used here is more accurate than the cut-back method [150] which only compares the output power of two waveguides with different length, especially when the impedance of the waveguide is not matched with the feeding network. It is because both insertion loss and return loss are considered in the GMAX method, while the cut-back method only takes into account insertion loss. The propagation loss calculated by using the GMAX method is also presented in Fig. 5.12 using the red solid curve. Good agreement between the TRL calibration method and GMAX method inside the guided band was achieved, and the negative propagation losses around 32.79 GHz are avoided with the GMAX method. From the red solid curve, It can be seen that at the lower and upper bounds of the guided band, the propagation loss is seen to increase, which agrees with the lower and upper limit of the dispersion curve of the even mode (I). The transmission window slightly above 37.41 GHz supports the propagation of the even mode (II), which is outside the guided band of interest. According to the GMAX method, the measured propagation loss of the HE_{10} mode is below 0.69 dB/cm over the frequency range from 28.75 GHz to 37.41 GHz, with a minimum loss of 0.07 dB/cm at 32.66 GHz.

In Fig. 5.12, the simulated loss calculated by using the GMAX method is also included. From 28.75 GHz to 37.41 GHz, the measured propagation losses are higher than simulated results on average. The difference in the propagation loss between the simulation and the measurement results is smaller in the centre of the guided band than that at the edge of the guided band. It is because the confinement of the wave by the photonic crystal structure is stronger in the band centre than that at the band edge, and consequently the EM wave in the band centre is less affected by the oxidized copper and defects in the cladding, resulting in a lower loss. Based on Fig. 5.5, the zero group-velocity dispersion points happens at $0.457a$, which is 33.4 GHz when $a = 4.106\ \mathrm{mm}$ in the real situation.

5.5 Concluding remarks

This chapter presents a novel hollow photonic crystal integrated waveguide (HPCIW) which combines the advantages of substrate integrated waveguide and photonic crystal waveguide. The design concept is experimentally verified at Ka-band with a good agreement with theoretical analyses. The

proposed HPCIW supports single-HE_{10}-mode propagation under even-field excitation conditions. It achieves a bandwidth of 26% centred at $0.453\,\mathrm{c/a}$, and a zero GVD point at $0.457\,\mathrm{c/a}$. The measured propagation loss of the fabricated waveguide is less than 0.69 dB/cm from 28.75 GHz to 37.41 GHz, with a minimum loss of 0.07 dB/cm at 32.66 GHz. A zero GVD point is founded at 33.4 GHz according to the dispersion relation. The design presented in this chapter can easily be scaled to other bands, such as THz and optical frequencies, by properly changing the lattice constant of the photonic crystal and choosing a suitable high permittivity host material.

Chapter 6
Octave Bandwidth Single-mode Hollow Bragg Reflector Integrated Waveguide

In this chapter, a novel hollow Bragg reflector integrated waveguide (HBRIW) is proposed, which comprises of an air-core line-defect Bragg reflector waveguide sandwiched between two parallel metal plates, as shown in Fig. 6.1. The design is similar to the previous work on hollow photonic crystal integrated waveguide (HPCIW) discussed in Chapter 5 and in the recently submitted paper [151]. However, along with some similarities, there are some differences between HBRIW and HPCIW. Firstly, they both adopt a photonic crystal structure and contain parallel metal plates, each of which confines the EM wave in horizontal and vertical directions, respectively, giving them similar advantages to PCW and SIW. For example, both HBRIW and HPCIW can be platforms for functional components and circuit design as what PCW and SIW are good at [146, 98]. Secondly, they both eliminate the drawbacks of PCW and SIW, such as the via metallization step of SIW at high frequencies and the difficulties of stacking PCW vertically for 3D compact and multilayer SiP applications. Thirdly, their operating bands are both scalable by changing the lattice constant of the photonic crystal and properly choosing the dielectric material. Fourthly, since the top and bottom metal plates can be isolated in both types of waveguides, a direct current (DC) bias can be applied to the top and bottom metal plates which helps integrate active components into the waveguide. However, due to the broad photonic bandgap, HBRIW can operate over more than a one-octave band in single-mode pattern, which is much wider than HPCIW does. Moreover, the structure of HBRIW is more flexible and smooth for creating

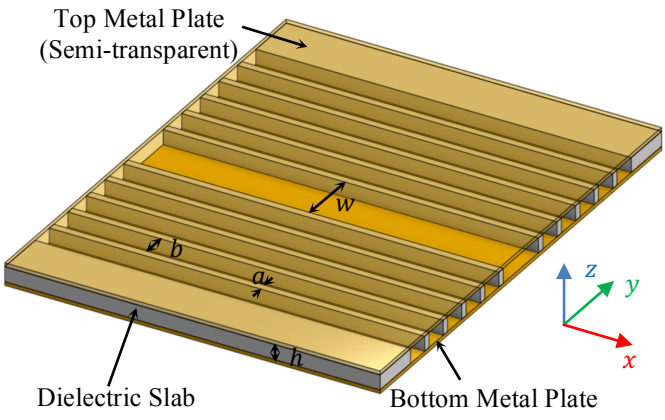

Fig. 6.1 Trimetric view of the HBRIW.

bends or tapering functional components than that of HPCIW which is restricted by the two-dimensional photonic crystal pattern. In addition, the minimum geometric feature of HBRIW can be about 4 times larger than that of HPCIW, which makes the fabrication easier.

A theoretical design of the proposed HBRIW was performed using MIT Photonic Bands (MPB) package [145] which indicated that HE_{10} mode is supported more than one octave centred at $0.464\,c/a$, and a zero group-velocity dispersion point is found at $0.536\,c/a$, where c is the speed of light and a is the lattice constant for the one-dimensional (1D) photonic crystal Bragg reflector structure. Selecting 4.28 mm as the value of a, a HBRIW operating around the Ka-band was fabricated and characterised.

6.1 Dispersion relation and guided modes

Fig. 6.1 shows the trimetric view of the proposed HBRIW with the key design parameters indicated. The top and bottom layers are a pair of parallel metal plates, and the middle layer is an air-core line-defect 1D photonic crystal Bragg reflector structure. The Bragg reflector consists of periodically alternating layers of high- and low-refractive-index materials. Air is chosen as the low-refractive-index material for its low refractive index and low loss. Another material that forms the Bragg reflector is desired to be high refractive index and low loss, to create a large photonic bandgap and reduce the material absorption loss. Considering the available fabrication techniques, Rogers RO3010™ material, whose design Dk (dielectric constant) is 11.2 from 8 to 40 GHz and loss tangent is 0.0022 at 10 GHz, was chosen as the high-refractive-index material. The fundamental mode of the proposed HBRIW is a vertically polarized HE_{10} mode. Like HPCIW [151], the height of the HBRIW, h, is adjustable, but it will slightly affect the performance, and will introduce high order modes if the value of is too large [147]. In this chapter, a HBRIW with a thin dielectric slab, namely, $h < w/2$, is considered. Since the electric field of the HE_{10} mode is uniform along the z-axis, h does not contribute to the dispersion relation. Therefore, the dispersion relation problem can be simplified into a 2D problem in the x-y plane assuming the third dimension is infinite and uniform, and it represents the eigenvalues for the vertically (z-axis) linearly polarized modes confined in the air core of the Bragg reflector waveguide.

As shown in Fig. 6.1, the thicknesses of the high- and low-refractive-index materials are a and b, respectively, and $\Lambda = a + b$ is the period constant of the 1d photonic crystal structure. To maximize the first-order photonic

bandgap, a and b are chosen based on the following quarter-wavelength condition [152]:

$$n_a a = n_b b = \frac{\lambda_c}{4} \tag{6.1}$$

where n_a and n_b are the refractive index of the high- and low-refractive-index materials, and λ_c is the center wavelength of the first-order bandgap when the longitudinal propagation constant $\beta = 0$. As it can be seen from Eqn. (6.1) that, by properly choosing a target operating wavelength (λ_c) and the materials for the high- and low-refractive-index layers, the geometric parameters of the Bragg reflector structure can change accordingly and the operating band can thereby be scaled to the target operating wavelength. In this design, $n_a = \sqrt{11.2} = 3.35$ and $n_b = 1$, so $a = \frac{n_b}{n_a+n_b}\Lambda = 0.23\Lambda$ and $n_b = \frac{n_a}{n_a+n_b}\Lambda = 0.77\Lambda$. The width of the line defect in the middle of the Bragg reflector waveguide, w, greatly affects the dispersion curves of the defects modes, but it barely affects the dispersion curves of the cladding modes. The value of w should be carefully chosen to push the dispersion curve of the competing second order odd mode to the edge of the photonic bandgap efficiently preventing the propagation of the odd mode in the HBRIW. This

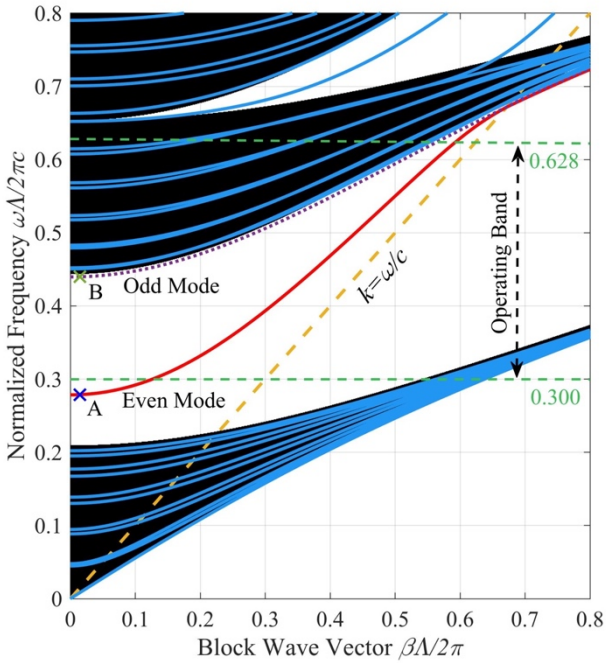

Fig. 6.2 Bandgap diagram and dispersion curves for the vertically polarized modes in the line-defect Bragg reflector waveguide. The orange dashed line is the light line. The green dashed lines indicate the operating band which is wider than one octave. The black region is the bandpass region for the 1D photonic crystal where the EM wave can pass through the periodic structure and leak out. The white region above the light line is the bandgap.

effect is known as the modal-filtering effect [127].

The dispersion curves for vertically (z-axis) linearly polarized modes in the line-defect Bragg reflector waveguide overlaid upon the bandgap diagram is shown in Fig. 6.2. The dispersion curves were numerically calculated by using the MPB package. The photonic bandgap obeys the following condition which gives the constraint that stops the EM wave from propagating through into the periodic claddings from the line defect [118]:

$$|\mathrm{Re}(X_s)| < 1 \qquad (6.2)$$

where

$$X_s = \left[cos(k_b b) - \frac{i}{2}\left(\frac{\xi_b k_b}{\xi_a k_a} + \frac{\xi_a k_a}{\xi_b k_b}\right) sin\,(k_b b)\right] exp\,(-ik_a a) \qquad (6.3)$$

and $k_i = \sqrt{(n_i k_0)^2 - \beta^2}\ (i = a, b)$ is the lateral propagation constant; $k_0 = \omega/c$ is the vacuum wavenumber; β is the longitudinal propagation constant; $n_{eff} = \beta/k_0$ is the effective refractive index of the mode; ω is the vacuum angular frequency; c is the speed of light in vacuum; and ξ_i is 1 or $1/n_i^2\ (i = a, b)$ corresponding to $S = \mathrm{TE}$ or TM modes, respectively.

In Fig. 6.2, the dispersion curves in the bandgap region are guided defect modes, such as the red curve which corresponds to the desired fundamental even mode. The blue curves that lie in the black region are cladding modes or lossy defect modes. The purple dotted line lying at the edge of the photonic bandgap corresponding to a lossy odd mode. The even and odd modes here correspond to the symmetric and antisymmetric modes regarding the x- z plane. The mode pattern of point A, for the fundamental even mode, and point ,B for the lossy odd mode, in Fig. 6.2 are shown in

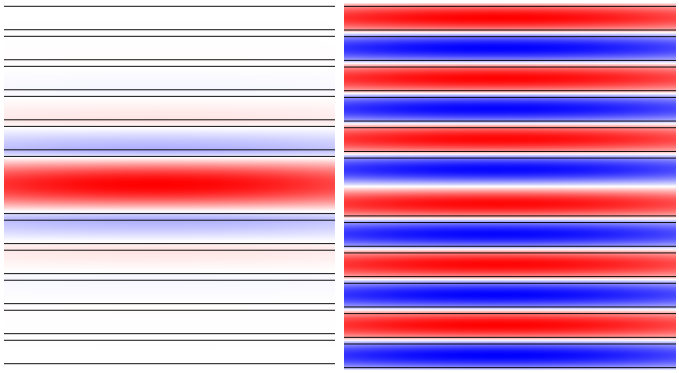

(a) Even mode (b) Odd mode

Fig. 6.3 Mode pattern for points A and B in Fig. 6.2. (a) Point A. $(k_n, \omega_n) = (0.015, 0.2788)$; (b) Point B. $(k_n, \omega_n) = (0.015, 0.4399)$. Here, $k_n = k\Lambda/2\pi$ and $\omega_n = \omega\Lambda/2\pi c$. Periodic boundaries are applied.

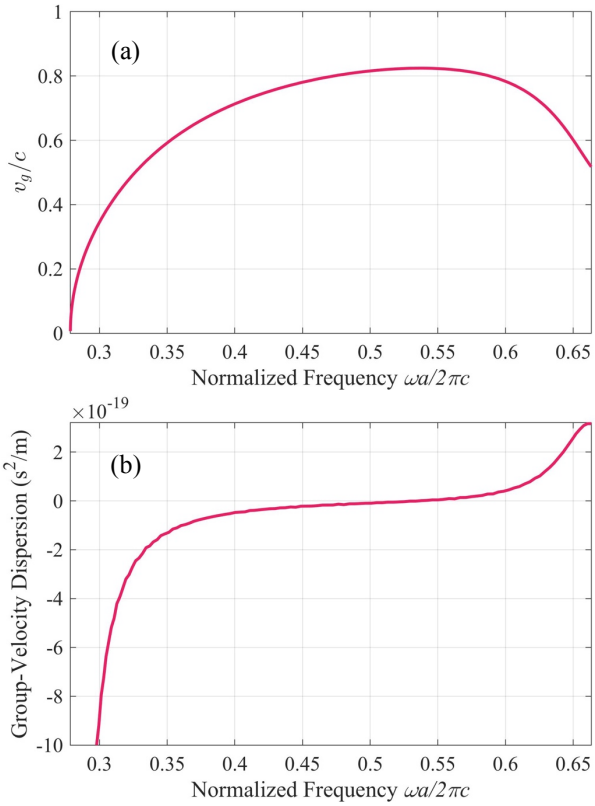

Fig. 6.4 (a) Normalized group velocity and (b) group-velocity dispersion.

Fig. 6.3. As it can be seen, only the desired fundamental even mode can be tightly confined in the line defect region, while the odd mode lying at the edge of the photonic bandgap is very lossy. The phenomenon has previously been observed in Bragg fibre [130]. Therefore, by properly coupling in to the even mode of the HBRIW, and not the odd mode, the waveguide can operate in single-mode pattern [17]. The frequency range between the two horizontal green dashed lines in Fig. 6.2 gives the operating band of this design. The parts of the dispersion curve for the even mode below the lower dashed line ($\omega_n^l = 0.300$) and above the upper dashed line ($\omega_n^h = 0.628$) are not selected as operating bands since in these frequencies, the guided mode can be relatively lossy and could potentially couple into the unwanted cladding modes. The selected operating band gives a ratio bandwidth of $\omega_n^h/\omega_n^l = 2.09$, which is wider than one octave.

The group velocity and GVD of the fundamental even mode is plotted with respect to normalized frequency in Fig. 6.4. The GVD is defined as $\partial^2 k/\partial\omega^2$. Fig. 6.4 (a) shows that as the frequency increases, the group velocity first increases and then decreases, and the turning point happens to be at $0.536c/a$ where the zero GVD occurs, as seen in Fig. 6.4 (b).

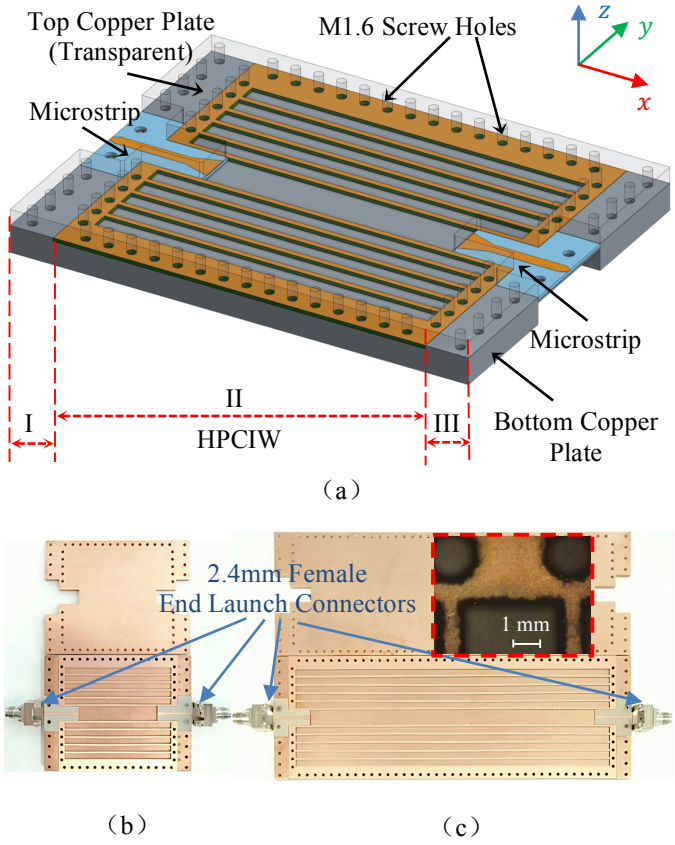

Fig. 6.5 CAD design and fabricated samples (before assembling) of the HBRIW. (a) CAD design. The HBRIW in region II is fed by microstrips in regions I and III. (b) Short HBRIW with the length between the two microstrip lines $l = 46.54\ \mathrm{mm}$. (c) Long HBRIW with $l = 150.56\ \mathrm{mm}$. The inserted picture in (c) shows the backside view of the Bragg reflector structure.

The design presented here is scalable. One can achieve this by changing the lattice constant of the Bragg reflector and properly choosing a combination of high- and low-refractive index material with low loss which suits the target frequency band. In the next section, a design around Ka-band by choosing Rogers RO3010™ and air as the high- and low-refractive-index materials and setting $\Lambda = 4.28\ \mathrm{mm}$ wil lbe demonstrated.

6.2 Fabrication and simulation

The fabrication process is similar to that of a HPCIW and has been stated in the last chapter of the submitted paper [151]. The fundamental even mode in Fig. 6.3(a) becomes a HE_{10} mode in the full 3D structure presented in Fig. 6.1. Fig. 6.5(a) shows the CAD design of the HBRIW. The colours do not reflect the actual colours of the materials and are selected to distinguish different sections. A microstrip line, whose even quasi-TEM field pattern is basically matched with the polarization of the HE_{10} mode, is used to couple

the signal into the HBRIW. Fig. 6.5(b) and Fig. 6.5(c) show the fabricated samples of the HBRIW before final assembly. Here, the width of the line defect $w = 8.14\,\mathrm{mm}$, and the thicknesses of the high- and low-refractive index layers are $a = 1\,\mathrm{mm}$ and $b = 3.28\,\mathrm{mm}$, respectively. As shown in the figures, 2.4 mm female end launch connectors obtained from Southwest Microwave Inc. are used to connect to the microstrip lines and then 2.4 mm coaxial cables go to the VNA. The input and output ends of the microstrip line are designed to fit the dimensions of the end launch connector and match the impedance of the HBRIW, respectively. Therefore, the microstrip line is tapered at both ends. To reduce the signal reflection between the microstrip line and the HBRIW with air as the material of the core region, a PCB board with low permittivity is preferable as the substrate for the microstrip line. Thus, the Rogers RT/duroid® 5880LZ™, whose dielectric constant is 2.00 between 8 and 40 GHz and loss tangent is 0.0021 at 10 GHz, is chosen. As above-mentioned, the material for the high-refractive index layer of the Bragg reflector is double-side cladded Rogers RO3010™. The dielectric thickness and copper cladding thicknesses (both sides) for both RT/duroid® 5880LZ™ and RO3010™ boards are 0.635 mm and 17.5 μm, respectively.

Both the microstrip feeds and the photonic crystal structures were fabricated using LPKF ProtoLaser U3. The fabrication was sufficiently precise, but the walls of the Bragg reflector were slightly burnt by the laser and a very small amount of burnt dielectric material was left surrounding the bottom edge of the removed part, as shown by the insert in Fig. 6.5(c). Since cleaning the residual burnt dielectric materials manually would probably cause unintended bends or damage to the structure, the residual burnt materials were left there. The copper claddings of the RO3010™ were not removed from the dielectric to provide extra mechanical support for the delicate Bragg reflector structure. The copper claddings are not originally designed in the HBRIW. However, since the thickness is only about 2.7% of the dielectric thickness and much smaller than the free-space wavelength over the operating band, the residual copper claddings have negligible impact on the dispersion relation and only very slightly increase the overall loss according to additional simulations. The top and bottom copper plates are made of C101 copper. They were first fabricated by using a DMU 40 CNC milling machine and then manually polished by using 500 grade wet and dry silicon carbide. The surface finish of the top plates is smooth since it does not require CNC processing, but the surface finish of the bottom plates is relatively rough owing to the tool marks caused by the CNC processing

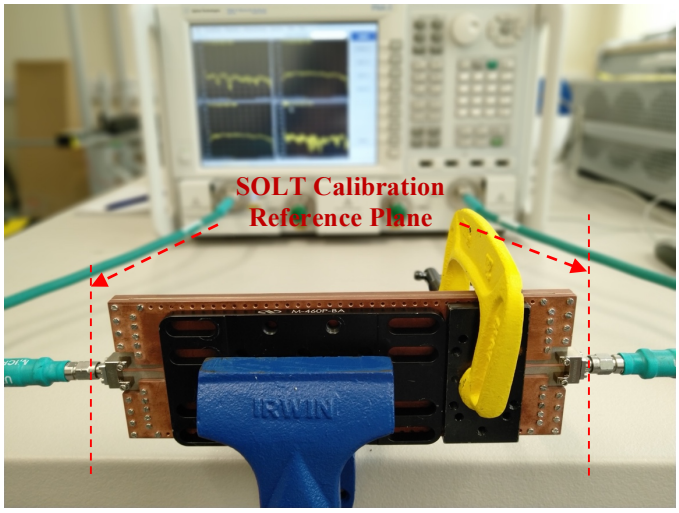

Fig. 6.6 Measurement Setup. SOLT calibration is applied to shift the reference plane to the end of the 2.4 mm coaxial cables. Clamps are used to squeeze out the air gaps between the metal plates and the photonic crystal layer as much as possible. The M1.6 nuts and bolts at both sides of the HBRIW are removed during the measurement to prevent them from reflecting the outgoing wave.

which is used to create a concave space to place the Bragg reflectors and microstrip lines.

6.3 Results

Fig. 6.6 shows the measurement setup. A SOLT calibration was performed using a 2.4mm mechanical calibration kit to place the reference planes to the end of the coaxial cables. The measurement and simulation results of the short and long HBRIWs shown in Fig. 6.5 are presented in Fig. 6.7. In the simulation, a simplified 50Ω coaxial connector, mimicking the actual end launch connector, was used to feed the signal to the microstrip line. The return losses of both the measured and simulated results are around 10 dB indicating that most of the power is coupled into the HBRIW. The measured difference of the insertion loss between the two HBRIWs is larger than the simulated one, which indicates a higher loss than the theoretical expectation. Factors that contribute to the additional loss in practice, such as residual air gaps between different layers, surface roughness, oxidation of copper, residual burnt dielectric powders, and fabrication errors, are not considered in the simulation, resulting in the difference between the simulated and measured results. The electric field pattern of the long HBRIW at 33 GHz is shown in Fig. 6.8. The EM wave is interfered at the junction between the microstrip line and the HBRIW where the EM field is not matched exactly causing impedance mismatch. However, the distorted field caused by the

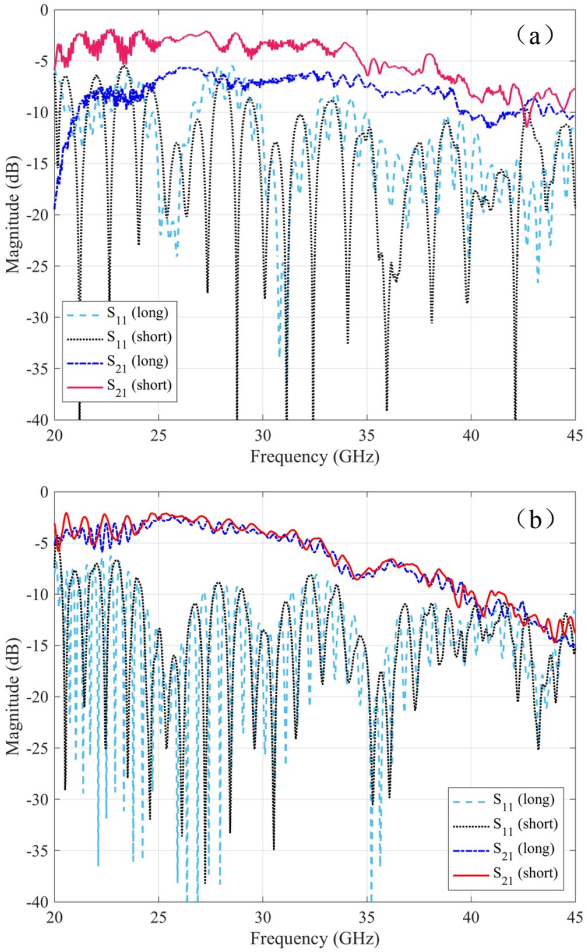

Fig. 6.7 (a) Measured and (b) simulated results of the HBRIWs shown in Fig. 5. The simulation is performed with CST time-domain solver.

interference is gradually dissipated along the waveguide. The desired HE_{10} mode is seen to be tightly confined in the air core demonstrating the HBRIW as a single-mode waveguide. Additional, from Fig. 6.1, It can be seen that the top and bottom metal plates of the HBRIW are not electrically connected, which means these metal plates can be electrodes by applying a DC voltage between them allowing for the integration of active components in the HBRIW. This application has been verified by a simplified simulation using a microstrip line to feed the ideal structure show in Fig. 6.1, which gives consistent results as presented in Fig. 6.7.

The measuerd and simulated propagation loss of the fabricated HBRIWs, shown Fig. 6.9, is obtained by comparing the maximum available gain (G_{max}) of short and long HBRIWs, which is the same GMAX method used in Chapter 5 to characterise the HPCIW. From Fig. 6.9, the measured propagation loss is observed to be higher than the simulated one, with factors that increase the loss, such as surface roughness, oxidation of

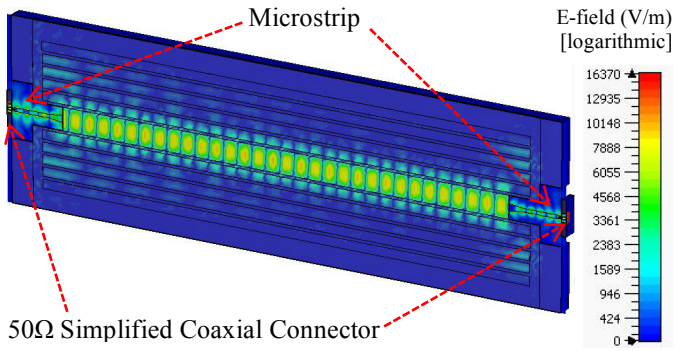

Fig. 6.8 Electric field of the long HPCIW in log scale at 33 GHz. Two 50Ω simplified coaxial connectors are applied to feed the microstrips.

copper, residual burnt dielectric material, and fabrication errors, that are not considered in the simulation. The difference between the measured and simulated loss is larger at low frequencies than that at high frequencies. It is due to the ability of confinement of the Bragg reflector being a frequency-dependent factor, and it is relatively weak when the effective refractive index (n_{eff}) of the mode is small [130]. From the measurement results, a narrow frequency range with negative propagation loss around 42.7 GHz is observed. It is likely because of an unwanted defect in the microstructured claddings of the short HBRIW being introduced during the fabrication which resonates at around 42.7 GHz, since there is a deep reduction of the transmission window around 42.7 GHz in the measured S_{21} spectrum of the short HBRIW, while the long HBRIW does not have such a reduced transmission window around this frequency.

From the measurement results shown in Fig. 6.9, a wide operating band is observed ranging from 21 to 44 GHz, and the propagation loss over this frequency range is less than 0.78 dB/cm. In addition to this, according to Fig. 6.4, the zero GVD point happens at $0.536c/a$, which is 39.4 GHz when $a = 4.28\ \mathrm{mm}$ in the real situation.

6.4 Concluding remarks

This chapter presents a novel hollow Bragg reflector integrated waveguide (HBRIW) which can operate in single-HE_{10}-mode over an octave bandwidth with zero GVD at $0.536c/a$. The proposed HBRIW is experimentally demonstrated around Ka-band which is constant with theoretical analysis and EM simulation. The fabricated waveguide loss has been characterised to be less than 0.78 dB/cm over the frequency range from 21 to 44 GHz. A zero GVD point is founded at 39.4 GHz based on the dispersion curve. The design concept here can easily be scaled to other band, such as THz and

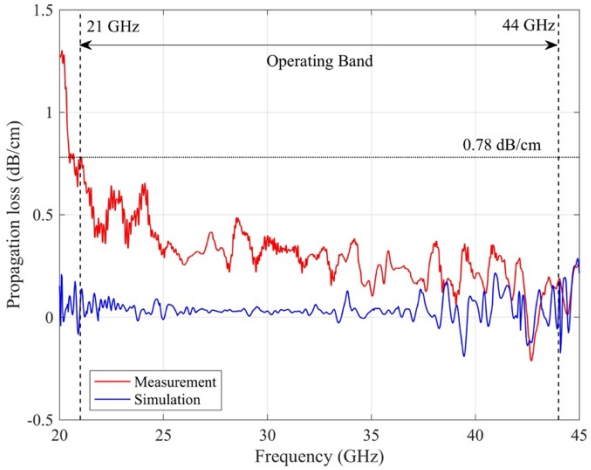

Fig. 6.9 The measured and simulated propagation loss of the proposed HPCIW.

optical frequencies. Showing many advantages over SIW and photonic crystal waveguide, HBRIW can be a promising candidate for multilayer mmW and THz SiP applications.

Chapter 7
Functional Components

PCW and SIW are well-known platforms for functional components, such as antennas [153, 154], cavities [155 - 157], splitters [158, 159], combiners [160], diplexers [161], directional couplers [162], filters [163 - 167], modulators [168, 169], polarization converters [170], switches [171], sensors [172], receivers [173], and lasers [174 - 178]. In this chapter, various functional components built upon the photonic crystal fibres or waveguides proposed in this thesis, including cavities, bends, splitters, and antennas, are investigated, demonstrating the potential for photonic-crystal-based waveguide to be used in a number of important applications, such as photonic integrated circuits and microfluidic sensors.

7.1 Waveguide Bends

Waveguides bends are essential components for integrated circuits. In this

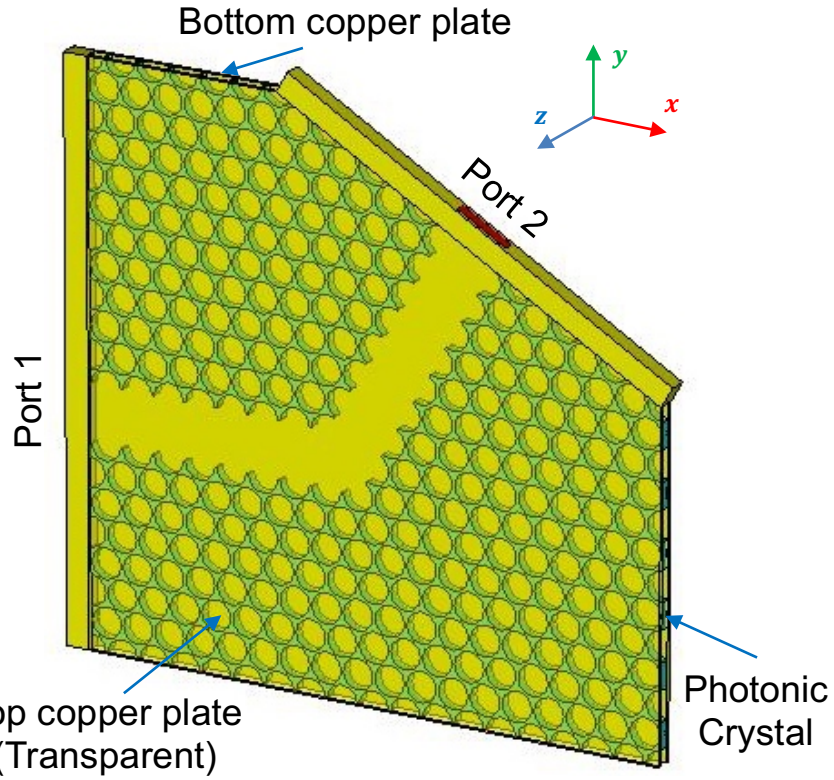

Fig. 7.1 Perspective view of the 60° waveguide bend based on HPCIW. The key geometric and material properties of the waveguide bend are the same as that of the HPCIW shown in Fig. 5.7.

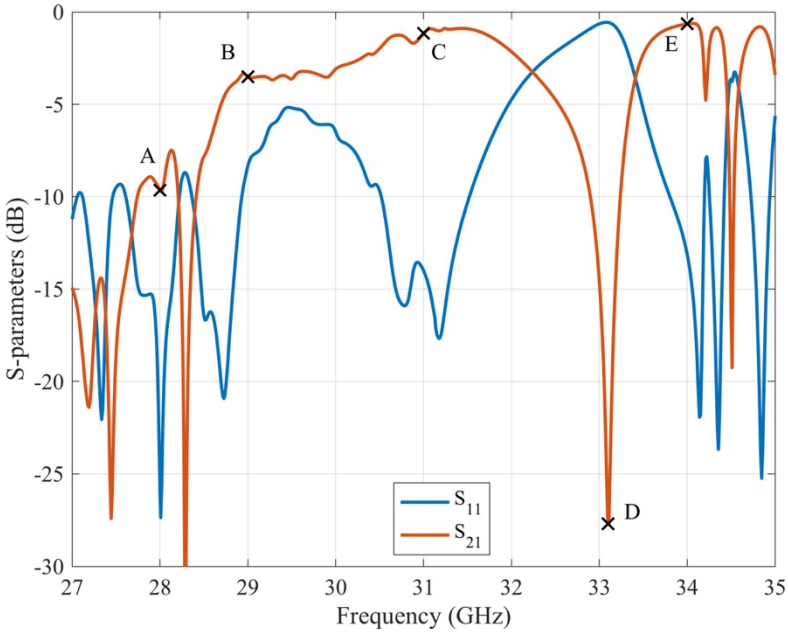

Fig. 7.2 Simulated S-parameters vs Frequency of points A to E corresponding to 28 GHz, 29 GHz, 31 GHz, 33.1 GHz, and 34 GHz, respectively

section, two types of waveguide bends are discussed, which are built upon the fabricated HPCIW and HBRIW proposed in Chapters 5 and 6.

7.1.1 HPCIW 60° waveguide bend

The perspective view of the 60° waveguide bend based on HPCIW is shown in Fig. 7.1. The key geometric and material properties of the waveguide bend are the same as that of the HPCIW discussed in Chapter 5, except the height of the dielectric layer is $h = 1.27\,\mathrm{mm}$, rather than previously $h = 0.635\,\mathrm{mm}$. The change does not affect the dispersion of the guided HE_{10} mode which is uniform along the z-direction. The waveguide bend is fed by rectangular waveguides with same aperture size as that of the line-defect air core of the HPCIW.

The simulated S-parameters are shown in Fig. 7.2. The HPCIW, as discussed in Chapter 5, operates from 28.75 to 37.41 GHz. However, due to the presence of a defect at the junction, the operating band of the waveguide bend is significantly reduced. The normalized electric field at several representative frequency points are shown in Fig. 7.3. The EM field at point A is leaky because it is outside the photonic bandgap of the waveguide. At points B and C, the EM fields are better confined in the line-defect region, since they are inside the photonic bandgap, but a small amount of EM field still penetrates into the bulk photonic crystal structure due to the presence of a defect at the junction. At point D, a standing wave is formed between the

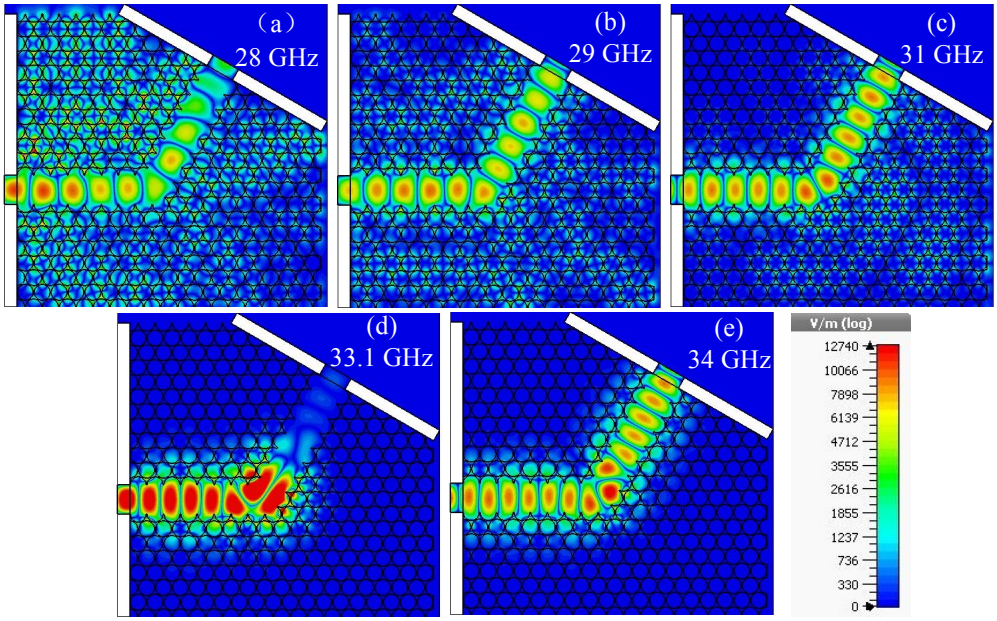

Fig. 7.3 Normalized electric field at points A to E shown in Fig. 7.2.

port 1 and the junction which stops the EM field being guided to the port 2, and hence the transmission at point D is very low. It is probably caused by a defect mode at the junction which resonates at 33.1 GHz. At point E, a high transmission is found. The operating band is significantly reduced by defects mode like the one at point D. Nonetheless, the waveguide bend still supports a transmission window ranging between 28.7 GHz and 32.5 GHz.

7.1.1 HBRIW 90° waveguide bend

The perspective view of the 90° waveguide curved bend based on HBRIW is shown in Fig. 7.4. The key geometric and material properties of the

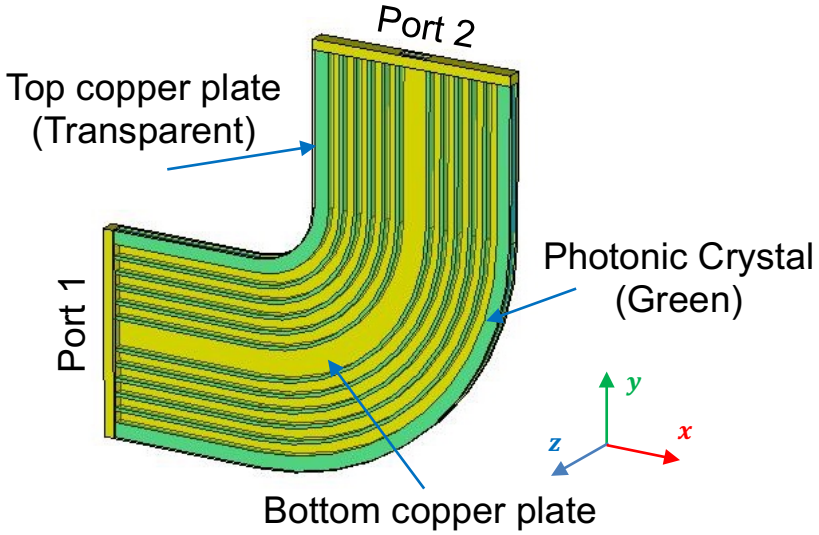

Fig. 7.4 Perspective view of the 90° waveguide curved bend based on HBRIW. The key geometric and material properties of the waveguide bend are the same as that of the HBRIW shown in Fig. 6.5.

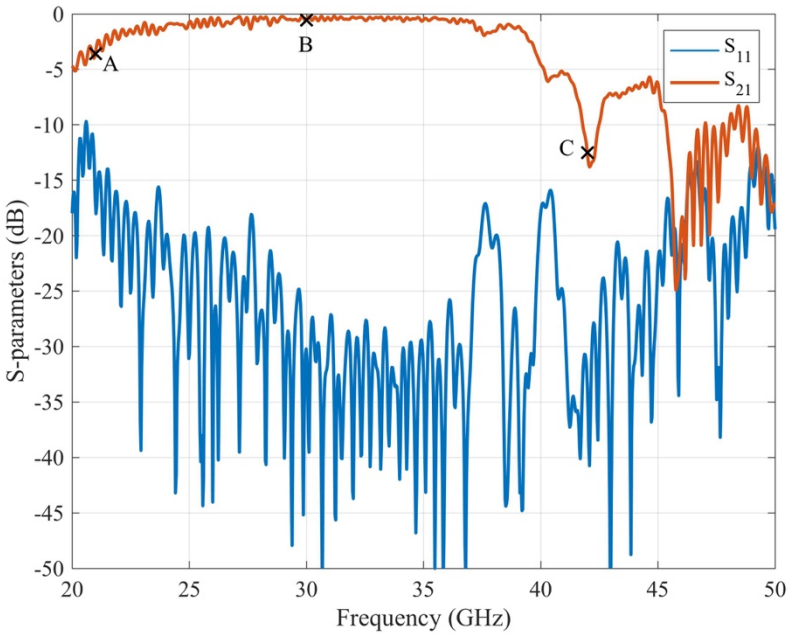

Fig. 7.5 Simulated S-parameters vs Frequency of points A to C corresponding to 21 GHz, 30 GHz, and 42 GHz, respectively.

waveguide bend are the same as that of the HBRIW discussed in Chapter 6, except the height of the dielectric layer is $h = 1.27\ \mathrm{mm}$, rather than previously $h = 0.635\ \mathrm{mm}$. The change does not affect the dispersion of the guided HE_{10} mode which is uniform along the z-direction. The waveguide bend is fed by rectangular waveguides with same aperture size as that of the line-defect air core of the HBRIW.

The simulated S-parameters are shown in Fig. 7.5. The HBRIW, as discussed in Chapter 6, operates from 21 to 44 GHz. However, due to the presence of the curved structure at the junction, the operating band of the waveguide curved bend is slightly reduced. The normalized electric field at points A, B, and C in Fig. 7.5 are shown in Fig. 7.6. The EM field at point A is leaky since the point A is located at the low end of the guided band of HBRIW, but most of the field is still guided in the waveguide. At point B, the EM field is very well confined in the line-defect air core, resulting in a large

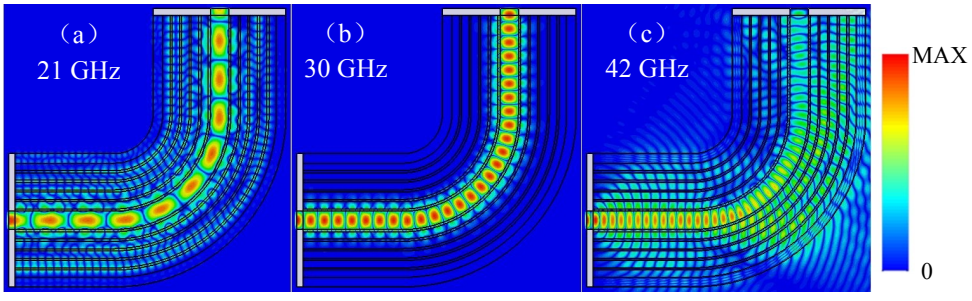

Fig. 7.6 Normalized electric field at points A to C shown in Fig. 7.5.

transmission coefficient. At point C, the EM cannot be confined in the waveguide and radiates out. Overall, from Fig. 7.5, it can be seen that the 90° waveguide bend using HBRIW supports a wide operating band ranging from 21 to 40 GHz.

7.2 Splitters

The perspective view of a splitter using HPCIW is shown in Fig. 7.7. The splitter is sandwiched by metal plates in +z and –z boundaries, which however is hidden in the figure. The geometrical and material properties are the same as that of the HPCIW discussed in Chapter 5, except that the radius of the air holes is $r_c = 0.44a$, rather than $r_c = 0.467a$. It is designed to shift the dispersion curve of the odd mode outside the operating band, which would potentially be excited due to the defect at the junction of the splitter shown in Fig. 7.7. The dispersion curve of the line defect HPCIW now calculated using the MPB package is shown in Fig. 7.8. Taking into account $a = 4.106\ \mathrm{mm}$, the even mode shown in Fig. 7.8 is supported by the HPCIW over the operating frequency range from $0.363c/a$ to $0.437c/a$, or 26.5 GHz to 31.9 GHz.

The structured shown in Fig. 7.7 is simulated using CST time domain solver.

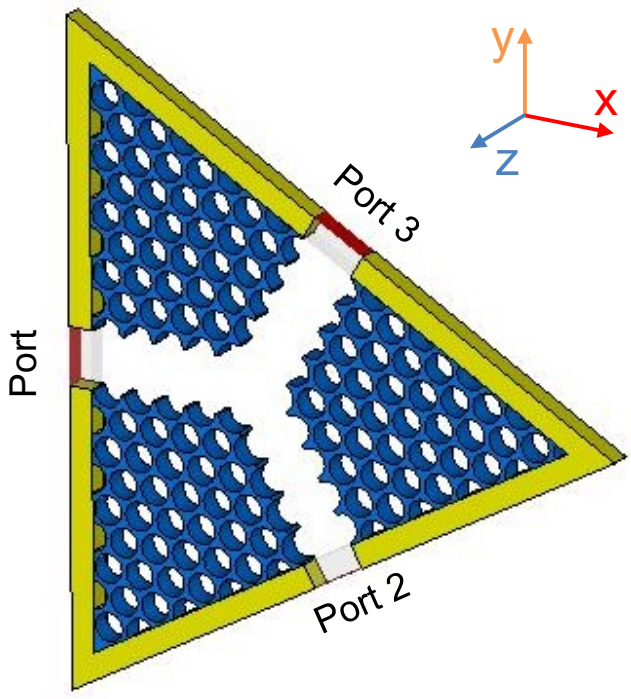

Fig. 7.7 Perspective view of the splitter. The key geometric and material properties of the splitter are the same as that of the HPCIW shown in Fig. 5.7. The top and bottom copper plates that cover the whole structure are not shown for better view.

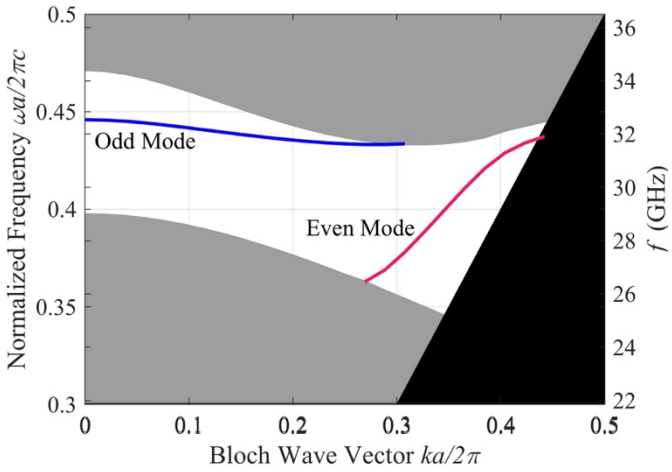

Fig. 7.8 Dispersion curves overlaid upon the photonic bandgap diagram. The second y-axis on the right corresponds to the structure with $\boldsymbol{a = 4.106\ mm}$.

The +z and –z boundaries are set as conductive boundaries using the conductivity of annealed copper (5.80×10^7 S/m). The simulated s-parameters can be found in Fig. 7.9, which shows a transmission window from 26.5 GHz to 31.9 GHz, which agrees with the dispersion curve shown in Fig. 7.8. However, at several frequencies within the window, the transmission is reduced. This is investigated by plotting the normalized electric fields at several representative frequency points, namely points A to F shown in Fig. 7.9, which are shown in Fig. 7.10.

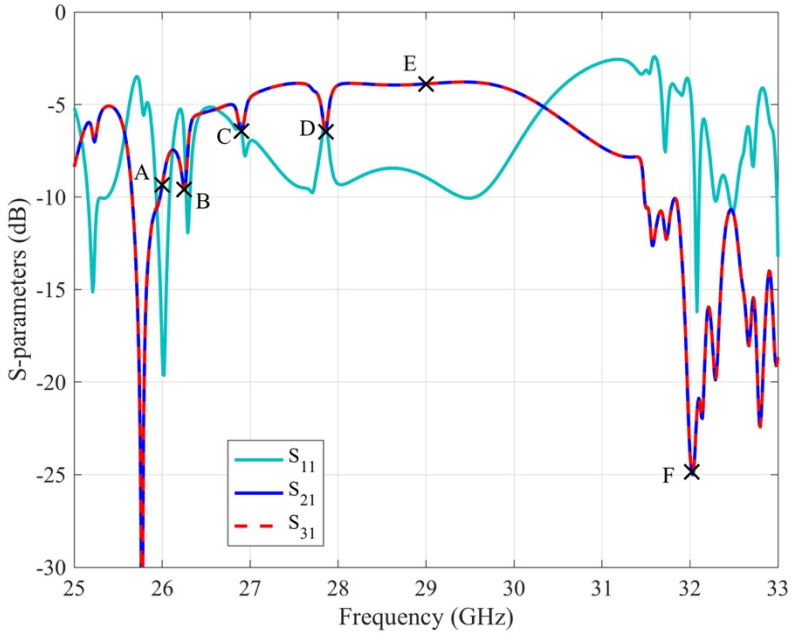

Fig. 7.9 Simulated S-parameters vs Frequency for splitter. Points A to F correspond to 26 GHz, 26.25 GHz, 26.91 GHz, 27.86 GHz, 29 GHz, and 32.02 GHz, respectively

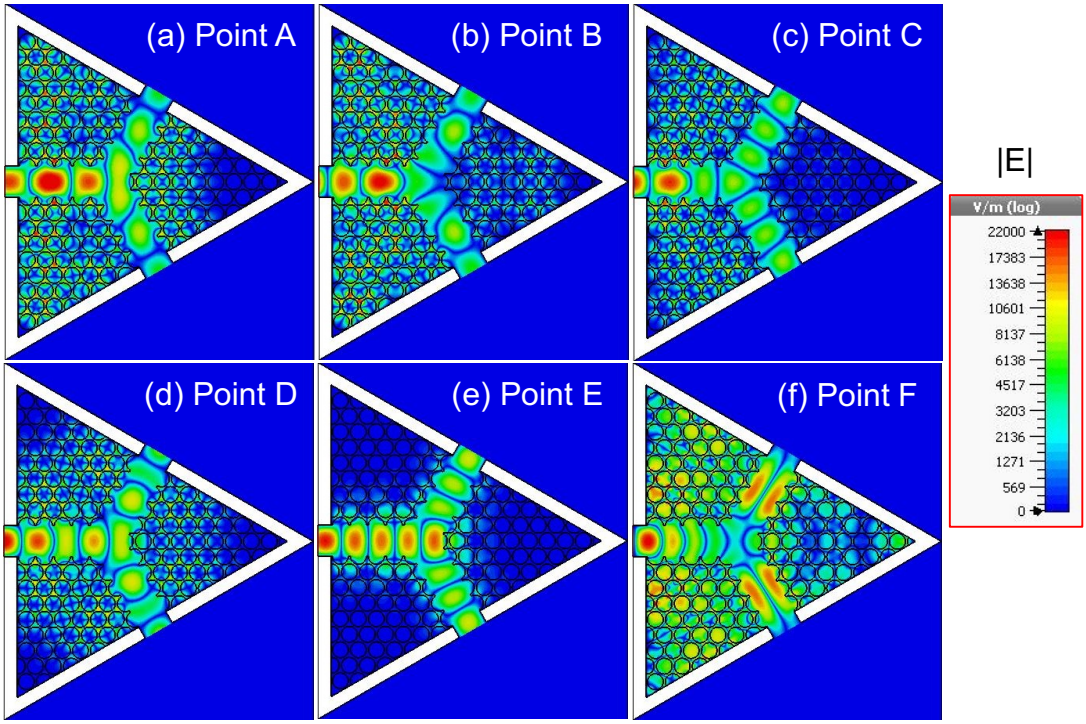

Fig. 7.10 Normalized electric field at points A to F shown in Fig. 7.9.

Comparing Fig. 7.8 and Fig. 7.9, points A and B are below the lowest guided frequency of the even mode. Thus, they are the outside the photonic bandgap and lossy, as shown in Fig. 7.10(a) and Fig. 7.10(b). Points C and D are within the guided band of the even mode, but the guided line-defect even mode is coupled with cladding modes distributed in the bulk photonic crystal structures at these frequencies, and this reduces the transmission coefficient, as shown in Fig. 7.10(c) and Fig. 7.10(d). As shown in Fig. 7.10(e), the normalized electric field is tightly confined in the line-defect air core region, resulting a good transmission property. Fig. 7.10(f) shows the polarization transformation of the EM field from the even mode to the odd mode between the input port (port 1) and the output ports (port 2 and port 3), indicating that the odd mode would potentially be excited at the junction of the splitter. Owing to above-mentioned phenomena, the operating bandwidth of the splitter is decreased to from 28 to 30 GHz.

Between 28 GHz and 30 GHz, the transmission coefficients (S_{21} and S_{31}) of the splitter are greater than -4.27 dB, and the reflection coefficient (S_{11}) is below -7.50 dB. Factors like Ohmic loss, dielectric absorption loss, and confinement loss are counted for the overall loss of the splitter.

7.3 Cavities

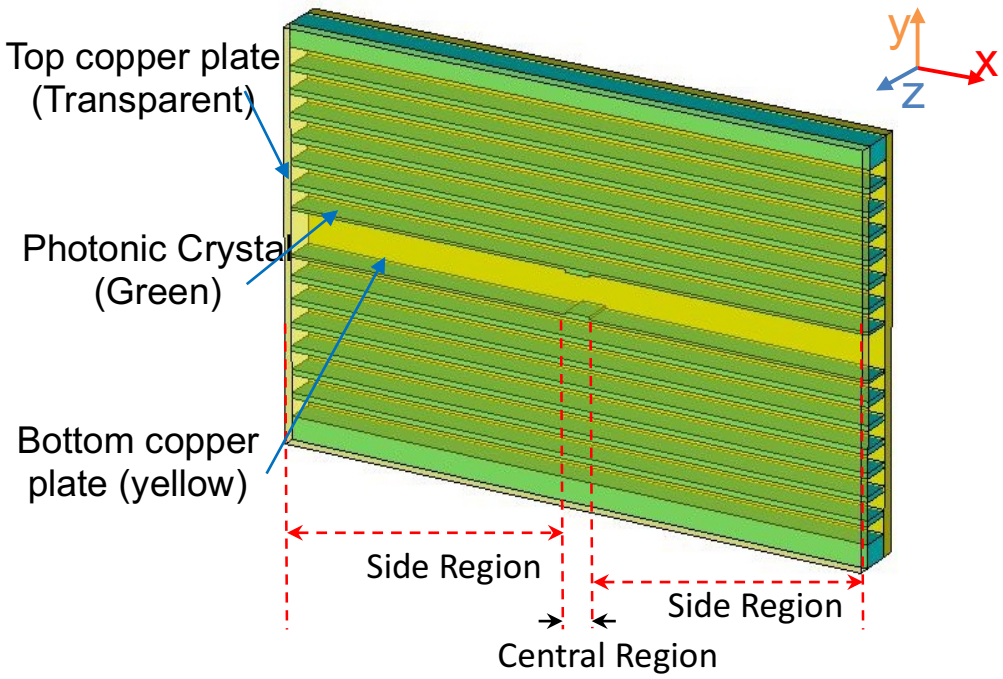

Fig. 7.11 Perspective view of the cavity.

The perspective view of the proposed cavity can be found in Fig. 7.11. The key geometric and material properties of the cavity are the same as that of the HBRIW presented in Chapter 6, except the following factors: 1) the height of the dielectric layer is $h = 1.27\,\mathrm{mm}$; 2) the thickness of the first layers away from the line-defect core at the side regions is $a/2$, while the

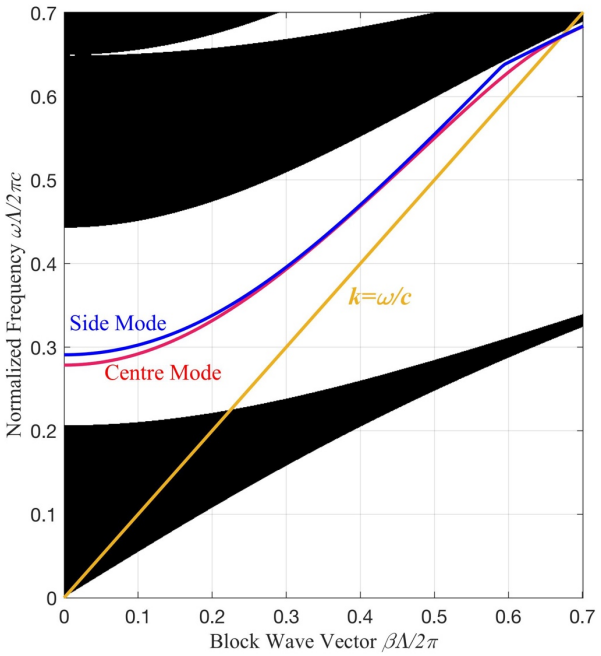

Fig. 7.12 Dispersion curves for the modes that are guided in the central and side regions, overlaid on the photonic bandgap diagram.

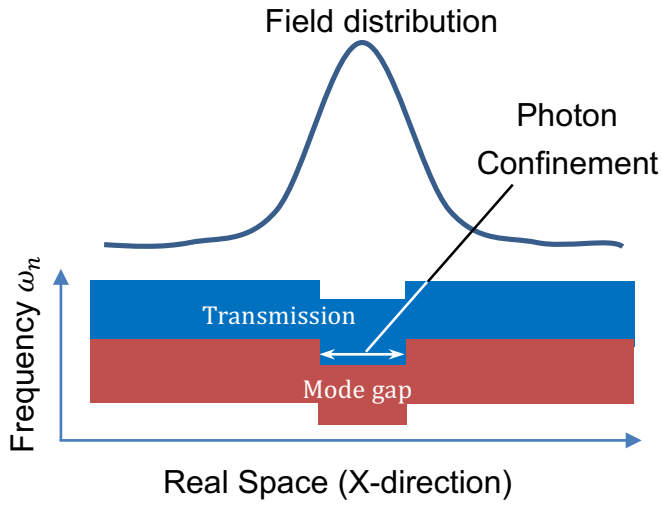

Fig. 7.13 Mechanism of photon confinement in the cavity.

thickness of the first layers at the central region remain the same as a. The dispersion curves of the line-defect mode supported in the central region and the side region overlaid upon the photonic bandgap diagram is shown in Fig. 7.12. It can be seen that in the frequency range of $0.2785 < \omega_n < 0.2909$, or $19.5\ \mathrm{GHz} < f < 20.4\ \mathrm{GHz}$ when $a = 4.28\ \mathrm{mm}$, the defect mode can only exist in the central region, not in the side regions. The photon confinement mechanism has been previously been used in photonic crystal slab waveguide [179], but it is the first time it is used in the HBRIW structure. Similar to the situation for electrons in a quantum well, the photon in the cavity is trapped in the central region, as shown in Fig. 7.13.

The structure shown in Fig. 7.11 was simulated using the CST eigenmode solver. A cavity mode is found at 21.99 GHz, as shown in Fig. 7.14. The resonant frequency is slightly higher than the frequency range shown in Fig. 7.12. It is because that the cavity mode is weakly confined in the x direction,

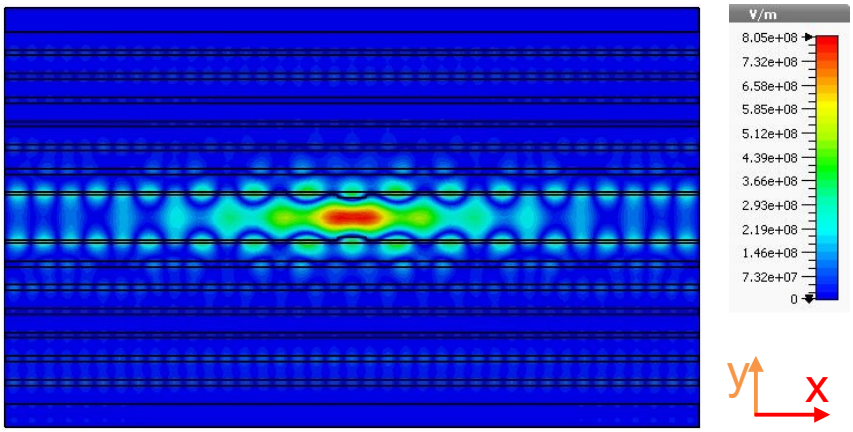

Fig. 7.14 Normalized electric field of the cavity mode resonating at 21.99 GHz.

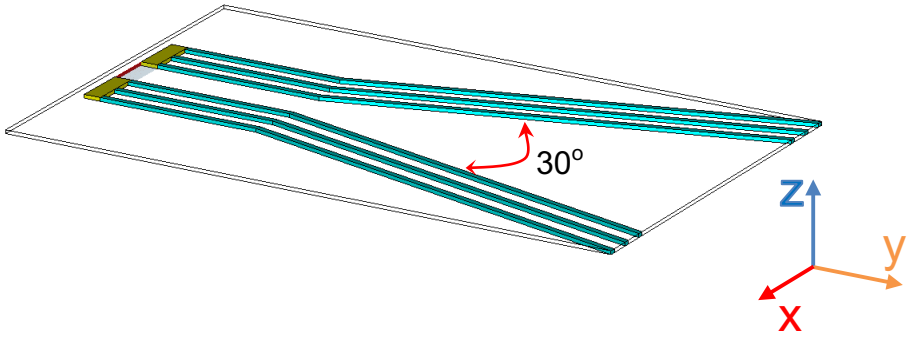

Fig. 7.15 Perspective view of the HBRIW-based h-plane horn antenna. The top and bottom boundary are set to be conductive boundaries using the conductivity of copper (5.8×10^7 S/m), so the structure is actually covered by metal in both sides in the z-direction.

which also contributes to the eigenmode frequency, while in Fig. 7.12, only the confinement in the Y-direction is considered. The unloaded q-factor of the cavity mode shown in Fig. 7.14 is calculated to be 595.72 using the CST eigenmode solver, which can potentially be improved by modifying the width of thickness of the first layers at the side regions and make the geometric transition between the central region and the side regions more smooth.

In summary, in this section, a novel cavity based on HBRIW is proposed. The mechanism for photon confinement in the cavity is similar to the electrons in a quantum well. The cavity is resonant at 21.99 GHz with a unloaded q-factor of 595.72. It can potentially be used in many functional components, like filters, sensors, diplexers, etc.

7.4 HBRIW H-plane horn antenna

The perspective view of the HBRIW H-plane horn antenna is shown in Fig. 7.15. Conductive boundaries are applied at the +z and –z boundaries to represent the parallel copper plates, which are not shown in the figure. The

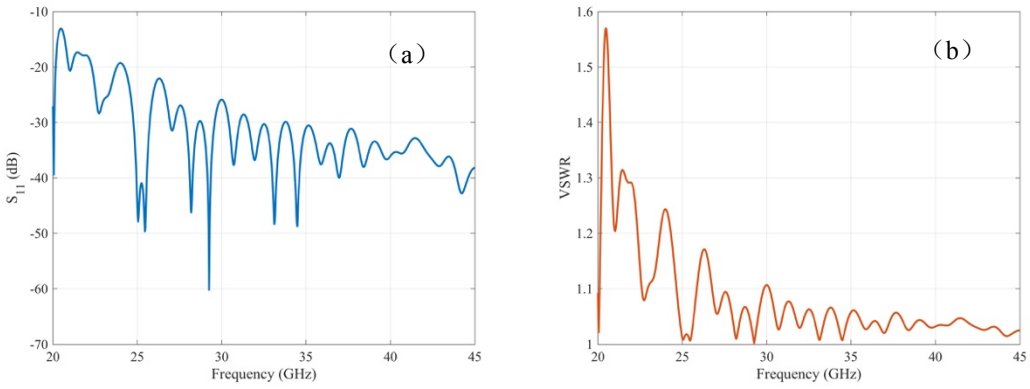

Fig. 7.16 (a) The S_{11} and (b) the VSWR of the HBRIW-based h-plane horn antenna.

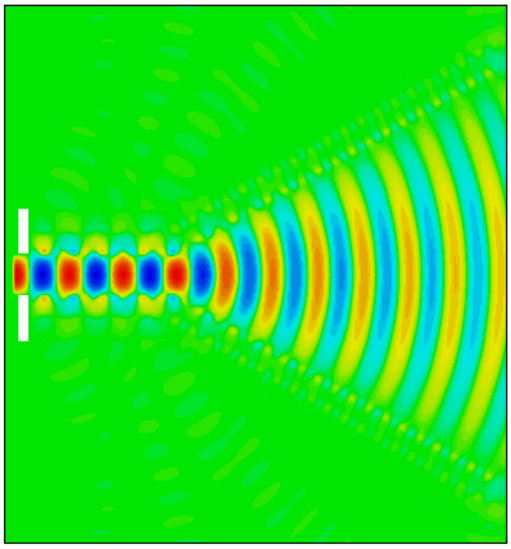

Fig. 7.17 Top view of E_z field component at middle plane of the antenna at 32.5 GHz.

key geometrical and material properties are the same as that of the HBRIW discussed in Chapter 6. The opening angle of the antenna is 30 degrees. A rectangular waveguide with same aperture size as the air core of the antenna is used to feed the antenna. The structure was simulated using CST microwave studio and the simulated S_{11} and voltage standing wave ratio (VSWR) is shown in Fig. 7.16. As discussed in Chapter 6, the operating frequency of the HBRIW ranges from 21 GHz to 44 GHz. The S_{11} and VSWR of the proposed HBRIW h-plane horn antenna is below -17.34 dB and 1.314, respectively, indicating a good matching between the feeding rectangular waveguide and the antenna over a more than one-octave

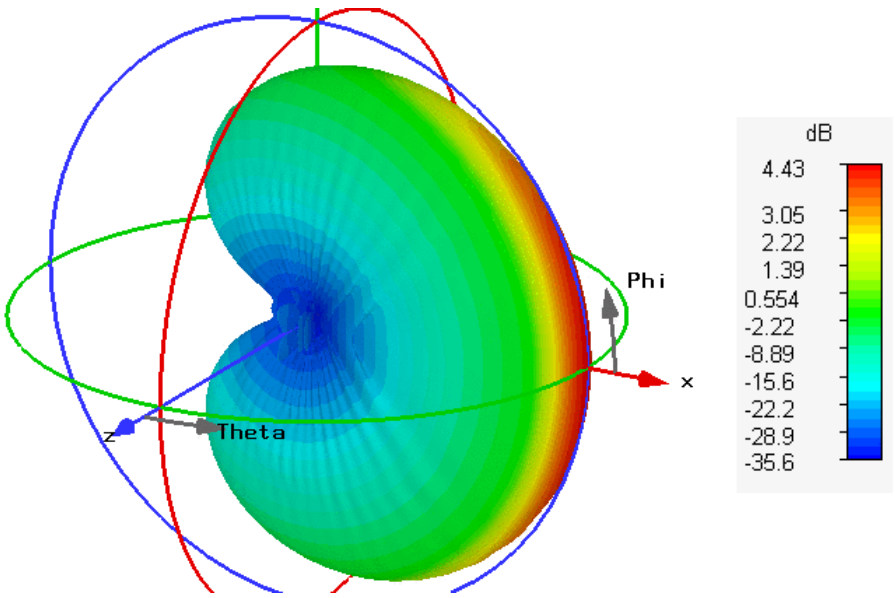

Fig. 7.18 Far-field pattern of the h-plane horn antenna at 32.5 GHz.

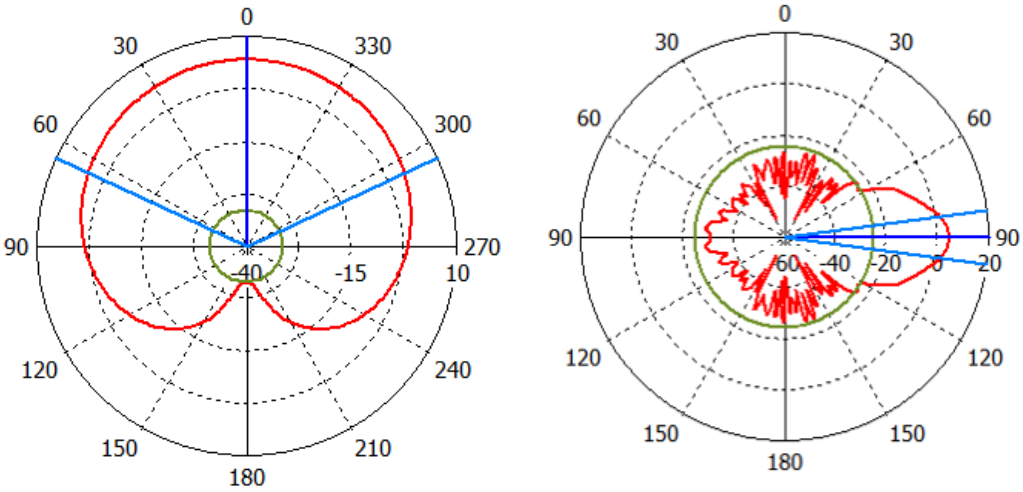

（a）$\theta = 90^o$ （b）$\varphi = 180^o$

Fig. 7.19 The far-field pattern at （a）$\theta = 90^o$ and （b）$\varphi = 180^o$ planes.

operating band.

The E_z field component guided within the antenna at 32.5 GHz is shown in Fig. 7.17. The antenna operating in single-HE_{10}-mode, and the HE_{10} mode is well maintained in the multimode region. The far-field pattern of the antenna at 32.5 GHz is shown in Fig. 7.18. The 3dB beam width of the antenna is 14.8 degrees, so the directivity of the antenna is well controlled by the structure. The far-field patterns in the $\theta = 90^o$ and $\varphi = 180^o$ planes are shown in Fig. 7.19, where θ and φ are the polar angle and azimuth angle, respectively. The main lobe magnitude of the antenna gain is 4.43 dB. The side lobe magnitude is -29 dB which is very well suppressed.

Overall, an h-plane horn antenna formed of HBRIW with S_{11} smaller than -17.34 dB over the operating band from 21 to 44 GHz has been proposed. The far-field patterns shown side lobes are very well suppressed and the difference between the main lobe magnitude and the side lobes magnitude is as great as 33.43 dB.

7.5 Bragg fibre horn antenna

The trimetric view of the geometry of the Bragg fibre horn antenna is shown in Fig. 7.20. The geometric and material properties of the antenna are the same as the Bragg fibre discussed in Chapter 3. The opening angle of the antenna is 12 degrees. It is small because the Bragg fibre is a multimode waveguide which could potentially excite high-order modes when the opening angle is large. Since the size of the Bragg fibre is significantly larger

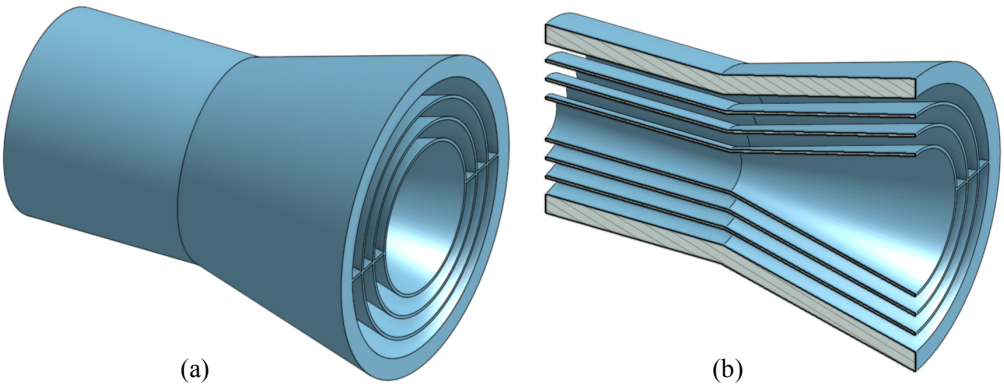

Fig. 7.20 (a) Full structure and (b) cutaway view of the Bragg fibre horn antenna.

than the operating wavelength, it is very hard to do a 3D full-structured simulation due to limited computational sources. Alternatively, a axisymmetric model is studied using COMSOL, as shown in Fig. 7.21. The support bridges are excluded in the simulation. A circular waveguide with the same aperture size as the air core of the Bragg fibre is used to excite the antenna. The simulated S_{11} and VSWR are shown in Fig. 7.22. According to Chapter 3.2, the theoretical operating band of the Bragg fibre ranges from 240 to 300 GHz. From Fig. 7.22, the S_{11} and VSWR is below -38.71 dB and 1.023, respectively, indicating a good matching between the feeding circular waveguide over the designed operating bandwidth. In the simulation, only results at a few frequency points are obtained and displayed because of the limited available computational sources.

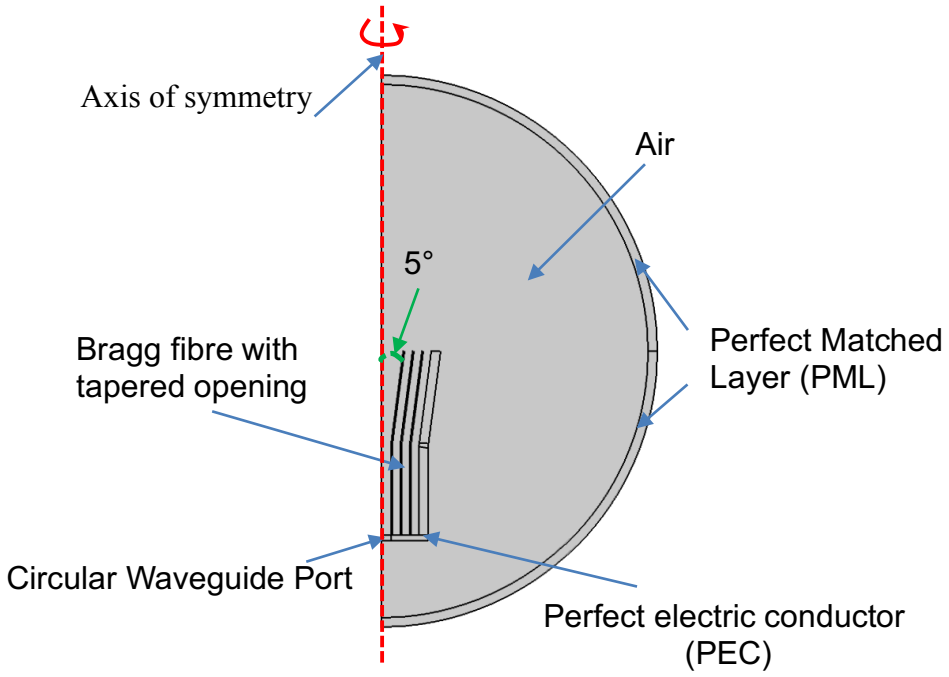

Fig. 7.21 Axisymmetric model of the Bragg fibre horn antenna.

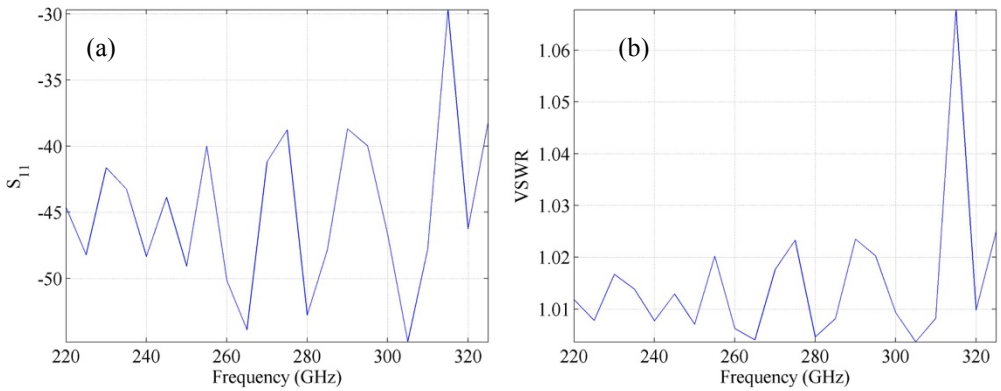

Fig. 7.22 (a) S_{11} and (b) VSWR of the Bragg fibre horn antenna.

The normalized electric field guided inside and near the horn at 272.5 GHz are shown in Fig. 7.23. Like the modal-filtering effect discussed in Chapter 4, some field corresponding to high-order modes radiates at the front part of the antenna, while most of the field is guided inside the waveguide which is operating in asymptotically single-HE_{11}-mode. The 3D far-field pattern of the antenna and its cutaway view in the $\theta = 90^o$ plane at 272.5 GHz are shown in Fig. 7.24. The magnitude of the main lobe is 53.95 dB, and the magnitude of the side lobes are below 22.88 dB. The 3dB beam width of the antenna is 5.43 degree, so the directivity of the antenna is very high.

In summary, a horn antenna design built upon the previous fabricated Bragg fibre is proposed. The horn antenna operates over the designed band of the Bragg fibre ranging from 240 GHz to 300 GHz. The high directivity is due to the small opening angle of the antenna. The difference between the magnitudes of the main lobe and the side lobes are greater than 31.07 dB.

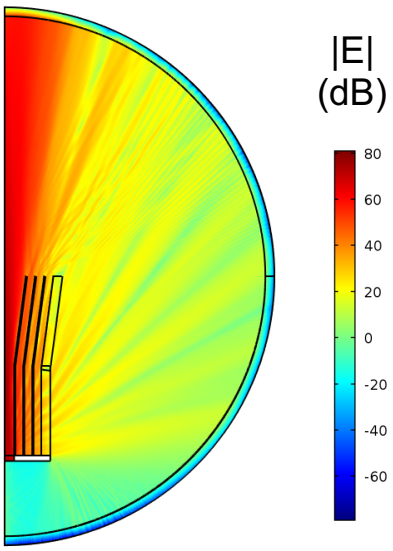

Fig. 7.23 Field distribution inside and near the Bragg fibre horn antenna at 272.5 GHz.

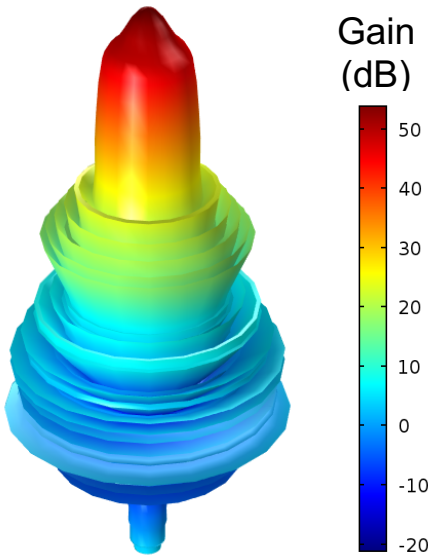

Fig. 7.24 Far-field pattern of the antenna at 272.5 GHz.

7.6 Concluding remarks

In this chapter, several functional components based on the previously studied photonic-crystal-based waveguides are presented, including waveguide bends, splitters, cavities, and horn antennas. The aim of this chapter, however, is not to present optimized functional components, but to demonstrate the photonic-crystal-based waveguides studied in this thesis are very flexible and can be promising candidates as platforms for mmW and THz functional components. Therefore, there is plenty of rooms to improve the performances of the functional components investigated in this chapter. For example, the operating frequency ranges of the waveguide bends and the splitter are significantly reduced owing to defects at the junction, and it can potentially be improved by adding a suitable coupling structure between the input waveguide and the output waveguide(s). In addition, the unloaded q-factor of the HBRIW cavity is low, which can be potentially improved by making the geometric transition between the central guided region and the side dissipating region more smooth. Overall, although only several basic functional components are studied in this chapter, benefiting from the important flexibility of SIW and PCW, many more functional components can be developed based on the photonic-crystal-based waveguides proposed in this thesis.

Chapter 8
Conclusion and Future Work

The thesis has three primary themes: 1) Chapters 2, 3 and 4 compose the first theme on THz Bragg fibres; 2) Chapters 5 and 6 make up the second theme on mmW and THz flat hollow photonic crystal waveguides; 3) Chapter 7 discusses various functional components built upon the proposed mmW and THz waveguides, forming the third theme of the thesis. To be more specific, the main contributions of each theme are summarized as in the following sections.

8.1 THz Bragg fibres

In terms of the Bragg fibre, the author first studied the design principles, and then fabricated and characterised a Bragg fibre, and finally the crucial problems on mode transitions and the modal-filtering effect in an asymptotically single-mode Bragg fibre are further investigated. Specifically, the contributions of Chapters 2, 3 and 4 are highlighted as follows:

- The **Chapter 2** presents a novel design concept, which is verified by analytical and simulation results, of a single-mode small-core terahertz Bragg fibre exhibiting the properties of low loss and low dispersion. Conventionally, a single-TE_{01}-mode Bragg fibre requires a large core and many cladding layer periods to achieve a significant propagation loss discrimination between the desired mode and other unwanted competing modes. The use of a second-order bandgap in this chapter completely eliminates this requirement, and enhances propagation loss discrimination using just a small core with a diameter at least 50% smaller than the conventional design and only four cladding layer periods. Furthermore, a generalized half-wavelength condition is proposed, promoting the manipulation of the photonic bandgap for Bragg fibre. The TE_{01} mode has a null point in the electric field close to the boundary interface between the core and the cladding, and this phenomenon has been exploited to minimize the impact of support bridges, which mechanically maintain the air gaps, on the propagation loss of the fibre. Finally, a novel design is proposed realizing a tightly confined single-TE_{01}-mode small-air-core Bragg fibre with propagation loss and group velocity dispersion less than 1.2 dB/m and -0.6 ps/THz/cm, respectively, between frequencies of 0.85 THz and 1.15 THz.

- In **Chapter 3**, the design and measurement of a 3D-printed low-loss asymptotically single-mode hollow-core terahertz Bragg fibre is reported, operating across the frequency range from 246 to 276 GHz. The HE_{11} mode is employed as it is the lowest loss propagating mode, with the electromagnetic field concentrated within the air core as a result of the photonic crystal bandgap behaviour. The HE_{11} mode also has large loss discrimination compared to its main competing HE_{12} mode. This results in asymptotically single-mode operation of the Bragg fibre, which is verified by extensive simulations based on the actual fabricated Bragg fibre dimensions and measured material parameters. The measured average propagation loss of the Bragg fibre is lower than 5 dB/m over the frequency range from 0.246 to 0.276 THz, which is, to the best of the author's knowledge, the lowest loss asymptotically single-mode all-dielectric microstructured fibre yet reported in this frequency range, with a minimum loss of 3 dB/m at 0.265 THz.
- In **Chapter 4**, the mechanism for electromagnetic (EM) mode transition and filtering in an asymptotically single-HE_{11}-mode hollow THz Bragg fibre is investigated. Bragg fibres with an asymptotically single-mode pattern were designed, fabricated, and measured, achieving measured signal propagation loss of better than 3 dB/m at 265 GHz and with an operating frequency range from 246 to 276 GHz. Mode transition and filtering effects are both verified by 3D full-wave simulations using measured material properties, with geometrical parameters extracted from the fabricated Bragg fibre prototypes. By optimizing the coupling efficiency between the free-space Gaussian beam and the guided Bessel function mode, the optimum distance of mode transition from the Gaussian-beam excitation into the guided mode is calculated to be ~13.7 free-space wavelengths in the fibre, to ensure fast EM-field convergence to the desired asymptotically single-mode mode pattern in the Bragg fibre. After this mode transition region, the electric field amplitude ratio between the desired HE_{11} mode and the main competing HE_{12} mode is approximately 7 times, with the HE_{12} mode attenuation being more than 10 dB/m larger than the fundamental HE_{11} mode; the results indicate that the fibre is one of the best candidates for low-loss asymptotically single-mode terahertz signal interconnections.

8.2 Hollow photonic crystal integrated waveguides

In the case of flat mmW and THz waveguides for compact and multilayer system-in-package applications, the design, fabrication, and characterisation of HPCIW and HBRIW are presented in Chapters 5 and 6, respectively. The major contributions of Chapters 5 and 6 are as follows:

- In **Chapter 5**, a novel waveguide medium that combines the advantages of photonic crystal waveguide (PCW) and substrate integrated waveguide (SIW) is demonstrated, which is called a hollow photonic crystal integrated waveguide (HPCIW). The proposed HPCIW is comprised of an air-core line-defect hexagonal dielectric photonic crystal waveguide sandwiched between two parallel metal plates. The HE_{10} mode can be excited and guided over a fractional bandwidth of 26% centred at $0.453\,c/a$, and a zero group-velocity dispersion point is found at $0.457\,c/a$, where c is the speed of light, and a is the lattice constant of the photonic crystal. The waveguide is experimentally demonstrated in Ka-band and shows good agreement with theoretical analysis and electromagnetic simulations. The measured propagation loss of the HPCIW varies between 0.07 dB/cm and 0.69 dB/cm over the designed operating band of 28.75 GHz to 37.41 GHz, with the minimum loss occurring at 32.66 GHz, while zero group-velocity dispersion is observed at 33.4 GHz. The HPCIW can be scaled for use at terahertz and optical frequencies, and could prove to be an important candidate for millimetre-wave, terahertz and photonic integrated systems employing multi-chip module and integrated circuit fabrication technologies.
- In **Chapter 6**, a novel waveguide medium is proposed, which is called a hollow Bragg reflector integrated waveguide (HBRIW), that can work more than one octave in single-HE_{10}-mode pattern. The proposed HBRIW comprises of an air-core line-defect one-dimensional photonic crystal waveguide, namely Bragg reflector waveguide, sandwiched between two parallel metal plates. It possesses the merits of both photonic crystal waveguide (PCW) and substrate integrated waveguide (SIW). The waveguide is experimentally demonstrated around Ka-band with a good agreement with theoretical analysis and electromagnetic simulations. The measured propagation loss of the HBRIW is less than 0.81 dB/cm over the designed operating band of 21 GHz to 44 GHz, while the zero group-velocity dispersion point is found to be at 37.5 GHz. The

HBRIW can be scaled for use at other frequencies, such as terahertz and optical frequencies. It is could prove to be a strong candidate for millimetre-wave and terahertz multilayer system-in-package (SiP) applications.

8.3 Photonic crystal functional components

The **Chapter 7** investigates several typical functional components based on the photonic-crystal-based waveguides that have been discussed in previous chapters. To be more specific, the following functional components have designed in Chapter 7:

1) A 60^{o} waveguide bend based on the HPCIW presented in Chapter 5 and a 90^{o} waveguide bend based on the HBRIW presented in Chapter 6 have been proposed in section 7.1. The operating bandwidths of the waveguide bends are observed to be narrower that the corresponding straight waveguides. It is due to the discontinuity of the propagation constant at the junction of the waveguide and the incomplete photonic bandgap. Nonetheless, low loss guiding of millimetre-wave waveguide curved bends within the supported band are demonstrated.
2) A splitter based on the HPCIW presented in Chapter 5 has been proposed in section 7.2. The splitter operates from 28 GHz to 30 GHz, with a typical S_{21} or S_{31} value of -4 dB. The operating bandwidth of the splitter is significantly reduced due to the discontinuities at the junction and the incomplete photonic bandgap. When the photonic bandgap of the waveguide is not omnidirectional, the guided modes in the line-defect air core could potentially couple with cladding modes which mainly distributed in the bulk photonic crystal structures, and consequently increases the loss.
3) A novel cavity based on the HBRIW presented in Chapter 6 has been proposed in section 7.3. The central region of the cavity supports modes which are not supported in the side regions. The field is thereby mainly confined in the central region and decreases exponentially in the side regions, which is similar to the situation of electrons in a quantum well. The cavity is resonant at 21.99 GHz with a unloaded q-factor of 595.72, and it can be a very useful component in many functional components, like sensors, filters, etc.
4) An h-plane horn antenna based on the HBRIW presented in Chapter 6 has been proposed in section 7.4. The operating bandwidth of the proposed h-plane horn antenna is as wide as the basic HBRIW. Over

the operating band from 21 to 44 GHz, the S11 is smaller than -17.34 dB and the VSWR is less than 1.314. The 3dB beam width of the antenna is 14.8 degrees. The minimum difference between the main lobe magnitude and side lobes magnitude is as great as 33.43 dB, indicating the side lobes are very well suppressed in the proposed h-plane horn antenna.

5) A horn antenna based on the Bragg fibre characterised in Chapter 3 has been proposed in section 7.5. The horn antenna operates over the whole operating band of the Bragg fibre. The 3dB beam width of the antenna is 5.43 degrees, so the directivity of the proposed antenna is narrow due to the fact that the Bragg fibre is an overmoded structure operating in asymptotically single-mode pattern, and it is sensitive to the change of the core radius. The far-field pattern of the proposed antenna has been simulated suggesting a minimum difference between the main lobe magnitude and side lobes magnitude of 31.07 dB.

Overall, the photonic-crystal-based waveguides have proven to be flexible, expandable, and scalable, as well as very promising candidates as the platforms for mmW and THz functional components, although there is plenty of room to optimise the proposed functional components.

8.4 Future work

In this research, several mmW and THz microstructured fibres or waveguides based on photonic crystals are first investigated, followed by some designs of functional components formed of them. To give some recommendations for future works, from easy to difficult, few topics are pointed out as follows:

Firstly, to extend the operating frequencies of the proposed photonic crystal waveguides to higher frequencies is of great interesting. In Chapter 3, a sub-THz Bragg fibre is fabricated and characterized. To fabricated a Bragg fibre operating above 1 THz could have many important applications, such as coupling the power of a THz quantum cascade laser (QCL) out from a cryogenic chamber. The potential fabrication techniques could be polymer extrusion or fibre drawing, and the promising candidate for the dielectric materials for the Bragg fibre could be low-loss polymers and silica. In Chapters 5 and 6, two flat photonic crystal waveguides operating at Ka-band are demonstrated. They can be easily scaled to other frequencies by changing the constant lattice of the photonic crystals and choosing proper low-loss materials. It is very interesting to demonstrate them at around 1

THz which had never been done before. The potential fabrication techniques to fabricate the flat photonic crystal waveguides at higher frequencies could be photolithography and deep-ion reactive etching, and one of the candidate materials is high-resistivity silicon. The propagation losses of the flat waveguides can be further reduced by using more precise and robust fabrication techniques. It is also interesting to widen the zero- or low-GVD band of these flat waveguides by adjusting the geometric parameters.

Secondly, in Chapter 7, several types of functional components are presented, including waveguide bends, splitters, cavities, and antennas. Benefiting from the flexibility of photonic crystal structure, it is not surprise to build more active and passive components using them, such as photonic crystal laser, Cherenkov radiation source, high-Q resonator, multiplexer, filter and antenna array. The potential future works could be either optimising the proposed functional components presented in Chapter 7, or building other functional components. For example, the operating bandwidths and propagation losses of the waveguide bends and splitter can be further improved by carefully design the coupling at the junction; the Q-factor of the cavity can potentially be improved by enhancing the field confinement of the cavity; antenna rotator or omnidirectional antenna can be built based on the Bragg fibre, thanks to the its circular geometry; and the flat architecture of the HBRIW H-plane horn antenna makes it desirable for multilayer antenna array.

Thirdly, sensors to characterize the dielectric properties of solids, liquids and gases are feasible applications for the proposed photonic crystal based waveguides. Many matters have special spectrum in the THz frequency range, like large molecules, explosives, and pharmaceuticals, which is called as “THz fingerprint”. Sensors using resonating configuration, which measure the material at a frequency point, or non-resonating configuration, which detect over a wide band, is interesting for lab-in-a-waveguide systems which does not require too expensive fabrication and measurement facilities.

Lastly, maybe the most challenging but also most rewarding project goes to the multilayer THz system-in-package (TSiP) which integrates multi-functional chips and components. This idea is simple. Since it is obvious that many functional components can be developed based on the proposed photonic crystal based waveguides, why not integrate them together and build a circuit? However, the idea is also complicate. How to integrate active components with passive components, how to integrate tiny chip with subwavelength waveguide, how to design the transition between different

components, and how to couple the EM field vertically, are challenging problems.

In summary, we have discussed the potential applications of the proposed photonic crystal based waveguides in many respects. Some of them are relatively easy and low cost, while some others are difficult and rely very much on the research grants.

Appendix A
Transfer-Matrix Method

The dispersion relations and guided mode in Bragg fibre was first derived by Yeh *et al.* [87]. In each cladding layer of Bragg fibre (excluding the outermost layer), the four field components ($E_z, H_\theta, H_z, E_\theta$) can be expressed in matrix form:

$$\begin{bmatrix} E_z \\ H_\theta \\ H_z \\ E_\theta \end{bmatrix} = \begin{bmatrix} J_m(k_i r) & Y_m(k_i r) & 0 & 0 \\ \frac{i\omega\varepsilon_i}{k_i} J'_m(k_i r) & \frac{i\omega\varepsilon_i}{k_i} Y'_m(k_i r) & -\frac{m\beta}{k_i^2 r} J_m(k_i r) & -\frac{m\beta}{k_i^2 r} Y_m(k_i r) \\ 0 & 0 & J_m(k_i r) & Y_m(k_i r) \\ -\frac{m\beta}{k_i^2 r} J_m(k_i r) & -\frac{m\beta}{k_i^2 r} Y_m(k_i r) & -\frac{i\omega\mu_i}{k_i} J'_m(k_i r) & -\frac{i\omega\mu_i}{k_i} Y'_m(k_i r) \end{bmatrix} \begin{bmatrix} A_j \\ B_j \\ C_j \\ D_j \end{bmatrix} \tag{A.1}$$

where J and Y indicate the Bessel and Neumann functions respectively; A, B, C and D are the coefficients; m is the azimuthal modal number; and the choice of i $(=a,b,c)$ is based on the layer number j ; r is the radial position; ε_i and μ_i are permittivity and permeability of layer j, respectively. For m=0, the guided modes in Bragg fibre are exactly TE and TM polarized, while for nonzero m, TE modes become HE modes, and TM modes become EH modes. The nonzero m modes are doubly degenerate, while the m=0 modes are nondegenerate [126].

In the outermost layer, there will be no incoming waves since there is no reflections from outside [125], and the Bessel (J) and Neumann (Y) functions are replaced by the first ($H^I = J + iY$) and second ($H^{II} = J - iY$) kind of Hankel functions. According to the boundary condition, all of the four field components should be continuous across the interfaces. Therefore, a transfer matrix [**T**] for a $f - n_{eff}$ pair (or $\beta - \omega$) is obtained to relate the coefficients in the innermost layer ($j = 1$) and the outermost layer ($j = N$) [87, 125]:

$$\begin{bmatrix} A_1 \\ B_1 \\ C_1 \\ D_1 \end{bmatrix} = \begin{bmatrix} T_{11} & T_{12} & T_{13} & T_{14} \\ T_{21} & T_{22} & T_{23} & T_{24} \\ T_{31} & T_{32} & T_{33} & T_{34} \\ T_{41} & T_{42} & T_{43} & T_{44} \end{bmatrix} \begin{bmatrix} A_N \\ B_N \\ C_N \\ D_N \end{bmatrix} \tag{A.2}$$

Note that the layer number N includes the core, the period structures and the outermost layer. Since the Neumann function (Y) goes to infinite at the

origin, $B_1 = D_1 = 0$, and because there is no incoming wave in the outermost cladding, $B_N = D_N = 0$. Substituting above conditions into Eqn. (A.2) gives

$$\begin{bmatrix} T_{21} & T_{23} \\ T_{41} & T_{43} \end{bmatrix} \begin{bmatrix} A_N \\ C_N \end{bmatrix} = 0 \tag{A.3}$$

The nontrivial solution condition is:

$$\det \begin{bmatrix} T_{21} & T_{23} \\ T_{41} & T_{43} \end{bmatrix} = 0 \tag{A.4}$$

Eqn. (A.4) is a multi-value complex transcendental eigenvalue equation. Since the confined modes in Bragg fibre are analogous to the guided modes of a hollow metallic circular waveguide with same core radius [126], The eigenvalue equation can be split into real part and imaginary part, and simply use the dispersion relations of the hollow metallic circular waveguide as the initial value of the root's real part and use zero as the initial value of the root's imaginary part, and solve Eqn. (A.4) in a multi-variable root finder, like 'fsolve' in Matlab®. Due to the multi-value nature of Eqn. (A.4), many other modes with same azimuthal modal number (*m*) may be found, rather than the desired mode. Thus, the root (namely the complex effective refractive index n_{eff}) should be verified by using simulation software, like 'mode analysis solver' in COMSOL®. This method is known as transfer matrix method [87, 125].

Once, the complex effective refractive index (n_{eff}) is obtained from Eqn. (A.4), one can calculate the propagation loss in dB/m using the following relations [180]:

$$L = \frac{40\pi}{\lambda \ln 10} \mathrm{Im}\left(n_{eff}\right) \tag{A.5}$$

Index

n_c	Refractive index of the core
n_a	Refractive index of the high-index layer
n_b	Refractive index of the low-index layer
a	Thickness of the high-index layer
b	Thickness of the low-index layer
r_c	Radius of the core
Λ	Period of the radial photonic crystal
k_i	Lateral propagation constant
k_0	Vacuum wavenumber
k_0	Vacuum angular frequency
c	The speed of light in vacuum
β	Longitudinal propagation constant
n_{eff}	Effective refractive index
ξ_i	1 for TE modes or $1/n_i^2$ $(i = a, b)$ for TM modes
λ_t	Wavelength of interest
n_t	Effective refractive index of interest
θ	Angle of incident
ζ	The order number of the bandgap
τ	Porosity factor
$\varkappa$	Absorption coefficient
f	Frequency
Δ	The midrange ratio of the bandgap
f_h	the upper edge of the photonic bandgap
f_l	the lower edge of the photonic bandgap
θ_{B}	Brewster angle

n_{B}	Effective refractive index for Brewster phenomenon
κ	Extinction coefficient
λ_0	Free-space wavelength
r_m	Core radius of feeding HMCW for Bragg fibre
A and B	Amplitude
υ	Spatial frequency of wave
λ_g	Guided wavelength
ε	Permittivity
μ	Permeability

Abbreviations

mmW	Millimetre wave
THz	Terahertz
PCW	Photonic crystal waveguide
TSiP	THz system in package
GVD	Group velocity dispersion
THz-TDS	Terahertz time-domain spectroscopy
SIW	Substrate integrated waveguide
HPCW	Hollow photonic crystal waveguide
SIIG	Substrate integrated image guide
3D	Three-dimensional
EM	Electromagnetic
COC	Cyclic olefin copolymer
SOS	Silicon-on-sapphire
LTCC	Low temperature co-fired ceramic
QWC	Quarter-wavelength condition
GHWC	Generalized half-wavelength condition
SPARROW	Stratified planar anti-resonant reflecting optical waveguide
CLD	Confinement loss diagram
VNA	Vector network analyzer
RWG	Rectangular waveguide
HMCW	Hollow metallic circular waveguide
HPCIW	Hollow photonic crystal integrated waveguide
MPB	MIT Photonic Bands
2D	Two-dimensional
DUT	Device under test

TRL	Thru-Reflect-Line
SOLT	Short-Open-Line-Thru
HBRIW	Hollow Bragg reflector integrated waveguide
DC	Direct current
1D	One-dimensional
VSWR	Voltage Standing Wave Ratio
QCL	Quantum Cascade Laser

References

[1] Davies, A. G., Burnett, A. D., Fan, W., Linfield, E. H., & Cunningham, J. E. (2008). Terahertz spectroscopy of explosives and drugs. *Materials Today*, 11(3), 18-26.

[2] Siegel, P. H. (2007). THz instruments for space. *Antennas and Propagation, IEEE Transactions on*, 55(11), 2957-2965.

[3] Rostami, A., Rasooli, H., & Baghban, H. (2010). *Terahertz technology: fundamentals and applications* (Vol. 77). Springer Science & Business Media.

[4] Siegel, P. H. (2004, June). Terahertz technology in biology and medicine. In *Microwave Symposium Digest, 2004 IEEE MTT-S International* (Vol. 3, pp. 1575-1578). IEEE.

[5] Jepsen, P. U., Cooke, D. G., & Koch, M. (2011). Terahertz spectroscopy and imaging–Modern techniques and applications. *Laser & Photonics Reviews*, 5(1), 124-166.

[6] Tonouchi, M. (2007). Cutting-edge terahertz technology. *Nature photonics*, 1(2), 97-105.

[7] Orlando, A. R., & Gallerano, G. P. (2009). Terahertz radiation effects and biological applications. *Journal of Infrared, Millimeter, and Terahertz Waves*, 30(12), 1308-1318.

[8] Williams, G.P., 2005. Filling the THz gap—high power sources and applications. *Reports on Progress in Physics*, 69(2), p.301.

[9] Dhillon, S.S., Vitiello, M.S., Linfield, E.H., Davies, A.G., Hoffmann, M.C., Booske, J., Paoloni, C., Gensch, M., Weightman, P., Williams, G.P. and Castro-Camus, E., 2017. The 2017 terahertz science and technology roadmap. *Journal of Physics D: Applied Physics*, 50(4), p.043001.

[10] Argyros, A., 2013. Microstructures in polymer fibres for optical fibres, THz waveguides, and fibre-based metamaterials. *ISRN Optics*, 2013.

[11] Dai, J., Zhang, J., Zhang, W. and Grischkowsky, D., 2004. Terahertz time-domain spectroscopy characterization of the far-infrared absorption and index of refraction of high-resistivity, float-zone silicon. *JOSA B*, 21(7), pp.1379-1386.

[12] Thomson Reuters, Web of Science, https://apps.webofknowledge.com/, Online; accessed 2017-04-22.

[13] Yablonovitch, E., Gmitter, T.J. and Leung, K.M., 1991. Photonic band structure: The face-centered-cubic case employing nonspherical atoms. *Physical review letters*, 67(17), p.2295.

[14] Yeh, P. and Yariv, A., 1976. Bragg reflection waveguides. *Optics Communications*, 19(3), pp.427-430.

[15] Nordquist, C. D., Wanke, M. C., Rowen, A. M., Arrington, C. L., Lee, M., & Grine, A. D. (2008, July). Design, fabrication, and characterization of metal micromachined rectangular waveguides at 3 THz. In *Antennas and Propagation Society International Symposium, 2008. AP-S 2008. IEEE* (pp. 1-4). IEEE.

[16] Ito, T., Matsuura, Y., Miyagi, M., Minamide, H., & Ito, H. (2007). Flexible terahertz fibre optics with low bend-induced losses. *JOSA B*, 24(5), 1230-1235.

[17] Mendis, R., & Grischkowsky, D. (2001). Undistorted guided-wave propagation of subpicosecond terahertz pulses. *Optics letters*, 26(11), 846-848.

[18] Mendis, R., & Grischkowsky, D. (2000). Plastic ribbon THz waveguides. *Journal of Applied Physics*, 88(7), 4449-4451.

[19] Wang, K., & Mittleman, D. M. (2004). Metal wires for terahertz wave guiding. *Nature*, 432(7015), 376-379.

[20] Pahlevaninezhad, H., Darcie, T. E., & Heshmat, B. (2010). Two-wire waveguide for terahertz. *Optics express*, 18(7), 7415-7420.

[21] Heiliger, H.M., Nagel, M., Roskos, H.G., Kurz, H., Schnieder, F., Heinrich, W., Hey, R. and Ploog, K., 1997. Low-dispersion thin-film microstrip lines with cyclotene (benzocyclobutene) as dielectric medium. *Applied physics letters*, 70(17), pp.2233-2235.

[22] Frankel, M.Y., Gupta, S., Valdmanis, J.A. and Mourou, G.A., 1991. Terahertz attenuation and dispersion characteristics of coplanar transmission lines. *IEEE Transactions on microwave theory and techniques*, 39(6), pp.910-916.

[23] Grischkowsky, D.R., 2000. Optoelectronic characterization of transmission lines and waveguides by terahertz time-domain spectroscopy. *IEEE Journal of Selected Topics in Quantum Electronics*, 6(6), pp.1122-1135.

[24] Jeon, T. I., & Grischkowsky, D. (2004). Direct optoelectronic generation and detection of sub-ps-electrical pulses on sub-mm-coaxial transmission lines. *Applied physics letters*, 85(25), 6092-6094.

[25] Fesharaki, F., Djerafi, T., Chaker, M. and Wu, K., 2016, May. Mode-selective transmission line for DC-to-THz super-broadband operation. In *Microwave Symposium (IMS), 2016 IEEE MTT-S International* (pp. 1-4). IEEE.

[26] Jin, L., Lee, R.M.A. and Robertson, I., 2014. Analysis and design of a novel low-loss hollow substrate integrated waveguide. *IEEE Transactions on Microwave Theory and Techniques*, 62(8), pp.1616-1624.

[27] Dupuis, A., Allard, J. F., Morris, D., Stoeffler, K., Dubois, C., & Skorobogatiy, M. (2009). Fabrication and THz loss measurements of porous subwavelength fibres using a directional coupler method. *Optics express*, 17(10), 8012-8028.

[28] Chen, L. J., Chen, H. W., Kao, T. F., Lu, J. Y., & Sun, C. K. (2006). Low-loss subwavelength plastic fibre for terahertz waveguiding. *Optics Letters*, 31(3), 308-310.

[29] Lai, C. H., Hsueh, Y. C., Chen, H. W., Huang, Y. J., Chang, H. C., & Sun, C. K. (2009). Low-index terahertz pipe waveguides. *Optics letters,* 34(21), 3457-3459.

[30] Bao, H., Nielsen, K., Bang, O., & Jepsen, P. U. (2015). Dielectric tube waveguides with absorptive cladding for broadband, low-dispersion and low loss THz guiding. *Scientific reports*, 5, 7620.

[31] Xiao, M., Liu, J., Zhang, W., Shen, J., & Huang, Y. (2013). Self-supporting polymer pipes for low loss single-mode THz transmission. *Optics express*, 21(17), 19808-19815.

[32] Matsuura, Y., & Takeda, E. (2008). Hollow optical fibres loaded with an inner dielectric film for terahertz broadband spectroscopy. *JOSA B*, 25(12), 1949-1954.

[33] Bowden, B., Harrington, J. A., & Mitrofanov, O. (2008). Low-loss modes in hollow metallic terahertz waveguides with dielectric coatings. *Applied physics letters*, 93(18), 181104-181104.

[34] Navarro-Cía, M., Vitiello, M. S., Bledt, C. M., Melzer, J. E., Harrington, J. A., & Mitrofanov, O. (2013). Terahertz wave transmission in flexible polystyrene-lined hollow metallic waveguides for the 2.5-5 THz band. *Optics express*, 21(20), 23748-23755.

[35] Mitrofanov, O., James, R., Fernández, F. A., Mavrogordatos, T. K., & Harrington, J. A. (2011). Reducing transmission losses in hollow THz waveguides. *Terahertz Science and Technology, IEEE Transactions on*, 1(1), 124-132.

[36] Anthony, J., Leonhardt, R., Argyros, A., & Large, M. C. (2011). Characterization of a microstructured Zeonex terahertz fibre. *JOSA B*, 28(5), 1013-1018.

[37] Yudasari, N., Vogt, D., Anthony, J., & Leonhardt, R. (2014, September). Hollow Core Terahertz Waveguide Fabricated using a 3D Printer. In *Infrared, Millimeter, and Terahertz waves (IRMMW-THz), 2014 39th International Conference on (pp. 1-2)*. IEEE.

[38] Atakaramians, S., Afshar V, S., Ebendorff-Heidepriem, H., Nagel, M., Fischer, B. M., Abbott, D., & Monro, T. M. (2009). THz porous fibres: design, fabrication and experimental characterization. *Optics express*, 17(16), 14053-15062.

[39] Anthony, J., Leonhardt, R., Leon-Saval, S. G., & Argyros, A. (2011). THz propagation in kagome hollow-core microstructured fibres. *Optics express*, 19(19), 18470-18478.

[40] Dupuis, A., Mazhorova, A., DÚsÚvÚdavy, F., RozÚ, M., & Skorobogatiy, M. (2010). Spectral characterization of porous dielectric subwavelength THz fibers fabricated using a microstructured molding technique. *Optics express*, 18(13), 13813-13828.

[41] Nielsen, K., Rasmussen, H. K., Adam, A. J., Planken, P. C., Bang, O., & Jepsen, P. U. (2009). Bendable, low-loss TOPAS fibres for the terahertz frequency range. *Optics Express*, 17(10), 8592-8601.

[42] Wu, Z., Ng, W. R., Gehm, M. E., & Xin, H. (2011). Terahertz electromagnetic crystal waveguide fabricated by polymer jetting rapid prototyping. *Optics express*, 19(5), 3962-3972.

[43] Dupuis, A., Stoeffler, K., Ung, B., Dubois, C., & Skorobogatiy, M. (2011). Transmission measurements of hollow-core THz Bragg fibres. *JOSA B*, 28(4), 896-907.

[44] Skorobogatiy, M., & Dupuis, A. (2007). Ferroelectric all-polymer hollow Bragg fibres for terahertz guidance. *Applied physics letters*, 90(11), 113514.

[45] Ponseca Jr, C. S., Pobre, R., Estacio, E., Sarukura, N., Argyros, A., Large, M. C., & van Eijkelenborg, M. A. (2008). Transmission of terahertz radiation using a microstructured polymer optical fibre. *Optics letters*, 33(9), 902-904.

[46] Lu, J. Y., Yu, C. P., Chang, H. C., Chen, H. W., Li, Y. T., Pan, C. L., & Sun, C. K. (2008). Terahertz air-core microstructure fibre. *Applied Physics Letters,* 92(6), 064105.

[47] Han, H., Park, H., Cho, M., & Kim, J. (2002). Terahertz pulse propagation in a plastic photonic crystal fibre. *Applied Physics Letters*, 80(15), 2634-2636.

[48] Atakaramians, S., Afshar V, S., Nagel, M., Rasmussen, H.K., Bang, O., Monro, T.M. and Abbott, D., 2011. Direct probing of evanescent field for characterization of porous terahertz fibers. *Applied Physics Letters*, *98*(12), p.121104.

[49] Yang, J., Zhao, J., Gong, C., Tian, H., Sun, L., Chen, P., Lin, L. and Liu, W., 2016. 3D printed low-loss THz waveguide based on Kagome photonic crystal structure. *Optics Express*, *24*(20), pp.22454-22460.

[50] Li, J., Nallappan, K., Guerboukha, H. and Skorobogatiy, M., 2017. 3D printed hollow core terahertz Bragg waveguides with defect layers for surface sensing applications. *Optics express*, *25*(4), pp.4126-4144.

[51] Setti, V., Vincetti, L. and Argyros, A., 2013. Flexible tube lattice fibers for terahertz applications. *Optics express*, *21*(3), pp.3388-3399.

[52] Lu, W., Lou, S. and Argyros, A., 2016. Investigation of flexible low-loss hollow-core fibres with tube-lattice cladding for terahertz

radiation. *IEEE Journal of Selected Topics in Quantum Electronics*, *22*(2), pp.214-220.

[53] Bao, H., Nielsen, K., Rasmussen, H.K., Jepsen, P.U. and Bang, O., 2012. Fabrication and characterization of porous-core honeycomb bandgap THz fibers. *Optics express*, *20*(28), pp.29507-29517.

[54] Hong, B., Swithenbank, M., Greenall, N., Clarke, R.G., Chudpooti, N., Akkaraekthalin, P., Somjit, N., Cunningham, J.E. and Robertson, I.D., 2018. Low-Loss Asymptotically Single-Mode THz Bragg Fiber Fabricated 5. *IEEE Transactions on Terahertz Science and Technology*, *8*(1), pp.90-99.

[55] Virginia Diodes Inc., Waveguide Band Designations, http://vadiodes.com/images/AppNotes/VDI_Waveguide_Designations_2015.01.pdf, Online; accessed 2018-04-08

[56] Miller, S. E., & Beck, A. C. (1953). Low-loss waveguide transmission. *Proceedings of the IRE*, 41(3), 348-358.

[57] Gallot, G., Jamison, S. P., McGowan, R. W., & Grischkowsky, D. (2000). Terahertz waveguides. *JOSA B*, 17(5), 851-863.

[58] Ito, T., Matsuura, Y., Miyagi, M., Minamide, H. and Ito, H., 2007. Flexible terahertz fiber optics with low bend-induced losses. *JOSA B*, 24(5), pp.1230-1235.

[59] Doradla, P., Joseph, C. S., Kumar, J., & Giles, R. H. (2012). Characterization of bending loss in hollow flexible terahertz waveguides. *Optics express*, 20(17), 19176-19184.

[60] Navarro-Cía, M., Melzer, J. E., Harrington, J. A., & Mitrofanov, O. (2015). Silver-Coated Teflon Tubes for Waveguiding at 1–2 THz. *Journal of Infrared, Millimeter, and Terahertz Waves*, 36(6), 542-555.

[61] Bowden, B., Harrington, J. A., & Mitrofanov, O. (2008). Fabrication of terahertz hollow-glass metallic waveguides with inner dielectric coatings. *Journal of Applied Physics*, 104(9), 093110.

[62] Bowden, B., Harrington, J. A., & Mitrofanov, O. (2008). Low-loss modes in hollow metallic terahertz waveguides with dielectric coatings. *Applied physics letters*, 93(18), 181104.

[63] Zhan, H., Mendis, R. and Mittleman, D.M., 2009, August. Terahertz energy confinement in finite-width parallel-plate waveguides. In *International Symposium on Photoelectronic Detection and Imaging 2009: Terahertz and High Energy Radiation Detection Technologies and Applications* (Vol. 7385, p. 73851K). International Society for Optics and Photonics.

[64] Bowden, B., Harrington, J. A., & Mitrofanov, O. (2007). Silver/polystyrene-coated hollow glass waveguides for the transmission of terahertz radiation. *Optics Letters*, 32(20), 2945-2947.

[65] Mbonye, M., Mendis, R., & Mittleman, D. M. (2013). Measuring TE1 mode Losses in Terahertz Parallel-Plate Waveguides. *Journal of Infrared, Millimeter, and Terahertz Waves*, 34(7-8), 416-422.

[66] Mendis, R., & Mittleman, D. M. (2009). Comparison of the lowest-order transverse-electric (TE1) and transverse-magnetic (TEM) modes of the parallel-plate waveguide for terahertz pulse applications. Optics express, 17(17), 14839-14850.

[67] Atakaramians, S., Afshar V, S., Monro, T. M., & Abbott, D. (2013). Terahertz dielectric waveguides. *Advances in Optics and Photonics*, 5(2), 169-215.

[68] Jeon, T. I., Zhang, J., & Grischkowsky, D. (2005). THz Sommerfeld wave propagation on a single metal wire. *Applied Physics Letters*, 86(16), 161904.

[69] Deibel, J. A., Wang, K., Escarra, M. D., & Mittleman, D. (2006). Enhanced coupling of terahertz radiation to cylindrical wire waveguides. *Optics express*, 14(1), 279-290.

[70] Chen, L.J., Chen, H.W., Kao, T.F., Lu, J.Y. and Sun, C.K., 2006. Low-loss subwavelength plastic fiber for terahertz waveguiding. Optics Letters, 31(3), pp.308-310.

[71] Jamison, S. P., McGowan, R. W., & Grischkowsky, D. (2000). Single-mode waveguide propagation and reshaping of sub-ps terahertz pulses in sapphire fibres. *Applied Physics Letters*, 76(15), 1987-1989.

[72] Roze, M., Ung, B., Mazhorova, A., Walther, M. and Skorobogatiy, M., 2011. Suspended core subwavelength fibers: towards practical designs for low-loss terahertz guidance. *Optics express*, 19(10), pp.9127-9138.

[73] Lai, C. H., You, B., Lu, J. Y., Liu, T. A., Peng, J. L., Sun, C. K., & Chang, H. C. (2010). Modal characteristics of antiresonant reflecting pipe waveguides for terahertz waveguiding. *Optics express*, 18(1), 309-322.

[74] Belenguer, A., Esteban, H. and Boria, V.E., 2014. Novel empty substrate integrated waveguide for high-performance microwave integrated circuits. *IEEE Transactions on Microwave Theory and Techniques*, *62*(4), pp.832-839.

[75] Parment, F., Ghiotto, A., Vuong, T.P., Duchamp, J.M. and Wu, K., 2015. Air-filled substrate integrated waveguide for low-loss and high power-handling millimeter-wave substrate integrated circuits. *IEEE Transactions on Microwave Theory and Techniques*, *63*(4), pp.1228-1238.

[76] K. Tsuruda, M. Fujita, and T. Nagatsuma, "Extremely low-loss terahertz waveguide based on silicon photonic-crystal slab," *Opt. Exp.*, vol. 23, no. 25, pp. 31977-31990, Dec 2015.

[77] Amarloo, H. and Safavi-Naeini, S., 2017. Terahertz Line Defect Waveguide Based on Silicon-on-Glass Technology. *IEEE Transactions on Terahertz Science and Technology*, *7*(4), pp.433-439.

[78] T. Nagatsuma, S. Hisatake, M. Fujita, H. H. N. Pham, K. Tsuruda, S. Kuwano, and J. Terada, " Millimeter-wave and terahertz-wave applications enabled by photonics," *IEEE J. Quantum Electron*, vol. 52, no. 1, pp. 1-12, Jan 2016.

[79] Zhao, Y. and Grischkowsky, D.R., 2007. 2-D terahertz metallic photonic crystals in parallel-plate waveguides. *IEEE transactions on Microwave Theory and Techniques*, *55*(4), pp.656-663.

[80] A. L. Bingham, and D. R. Grischkowsky, "Terahertz 2-D photonic crystal waveguides," *IEEE Microw. Compon. Lett.,* vol. 18, no. 7, pp. 428-430, Jul. 2008.

[81] Ranjkesh, N., Basha, M., Taeb, A. and Safavi-Naeini, S., 2015. Silicon-on-glass dielectric waveguide—Part II: For THz applications. *IEEE Transactions on Terahertz Science and Technology*, *5*(2), pp.280-287.

[82] Malekabadi, A., Charlebois, S.A., Deslandes, D. and Boone, F., 2014. High-resistivity silicon dielectric ribbon waveguide for single-mode low-loss propagation at F/G-bands. *IEEE Transactions on Terahertz Science and Technology*, *4*(4), pp.447-453

[83] Patrovsky, A. and Wu, K., 2006. Substrate integrated image guide (SIIG)-a planar dielectric waveguide technology for millimeter-wave applications. *IEEE transactions on Microwave Theory and Techniques*, *54*(6), pp.2872-2879.

[84] Knight, J. C., Birks, T. A., Russell, P. S. J., & Atkin, D. M. (1996). All-silica single-mode optical fibre with photonic crystal cladding. *Optics letters*, 21(19), 1547-1549.

[85] Vincetti, L., 2016. Empirical formulas for calculating loss in hollow core tube lattice fibers. *Optics express*, *24*(10), pp.10313-10325.

[86] Vincetti, L., 2010. Single-mode propagation in triangular tube lattice hollow-core terahertz fibers. *Optics Communications*, *283*(6), pp.979-984.

[87] Yeh, P., Yariv, A. and Marom, E., 1978. Theory of Bragg fiber. *JOSA*, *68*(9), pp.1196-1201.

[88] Russell, P., 2003. Photonic crystal fibers. *science*, *299*(5605), pp.358-362.

[89] Poletti, F., 2014. Nested antiresonant nodeless hollow core fiber. *Optics express*, *22*(20), pp.23807-23828.

[90] Vincetti, L. and Setti, V., 2010. Waveguiding mechanism in tube lattice fibers. *Optics express*, *18*(22), pp.23133-23146.

[91] Nielsen, K., Rasmussen, H. K., Jepsen, P. U., & Bang, O. (2011). Porous-core honeycomb bandgap THz fibre. *Optics letters*, 36(5), 666-668.

[92] Hassani, A., Dupuis, A., & Skorobogatiy, M. (2008). Porous polymer fibres for low-loss Terahertz guiding. *Optics express*, 16(9), 6340-6351.

[93] Litchinitser, N. M., Abeeluck, A. K., Headley, C., & Eggleton, B. J. (2002). Antiresonant reflecting photonic crystal optical waveguides. *Optics letters*, 27(18), 1592-1594.

[94] Abeeluck, A., Litchinitser, N., Headley, C., & Eggleton, B. (2002). Analysis of spectral characteristics of photonic bandgap waveguides. *Optics express*, 10(23), 1320-1333.

[95] Cregan, R. F., Mangan, B. J., Knight, J. C., Birks, T. A., Russell, P. S. J., Roberts, P. J., & Allan, D. C. (1999). Single-mode photonic band gap guidance of light in air. *science*, 285(5433), 1537-1539.

[96] Litchinitser, N., Dunn, S., Steinvurzel, P., Eggleton, B., White, T., McPhedran, R., & De Sterke, C. (2004). Application of an ARROW model for designing tunable photonic devices. *Optics express*, 12(8), 1540-1550.

[97] Greenall, N., Valavanis, A., Desai, H.J., Acheampong, D.O., Li, L.H., Cunningham, J.E., Davies, A.G., Linfield, E.H. and Burnett, A.D., 2017. The Development of a Semtex-H Simulant for Terahertz Spectroscopy. *Journal of Infrared, Millimeter, and Terahertz Waves*, *38*(3), pp.325-338.

[98] Bozzi M, Georgiadis A, Wu K. Review of substrate-integrated waveguide circuits and antennas. *IET Microwaves, Antennas & Propagation*. 2011 Jun 6;5(8):909-20.

[99] Hejase, J.A., Paladhi, P.R. and Chahal, P.P., 2011. Terahertz characterization of dielectric substrates for component design and nondestructive evaluation of packages. *IEEE Transactions on Components, Packaging and Manufacturing Technology*, 1(11), pp.1685

[100] Grischkowsky, D., Keiding, S., Van Exter, M. and Fattinger, C., 1990. Far-infrared time-domain spectroscopy with terahertz beams of dielectrics and semiconductors. *JOSA B*, *7*(10), pp.2006-2015.

[101] Rogers Corporation (2018) Product Properties Tool - Laminates, Available at: http://tools.rogerscorp.com/acs/properties/laminates/index.aspx (Accessed: 9th May 2018).

[102] Argyros, A. (2009). Microstructured polymer optical fibres. *Journal of Lightwave Technology*, 27(11), 1571-1579.

[103] Barton, G., van Eijkelenborg, M. A., Henry, G., Large, M. C., & Zagari, J. (2004). Fabrication of microstructured polymer optical fibres. *Optical Fibre Technology*, 10(4), 325-335.

[104] van Eijkelenborg, M., Large, M., Argyros, A., Zagari, J., Manos, S., Issa, N., ... & Nicorovici, N. A. (2001). Microstructured polymer optical fibre. *Optics express*, 9(7), 319-327.

[105] Atakaramians, S., Afshar V, S., Ebendorff-Heidepriem, H., Nagel, M., Fischer, B. M., Abbott, D., & Monro, T. M. (2009). THz porous fibers: design, fabrication and experimental characterization. *Optics express*, 17(16), 14053-15062.

[106] Vienne, G., Xu, Y., Jakobsen, C., Deyerl, H. J., Jensen, J., Sorensen, T., ... & Yariv, A. (2004). Ultra-large bandwidth hollow-core guiding in all-silica Bragg fibers with nano-supports. *Optics Express*, 12(15), 3500-3508.

[107] Argyros, A., & Pla, J. (2007). Hollow-core polymer fibres with a kagome lattice: potential for transmission in the infrared. Optics express, 15(12), 7713-7719.andwidth hollow-core guiding in all-silica Bragg fibers with nano-supports. *Optics Express*, 12(15), 3500-3508.

[108] D'Auria, M., Otter, W.J., Hazell, J., Gillatt, B.T., Long-Collins, C., Ridler, N.M. and Lucyszyn, S., 2015. 3-D printed metal-pipe rectangular waveguides. *IEEE Transactions on Components, Packaging and Manufacturing Technology*, *5*(9), pp.1339-1349.

[109] Cook, K., Balle, G., Canning, J., Chartier, L., Athanaze, T., Hossain, M.A., Han, C., Comatti, J.E., Luo, Y. and Peng, G.D., 2016. Step-index optical fiber drawn from 3D printed preforms. *Optics letters*, *41*(19), pp.4554-4557.

[110] Furlan, W.D., Ferrando, V., Monsoriu, J.A., Zagrajek, P., Czerwińska, E. and Szustakowski, M., 2016. 3D printed diffractive terahertz lenses. *Optics letters*, *41*(8), pp.1748-1751.

[111] Wu, Z., Liang, M., Ng, W.R., Gehm, M. and Xin, H., 2012. Terahertz horn antenna based on hollow-core electromagnetic crystal (EMXT) structure. *IEEE Transactions on Antennas and Propagation*, *60*(12), pp.5557-5563.

[112] Ebendorff-Heidepriem, H., & Monro, T. M. (2007). Extrusion of complex preforms for microstructured optical fibers. *Optics Express*, 15(23), 15086-15092.

[113] West, J.A., Smith, C.M., Borrelli, N.F., Allan, D.C. and Koch, K.W., 2004. Surface modes in air-core photonic band-gap fibers. *Optics Express*, 12(8), pp.1485-1496.

[114] Johnson, S.G., Ibanescu, M., Skorobogatiy, M., Weisberg, O., Engeness, T.D., Soljačić, M., Jacobs, S.A., Joannopoulos, J.D. and Fink, Y., 2001. Low-loss asymptotically single-mode propagation in large-core OmniGuide fibers. *Optics Express*, 9(13), pp.748-7

[115] Temelkuran, B., Hart, S.D., Benoit, G., Joannopoulos, J.D. and Fink, Y., 2002. Wavelength-scalable hollow optical fibres with large photonic bandgaps for CO 2 laser transmission. *Nature*, 420(6916), p.650.

[116] Fink, Y., Winn, J.N., Fan, S., Chen, C., Michel, J., Joannopoulos, J.D. and Thomas, E.L., 1998. A dielectric omnidirectional reflector. *Science*, 282(5394), pp.1679-1682.

[117] Zhang, Y. and Robertson, I.D., 2010. Single-mode terahertz Bragg fiber design using a modal filtering approach. *IEEE Transactions on Microwave Theory and Techniques*, 58(7), pp.1985-1992.

[118] Kitagawa, A. and Sakai, J.I., 2009. Bloch theorem in cylindrical coordinates and its application to a Bragg fiber. *Physical Review A*, 80(3), p.033802.

[119] Xu, Y., Ouyang, G.X., Lee, R.K. and Yariv, A., 2002. Asymptotic matrix theory of Bragg fibers. *Journal of lightwave technology*, 20(3), p.428.

[120] Sakai, J.I., 2011. Analytical expression of confinement loss in Bragg fibers and its relationship with generalized quarter-wave stack condition. *JOSA B*, 28(11), pp.2740-2754.

[121] Hong, B., Somjit, N., Cunningham, J. and Robertson, I., 2015, August. Design study of low loss single-mode hollow core photonic crystal terahertz waveguide with support bridges. In *Infrared, Millimeter, and Terahertz waves (IRMMW-THz), 2015 40th International Conference on* (pp. 1-2). IEEE.

[122] K. J. Rowland, S. Afshar, and T. M. Monro, "Bandgaps and antiresonances in integrated-ARROWs and Bragg fibers; a simple model," *Opt. Exp.*, vol. 16, no. 22, pp. 17935-17951, Oct. 2008.

[123] C. M. Smith, N. Venkataraman, M. T. Gallagher, D. Müller, J. A. West, N. F. Borrelli, D. C. Allan, and K. W. Koch, "Low-loss hollow-core silica/air photonic bandgap fibre," *Nature*, vol. 424, no. 6949, pp. 657-659, Aug. 2003.

[124] H. Y. Yao, J. Y. Jiang, Y. S. Cheng, Z. Y. Chen, T. H. Her, and T. H. Chang, "Modal analysis and efficient coupling of TE 01 mode in small-core THz Bragg fibers," *Opt. Exp.*, vol. 23, no. 21, pp. 27266-27281, Oct 2015.

[125] S. Guo, S. Albin, and R. Rogowski, "Comparative analysis of Bragg fibers," *Opt. Exp.*, vol. 12, no. 1, pp. 198-207. Jan. 2004.

[126] M. Ibanescu, S. G. Johnson, M. Soljačić, J. D. Joannopoulos, Y. Fink, O. Weisberg, T. D. Engeness, S. A. Jacobs, and M. Skorobogatiy, "Analysis of mode structure in hollow dielectric waveguide fibers," *Phys. Rev. E*, vol. 67, no. 4, p.046608, Apr. 2003.

[127] Y. Zhang, and I. D. Robertson, "Analysis and design of Bragg fibers using a novel confinement loss diagram approach," *J. Lightw. Technol.,* vol. 28, no. 22, pp.3197-3206, Nov. 2010.

[128] J. I. Sakai, and N. Nishida, "Confinement loss, including cladding material loss effects, in Bragg fibers," *JOSA B*, vol. 28. no. 3, pp. 379-386, Mar. 2011.

[129] F. Poli, M. Foroni, D. Giovanelli, A. Cucinotta, S. Selleri, J. B. Jensen, J. Lægsgaard, A. Bjarklev, G. Vienne, C. Jakobsen, and J. Broeng, "Silica bridge impact on hollow-core Bragg fiber transmission properties," In *Opt. Fiber Commun. Conf.,* Anaheim, CA, p. OML8, Mar. 2007.

[130] Hong, B., Swithenbank, M., Somjit, N., Cunningham, J. and Robertson, I., 2016. Asymptotically single-mode small-core terahertz Bragg fibre with low loss and low dispersion. *Journal of Physics D: Applied Physics*, *50*(4), p.045104.

[131] Dai, D., Tang, Y. and Bowers, J.E., 2012. Mode conversion in tapered submicron silicon ridge optical waveguides. *Optics express*, *20*(12), pp.13425-13439.

[132] Daly, J.C., 1984. *Fiber Optics*. Boca Raton, Florida: CRC Press.

[133] Chen, D. and Chen, H., 2010. A novel low-loss Terahertz waveguide: Polymer tube. *Optics express*, *18*(4), pp.3762-3767.

[134] Carmel, Y., Chu, K.R., Dialetis, D., Fliflet, A., Read, M.E., Kim, K.J., Arfin, B. and Granatstein, V.L., 1982. Mode competition, suppression, and efficiency enhancement in overmoded gyrotron oscillators. *International Journal of Infrared and Millimeter Waves*, *3*(5), pp.645-665.

[135] Argyros, A., 2002. Guided modes and loss in Bragg fibres. *Optics Express*, *10*(24), pp.1411-1417.

[136] Cooper, K.B., Dengler, R.J., Llombart, N., Thomas, B., Chattopadhyay, G. and Siegel, P.H., 2011. THz imaging radar for standoff personnel screening. *IEEE Transactions on Terahertz Science and Technology*, *1*(1), pp.169-182.

[137] Hong, B., Somjit, N., Cunningham, J. and Robertson, I., 2017, September. High-order operating mode selection using second-order bandgap in THz Bragg fiber. In *Millimetre Waves and Terahertz Technologies (UCMMT), 2017 10th UK-Europe-China Workshop on* (pp. 1-2). IEEE.

[138] Robertson, I., Somjit, N. and Chongcheawchamnan, M., 2016. *Microwave and millimetre-wave design for wireless communications*. John Wiley & Sons.

[139] Roels, J., De Vlaminck, I., Lagae, L., Maes, B., Van Thourhout, D. and Baets, R., 2009. Tunable optical forces between nanophotonic waveguides. *Nature nanotechnology*, *4*(8), p.510.

[140] Park, H.G., Huang, S.Y. and Kim, B.Y., 1989. All-optical intermodal switch using periodic coupling in a two-mode waveguide. *Optics letters*, *14*(16), pp.877-879.

[141] Cohen, L.G. and Schneider, M.V., 1974. Microlenses for coupling junction lasers to optical fibers. *Applied Optics*, *13*(1), pp.89-94.

[142] Vitiello, M.S., Xu, J.H., Kumar, M., Beltram, F., Tredicucci, A., Mitrofanov, O., Beere, H.E. and Ritchie, D.A., 2011. High efficiency coupling of Terahertz micro-ring quantum cascade lasers to the low-loss optical modes of hollow metallic waveguides. *Optics express*, *19*(2), pp.1122-1130.

[143] Snyder, A.W. and Love, J., 2012. *Optical waveguide theory*. Springer Science & Business Media.

[144] Layton, M.R. and Bucaro, J.A., 1979. Optical fiber acoustic sensor utilizing mode-mode interference. *Applied Optics*, *18*(5), pp.666-670.

[145] S. G. Johnson, and J. D. Joannopoulos, "Block-iterative frequency-domain methods for Maxwell's equations in a planewave basis," *Optics express*, vol. 8, no. 3, pp. 173-190, Jan. 2001.

[146] Joannopoulos, J.D., Johnson, S.G., Winn, J.N. and Meade, R.D., 2011. *Photonic crystals: molding the flow of light*. Princeton university press.

[147] Deslandes, D. and Wu, K., 2003. Single-substrate integration technique of planar circuits and waveguide filters. *IEEE Transactions on Microwave Theory and Techniques*, *51*(2), pp.593-596.

[148] Petrov, A.Y. and Eich, M., 2004. Zero dispersion at small group velocities in photonic crystal waveguides. *Applied Physics Letters*, *85*(21), pp.4866-4868.

[149] Engen, G.F. and Hoer, C.A., 1979. Thru-reflect-line: An improved technique for calibrating the dual six-port automatic network analyzer. *IEEE transactions on microwave theory and techniques*, *27*(12), pp.987-993.

[150] McNab, S.J., Moll, N. and Vlasov, Y.A., 2003. Ultra-low loss photonic integrated circuit with membrane-type photonic crystal waveguides. *Optics express*, *11*(22), pp.2927-2939.

[151] Hong, B., Doychinov, V., Platt, D., Clarke, R., Akkaraekthalin, P., Somjit, N., Cunningham, J., and Robertson, I., 2018. Design and Measurement of a Single-Mode Hollow Photonic Crystal Integrated Waveguide. *IEEE Transactions on Microwave Theory and Technique*, xx(x), p.xx-xx. (Submitted)

[152] Xu, Y., Lee, R.K. and Yariv, A., 2000. Asymptotic analysis of Bragg fibers. *Optics Letters*, 25(24), pp.1756-1758.

[153] Withayachumnankul, W., Yamada, R., Fumeaux, C., Fujita, M. and Nagatsuma, T., 2017. All-dielectric integration of dielectric resonator antenna and photonic crystal waveguide. *Optics Express*, 25(13), pp.14706-14714.

[154] Weily, A.R., Esselle, K.P., Bird, T.S. and Sanders, B.C., 2006. Linear array of woodpile EBG sectoral horn antennas. *IEEE Transactions on Antennas and Propagation*, 54(8), pp.2263-2274.

[155] Yee, C.M. and Sherwin, M.S., 2009. High-Q terahertz microcavities in silicon photonic crystal slabs. *Applied Physics Letters*, 94(15), p.154104.

[156] Jian, Z., Pearce, J. and Mittleman, D.M., 2004. Defect modes in photonic crystal slabs studied using terahertz time-domain spectroscopy. *Optics letters*, 29(17), pp.2067-2069.

[157] Bingham, A.L. and Grischkowsky, D., 2008. Terahertz two-dimensional high-Q photonic crystal waveguide cavities. *Optics letters*, 33(4), pp.348-350.

[158] Mendis, R., Nagai, M., Zhang, W. and Mittleman, D.M., 2017. Artificial dielectric polarizing-beamsplitter and isolator for the terahertz region. *Scientific Reports*, 7(1), p.5909.

[159] Jiu-Sheng, L., Han, L. and Le, Z., 2015. Tunable multi-channel terahertz wave power splitter. *Optics Communications*, 356, pp.616-619.

[160] Zahednamazi, M., Alikhani, A. and Hamidi, S.M., 2016. Photonic crystal power combiner based on hexagonal waveguides. *Optik-International Journal for Light and Electron Optics*, 127(20), pp.8600-8603.

[161] Yata, M., Fujita, M. and Nagatsuma, T., 2016. Photonic-crystal diplexers for terahertz-wave applications. *Optics express*, 24(7), pp.7835-7849.

[162] Fan, F., Liu, Y., Li, J., Wang, X.H. and Chang, S.J., 2015. Active terahertz directional coupler based on phase transition photonic crystals. *Optics Communications*, 336, pp.59-66.

[163] Park, D., Kim, S., Park, I. and Lim, H., 2005. Higher order optical resonant filters based on coupled defect resonators in photonic crystals. *Journal of lightwave technology*, 23(5), p.1923.

[164] Li, S., Liu, H., Sun, Q. and Huang, N., 2015. A tunable terahertz photonic crystal narrow-band filter. *IEEE Photon. Technol. Lett.*, 27(7), pp.752-754.

[165] Li, J.S., Liu, H. and Zhang, L., 2015. Compact and tunable-multichannel terahertz wave filter. *IEEE Transactions on Terahertz Science and Technology*, 5(4), pp.551-555.

[166] Luo, Y., Li, Y., Hu, Z. and Liu, J., 2016. A novel broadband terahertz filter for photonic crystal. *Journal of Modern Optics*, 63(17), pp.1688-1694.

[167] Lu, Y., Liu, H., Sun, Q., Huang, N. and Wang, Z., 2016. Terahertz narrow-band filter based on rectangle photonic crystal. *Journal of modern optics*, 63(3), pp.224-230.

[168] Zhou, W., Chen, H.M., Ji, K. and Zhuang, Y., 2017. Vertically magnetic-controlled THz modulator based on 2-D magnetized plasma

photonic crystal. *Photonics and Nanostructures-Fundamentals and Applications*, 23, pp.28-35.

[169] Zhang, X., Hosseini, A., Lin, X., Subbaraman, H. and Chen, R.T., 2013. Polymer-based hybrid-integrated photonic devices for silicon on-chip modulation and board-level optical interconnects. *IEEE Journal of Selected Topics in Quantum Electronics*, 19(6), pp

[170] Bayat, K., Rafi, G.Z., Shaker, G.S., Ranjkesh, N., Chaudhuri, S.K. and Safavi-Naeini, S., 2010. Photonic-crystal-based polarization converter for terahertz integrated circuit. *IEEE Transactions on Microwave Theory and Techniques*, 58(7), pp.1976-1984.

[171] Li, Z., Zhang, Y. and Li, B., 2006. Terahertz photonic crystal switch in silicon based on self-imaging principle. *Optics express*, 14(9), pp.3887-3892.

[172] Hasek, T., Kurt, H., Citrin, D.S. and Koch, M., 2006. Photonic crystals for fluid sensing in the subterahertz range. *Applied physics letters*, 89(17), p.173508.

[173] Kakimi, R., Fujita, M., Nagai, M., Ashida, M. and Nagatsuma, T., 2014. Capture of a terahertz wave in a photonic-crystal slab. *Nature Photonics*, 8(8), p.657.

[174] Benz, A., Deutsch, C., Fasching, G., Unterrainer, K., Andrews, A.M., Klang, P., Hoffmann, L.K., Schrenk, W. and Strasser, G., 2009. Photonic crystal mode terahertz lasers. *Journal of Applied Physics*, 105(12), p.122404.

[175] Zhang, H., Scalari, G., Faist, J., Dunbar, L.A. and Houdré, R., 2010. Design and fabrication technology for high performance electrical pumped terahertz photonic crystal band edge lasers with complete photonic band gap. *Journal of Applied Physics*, 108(9),

[176] Zhang, H., Dunbar, L.A., Scalari, G., Houdré, R. and Faist, J., 2007. Terahertz photonic crystal quantum cascade lasers. *Optics Express*, 15(25), pp.16818-16827.

[177] Benz, A., Deutsch, C., Fasching, G., Unterrainer, K., Andrews, A.M., Klang, P., Schrenk, W. and Strasser, G., 2009. Active photonic crystal terahertz laser. *Optics Express*, 17(2), pp.941-946.

[178] Zhang, H., Scalari, G., Beck, M., Faist, J. and Houdré, R., 2011. Complex-coupled photonic crystal THz lasers with independent loss and refractive index modulation. *Optics express*, 19(11), pp.10707-10713.

[179] Song, B.S., Noda, S., Asano, T. and Akahane, Y., 2005. Ultra-high-Q photonic double-heterostructure nanocavity. *Nature materials*, 4(3), p.207.

[180] Issa, N.A., Argyros, A., van Eijkelenborg, M.A. and Zagari, J., 2003. Identifying hollow waveguide guidance in air-cored microstructured optical fibres. *Optics Express*, *11*(9), pp.996-1001.